The Dissertation Committee for Xing Zheng Certifies that this is the approved version of the following Dissertation:

Continental-Scale High-Resolution River Geometry and Real-Time Inundation Mapping

Committee:

David R. Maidment, Supervisor

Paola Passalacqua

Ben R. Hodges

Zong-Liang Yang

Polina Sela

Continental-Scale High-Resolution River Geometry and Real-Time Inundation Mapping

by

Xing Zheng

Dissertation

Presented to the Faculty of the Graduate School of

The University of Texas at Austin

in Partial Fulfillment

of the Requirements

for the Degree of

Doctor of Philosophy

The University of Texas at Austin

May 2018

Dedication

This body of work is dedicated to my adviser David R. Maidment and co-adviser Paola Passalacqua for their wonderful support and guidance.

Acknowledgements

I would like to thank my advisor, Dr. David Maidment for his guidance and visions. Being his last PhD student is definitely the most glorious moment in my life so far.

I would like to thank my co-advisor, Dr. Paola Passalacqua for her insights, patience and kindness. She teaches me how to be an excellent scholar as well as a nice person.

I would like to thank Dr. Tim Whiteaker and Dr. Yan Liu for all the help they give me throughout my graduate student career. They are my great teachers and fantastic friends. They teach me many technical skills and also listen to the struggles in my life.

I would like to thank Tongren Zhu and Bochao Zhan for helping me settle down on the new continent. I appreciate all the things they did for me in the past.

At last, I would like to thank my parents, friends, family members, teachers and fans. Your unconditional love is where all my strength comes from, inspiring me to conquer the world.

Abstract

Continental-Scale High-Resolution River Geometry and Real-Time Inundation Mapping

Xing Zheng, Ph.D.

The University of Texas at Austin, 2018

Supervisor: David R. Maidment

Flooding is the most threatening natural disaster worldwide considering the fatalities and property damage it causes. Recent flood disasters have raised concerns for accurate and responsive inundation forecast due to the rapid spread and astonishing destructive power of these events. Although recent development in large scale hydrologic simulation has enabled the real-time streamflow simulation operating on millions of river reaches, a framework for converting the forecast discharge into corresponding water surface elevation and inundation maps at a continental-scale is absent to better support local flood response. To accurately map flood inundation extent, a comprehensive description of the geometry of the channel is indispensable. As such, this dissertation presents an innovative approach for estimating river geometry and conducting inundation mapping at a continental-scale with a high spatial resolution. This approach is based on the concept of Height Above Nearest Drainage (HAND). Advanced hydrologic terrain analysis workflows have been designed to derive channel hydraulic properties, stage-discharge rating curves, and inundation extents using HAND. After the mechanism being

presented, the implementation of this approach across the contiguous United States has been demonstrated using the 10-meter National Elevation Dataset. The integrity of the outputs has been validated through the comparison with best available references at multiple test sites. Considering the increasingly availability of high-resolution topographic data derived from lidar technology, the dissertation further presents how advanced geomorphic feature extraction tools are integrated into the proposed approach to overcome the challenges associated with the enrichment of terrain details. At last, this dissertation presents how banklines, an essential piece of river geometry characteristic as the boundary differentiates channel zone from floodplain, is detected with enhanced geomorphic feature extraction tools for improving large-scale hydrologic simulation and inundation mapping accuracy.

Table of Contents

List of Tables

List of Figures

Chapter 1: Introduction

1.1 BACKGROUND

Flooding is the most threatening natural disaster worldwide considering the fatalities and property damage it causes. It makes up 40% of all natural disasters worldwide and causes about half of all natural hazard fatalities (Noji, 1991; Ohl et al., 2001). In the 1990s alone, flooding caused an asset loss of about $50 billion (NRC, 2009). Under a changing climate, the magnitude (Knox, 1993) and frequency (Milly, 2002) of floods increase significantly, which, together with the growing population and the expanding urbanization, lead to more serious and frequent hazards. For 136 coastal cities across the world, annual losses due to flooding will increase to $52 billion per year by 2050 (the 2005 estimate was $6 billion) with projected socio-economic change. This number could even reach $1 trillion if other factors are considered (Hallegatte, 2013).

The growing risk and damage result in a growing concern. In August, 2016, the U.S. National Oceanic and Atmospheric Administration (NOAA) launched a new National Water Model (NWM), which enhances and expands NOAA's water flow forecasts from approximately 4,000 forecast locations to 2.7 million stream reaches defined in the geospatial hydrologic framework of the country, the National Hydrography Dataset Plus (NHDPlus). With the help of the NWM, 18-hour short-range forecast, 10-day medium-range forecast, 30-day long-range forecast flow conditions and analysis model for current conditions are available to the public on a regular basis for all the 2.7 million reaches across the continental U.S. However, only if the discharge time series or hydrographs are interpreted as understandable end products, can they become usable and useful to the public, first responders, and decision makers (Merz et al., 2007). The most common type of end product is a combination of the hazard level and the vulnerability at

any location (Apel et al., 2009). Inundation maps show the spatial distribution of the flooding and inform the direction of flood emergency response to people and communities who need help. Recent flood disasters resulting from hurricanes Harvey, Irma and Maria in 2017 emphasize the need for rapid, approximate flood inundation mapping over very large areas. However, traditional ways for building inundation maps from local hydraulic models are not viable economically and cannot be coupled with the newly-established national hydrological forecast system. Therefore, an innovative approach, which can conduct inundation mapping at a continental-scale with a high spatial resolution, is needed.

To accurately map flood inundation extent, a comprehensive description of the geometry of the channel is indispensable, since the river fluvial system conveys water across the continent and is most vulnerable to extreme water events (Maidment, 1992). The availability of high-performance computing power from advanced cyberinfrastructure and the completion of a continental-coverage high-resolution geospatial hydrologic framework facilitate the hydrologic terrain analysis to enable moving from watershed scale to continental scale. The continental-coverage terrain analysis product developed through this study links discharge, water depth and flood inundation extent for each stream reach. Combining this product with the establishment of the continental-coverage high-resolution stream discharge forecast system, a continental-scale high-resolution river geometry data set and a real-time flood inundation mapping system could be obtained.

Moreover, the advancement in lidar technology promotes wide availability of high-resolution terrain datasets in the near future, helping to address existing issues in current inundation mapping techniques and to improve mapping accuracy. Newly

emerging geomorphic feature extraction algorithms applied to lidar-derived Digital Elevation Models (DEM) will support the detection of key river channel features and characteristic parameters, allowing further understanding of river fluvial system. Among these features of interest, the reach-average bankfull width estimation for every river segment in the network is particularly needed, since it is critical information for improving the performance of large-scale hydrological simulation and inundation mapping.

1.2 LITERATURE REVIEW

1.2.1 Hydrologic Terrain Analysis

Topography plays a crucial role in the natural hydrologic cycle that controls the distribution and flux of water (Maidment, 2000). Digital representation of topography is usually organized with one of three data structures (Wilson and Gallant, 2000): (1) regular grids, (2) triangulated irregular networks, and (3) contours. Among these three structures, a rectangular grid DEM is most widely used due to its simplicity and machine-friendly structure (Tarboton, 2008). A terrain analysis consists of the quantitative analysis of topographic surfaces (Basso, 2005). Terrain analysis using DEMs has been performed in hydrology for watershed delineation (Band, 1986; Maidment, 2002), channel network extraction (O'Callaghan and Mark, 1984; Band, 1986; Tarboton, 1997; Passalacqua, 2010a), and flow-related quantities derivation (Moore et. al, 1991; Tesfa et al., 2009).

For the extraction of channel networks, the classic method is the flow accumulation algorithm, which follows a well-defined procedure of (1) pit removal, (2) flow direction calculation, and (3) flow accumulation calculation (Wilson and Gallant, 2000; Maidment, 2002). Pits consist of grid cells surrounded by higher neighbor cells

resulting from terrain depressions and deficiencies in the DEM production process and generalization in the representation of the terrain (Jenson and Domingue, 1988; Jenson, 1991). Pits are usually removed with a drainage correction process that alters the elevation of some cells in the DEM (Tarboton, 2008). Drainage correction ensures that the DEM is hydrologically correct, meaning that water falling at any location within the DEM domain will eventually drain to the watershed outlet. The most common drainage correction approach is pit filling, which is implemented by identifying the area draining to each pit and raising the elevation of all cells within it to the elevation of the lowest point of the area boundary (Jenson and Domingue, 1988). Improvements in pit filling algorithms have been made (Planchon and Darboux, 2001; Arge et al., 2003) as raising only grid elevation may lead to an excessive correction when the flow path goes through barriers. Therefore, carving (Garbrecht and Martz, 1997; Soille et al., 2003), a combination of filling and carving (Soille, 2004), and a landscape-evolution-based method (Grimaldi et al., 2007) have also been studied. However, these newer algorithms of these alternatives have not been adapted for high-performance implementation. Therefore, the classic pit filling approach will be adopted in this research.

Past experience in using spatial information of existing streams to guide drainage correction such as stream burning (Maidment, 1996, Callow et al. 2007) and AGREE (Hellweger, 1997) also provide possible approaches to embed the existing geospatial hydrologic framework in hydrologic terrain analysis. Both the single flow direction algorithm and multiple flow direction algorithms have been developed for flow direction computation. The single flow direction method (O'Callaghan and Mark, 1984) assigns the flow direction of a cell towards one of its eight neighboring grid cells according to the steepest descent slope. The main limitation of the single flow direction method is that it

can assign flow directions to only one of eight possible directions (Fairfield and Leymarie, 1991; Costa-Cabral and Burges, 1994). To solve this limitation, many multiple flow direction approaches have been proposed (Quinn et al., 1991; Tarboton, 1997; Seibert and McGlynn, 2007), which proportion the outflow from each cell among one or more lower neighbors. These methods introduce dispersion (spreading out) and reduce bias from routing flow along fixed directions. The D-infinity method defines the flow direction of each cell as the direction of steepest downward slope on eight triangular facets centered at that cell (Tarboton, 1997). For both single flow direction method and multiple flow direction method, a main computational bottleneck is the identification flow direction for a flat zone with no local gradient, which makes the local flow direction problem become global. A geomorphologically inspired process has been developed to solve this problem, which directs flow towards adjacent low terrain and away from adjacent high terrain (Garbrecht and Martz, 1997). A First In First Out (FIFO) queue is then introduced to speed up this algorithm (Barnes et al. 2014).

In the flow accumulation area computation, the limitation that researchers identify as most critical is the assumption used in stream definition that all channels begin at the same flow accumulation threshold (McNamara et al., 2006). An objective accumulation threshold selection approach using the constant drop property for Strahler streams has been explored (Tarboton and Ames, 2001). An alternative to the typical flow accumulation algorithm is the least-cost-path (LCP) algorithm (A* Search) (Hart et al. 1968; Ehlschlaeger, 1989), which was initially designed to find the shortest route from a starting point to a given destination. In the LCP algorithm, no pit-removal process is involved; therefore no modification of the raw elevations needs to be made. Costs are related to elevation changes along the flow path. Research shows that this approach

results in more accurate flow routing through large, nested depressions with fewer artifacts (Kinner et al., 2005). This algorithm has been redesigned, improved, and implemented in GRASS GIS flow routing functions (Metz et al. 2011; Neteler and Helena, 2013).

New channel extraction methods have also been developed to avoid limitations such as pit filling and to take full advantage of the high-resolution terrain datasets (Lashermes et al, 2007; Passalacqua et al., 2010a; Pelletier, 2013). Among these methods, GeoNet (Passalacqua et al., 2010a) has demonstrated its effectiveness on both steep, natural landscapes (Passalacqua et al., 2010a; Passalacqua et al., 2010b) and flat urbanized landscapes (Passalacqua et al., 2012; Sangireddy et al., 2016). In GeoNet, a nonlinear-diffusion filter is first applied to the original DEM to remove small scale variability and enhance features of interest; then a statistical analysis is conducted on curvature calculated on the filtered DEM to identify likely channelized pixels; finally geodesic minimization principles are applied with a cost function based on contributing area and curvature to extract channel heads and flowlines (Passalacqua et al., 2010a).

On the derivation of flow-related quantities, hydrological proximity measures comprise one important branch, which are a group of distances up to ridge grids with no inflow and distances down to stream grids from any grid within the DEM domain following its flow path (Tesfa et al., 2009). Among these hydrological proximity measures, the vertical distance down to stream has great potential for inundation mapping applications. This capability was first presented during the development of a flood risk model for the Czech Republic (Rodda, 2005). Then other researchers worked on this approach which was named Height Above the Nearest Drainage (HAND) (Renno et al., 2008). HAND was applied and tested in terrain classification (Renno et al., 2008), soil

moisture classification (Nobre et al., 2011; Cuartas et al., 2012), and inundation mapping (Nobre et al., 2016). However, its integration with existing stream networks, its implementation at a continental scale, and its application to describe river geometry have not been explored, which becomes one of the main objectives of this research.

Advances in terrain data acquisition technology, especially the Geiger-mode LiDAR for commercial application (Clifton, 2015; Ullrich and Pfennigbauer, 2016), are increasing the capability of collecting high-resolution terrain data at a large spatial coverage. The big data challenge and opportunity brought by this technology evolution (Lynch, 2008), together with the advancement of high performance computational techniques and the accessibility to supercomputing resources, have been spurring hydrologists and computer scientists to collaborate to bring the traditional hydrological terrain analysis functions to a highly scalable level. Recent development of the TauDEM software (TauDEM 2016) makes it a scalable and high-performance package, which is usable in a supercomputing environment. Fundamental hydrologic terrain analysis, including pit filling (Wallis et al, 2009a), flow direction and contributing area computation (Wallis et al, 2009b), and hydrological proximity measures computation (Tesfa et al, 2011) now can be run in a parallel mode on large dataset in reasonable time.

A CyberGIS framework has been developed as a software framework that synergistically integrates both application-driven and user-centric functionalities of cyberinfrastructure, GIS, and spatial analysis (Wang, 2010). Following the CyberGIS framework, TauDEM has been developed as a cyberinfrastructure-empowered science gateway application service (Fan et al., 2014). A virtual tile memory manager is developed to manage the memory during the parallel terrain analysis in a shared-memory system (Yıldırım, 2015). An improved parallel algorithm has been developed to solve the

computational bottleneck of flow direction computation, solving flow directions across flat zones (Survila et al., 2016). This new algorithm outperformed the existing parallel flow direction algorithm by two orders of magnitude (Survila et al., 2016). All these recent advancements in high-performance hydrologic terrain analysis are the backbone of the propose research, a goal of which involves the design and implementation of a more sophisticated terrain analysis workflow in a supercomputing system.

1.2.2 Continental Scale River Geometry Estimation

Although the theoretically optimal configuration of a continental-scale hydrodynamic model should be a combination of 1D, 2D, and 3D models, establishing a stable 1D hydrodynamic model seems to be the feasible next goal for modelling large-scale river networks (Hodges, 2013). Whatever model is applied, detailed river geometry information is always an indispensable input. 1D Continental river dynamic modelling has its own unique requirement for river geometry data: on one hand, the data needs to be complete and detailed enough to cover the whole study domain; on the other hand, river geometry information contained within a higher-resolution terrain dataset needs to abstracted to a proper coarser level at which 1D hydrodynamic modelling works well (Hodges, 2013).

One basic computation unit in the one-dimensional model is the perpendicular cross section, which depicts the channel bathymetry at one place along the watercourse (Brunner, 1997). At a local scale, research has been conducted to extract cross sections from hydraulic models to build an updated TIN, which describes channel terrain details that are missed in a coarser-resolution (30-meter) DEM (Tate et al., 2002). The optimal distance between cross sections in 1D hydraulic modelling has been shown to be

proportional to the bankfull width (Samuels, 1990; Castellarin, 2009); adding extra cross sections within the optimal spacing decreases rather than increases the accuracy of the simulation due to rounding errors (Castellarin, 2009). However, whether the 10-meter resolution that the national elevation dataset (NED) currently has for the national coverage is enough to describe channel geometry has not been explored yet.

An alternative approach is to use a GIS-based workflow to convert an irregularly spaced set of bathymetry points to a thalweg and a 3D mesh grid that can be used in hydraulic modelling (Merwade et al., 2005). When generating a bathymetric raster surface from scattered survey points, channel anisotropy has some nontrivial effect on the final interpolation result and an interpolation method named elliptical inverse distance weighting has been developed to account for it (Merwade et al, 2006). GIS tools have been developed to map and analyze channel data in a curvilinear coordinate system, interpolating cross sections to create a 3D main channel mesh grid, and integrating it with the surrounding topography (Merwade et al., 2008).

Hydraulic geometry, a set of power functions (Equation (1.1)) established among several hydraulic parameters (i.e., river width, depth, and velocity) and changing discharge at a specific cross section, has been extensively studied and widely applied after its creation over six decades ago (Leopold et al., 1953).

$$w = aQ^b \tag{1.1a}$$

$$d = cQ^f \tag{1.1b}$$

$$v = kQ^m \tag{1.1c}$$

where Q is water discharge, w is water surface width, d is mean water depth, and v is mean velocity; a, c, k, b, f, and m are numerical constants.

Research on the topic first focused on verifying the existence of these power relationships at different locations with different physiographic settings (Park, 1977; Rhodes, 1978). Some researchers also tried to identify underlying physical principles that caused the hydraulic geometry relationship (Richards, 1973; Knighton, 1974; Knighton, 1975; Phillips and Harlin, 1984). The temporal (Knighton, 1975) and spatial (Phillips and Harlin, 1984) stability of hydraulic geometry were questioned.

An influential study of hydraulic geometry was conducted by Ferguson (Gleason, 2014). In Ferguson's paper in 1986, hydraulic geometry is reduced to "hydraulic and geometry" (Ferguson, 1986). Different channel shapes such as rectangular, triangular, parabolic, and asymmetrical-curved were assumed and then flow resistance equations such as Manning, Keulegan, and Darcy-Weisbach were applied to generate the relationship between the hydraulic properties and discharge (Ferguson, 1986). In that way, hydraulic geometry was reproduced from a theoretical approach instead of from observations. Based on this analysis, hydraulic geometry exponents were found to be functions of cross sectional shape (Ferguson, 1986). Another conclusion drawn from that work is that the power law form worked for hydraulic geometry due to the parabolic channel shape where field data were usually collected (Ferguson, 1986).

Explicit equations were derived in later research for the exponents and the coefficients in hydraulic geometry with generalized cross section geometry and hydraulics (Dingman, 2007). Comparison between analytical and observed exponent values shows that empirical hydraulic equations tend to underestimate channel hydraulic conductance in high flow conditions (Dingman, 2007). Hydraulic geometry has been widely applied. The most well-known application is the daily discharge data USGS publishes for the streams and rivers calculated from hydraulic geometry and channel

elevation data (Huizinga, 2009). Regionalization of hydraulic geometry consisted of the analysis of its spatial pattern (Mosley, 1981; Castro and Jackson, 2001; Pistocchi and Pennington, 2006; Johnson and Fecko, 2008; Mulvihill and Baldigo, 2012). Other applications of hydraulic geometry include habitat assessment (Singh and McConkey, 1989), ancient ice lake burst (Tinkle and Pengelly, 1995), and hydrologic modeling (Wiele and Smith, 1996). Reach-average hydraulic geometry has also been explored and its existence has been demonstrated at several sites (Jowett, 1998; Wohl et al. 2004; Harman et al, 2008). Researchers are also trying to derive similar relationship between other hydraulic and geomorphic variables (Hood, 2002; David et al., 2010; Magnusson et al., 2012; Gleason and Smith, 2014).

The main limitations of hydraulic geometry are: first, hydraulic geometry is a mixture of geometry and hydraulics, which involves more uncertain processes compared to only understanding topographic variation. Second, hydraulic geometry relies on field-observed river geometry and discharge data pairs, which complicates the process and limits the data availability and density across a large study domain. Third, this approach relies more on statistical analysis than terrain truth examination, and the unique geomorphic setting of each reach is neglected. Also, the resolution currently captured by river geometry is not high enough to cover small tributaries.

Besides hydraulic geometry, inferring channel characteristics from remotely sensed imagery is another essential branch of river geometry research. A software tool named RivWidth was developed to estimate river width from remotely sensed water mark (Pavelsky and Smith, 2008). After a channelized zone is classified from the imagery, the algorithm extracts a river centerline using boundary definition techniques, generates a perpendicular line segment at every centerline pixel, and computes the average length of

the perpendicular lines lying on the same reach. Other studies calculate the width of each channel as the mean of three lengths (one at both ends and one in the center) measured in the manually-extracted or the Normalized Difference Vegetation Index (NDVI)-classified channel zone from Landsat Enhanced Thematic Mapper Plus (ETM+) mosaic (Trigg et al., 2012; O'Loughlin et al., 2013).

Built upon the basic river geometry estimation approaches that are effective at local scale, efforts have been made to obtain a channel geometry description at a continental scale or even at global scale. A simple global river bankfull width and depth database was developed using a regression relationship between bankfull discharge and drainage area and hydraulic geometry relationships (Andreadis et al., 2013). Applying an algorithm that calculates the distance from remote-sensed water body edge to river centerlines following the flow direction, the Global Width Database for Large Rivers (GWD-LR) was developed with the SRTM Water Body Database and the HydroSHED (Hydrological data and maps based on SHuttle Elevation Derivatives at multiple Scales) flow direction raster (Yamazaki et al., 2014). Both bankful width and effective river width without islands were computed for river channels between 60S and 60N (Yamazaki et al., 2014). A so-called first fine-resolution, continental-scale river centerline and width database, Landsat-derived North American River Width (NARWidth) dataset has been developed (Allen and Pavelsky, 2015). It includes rivers ranging from approximately fourth to ten Strahler stream order, the width of which is wider than 30 meter at annual mean discharge. The workflow for creating NARWidth is similar to previous studies: select an optimal mean-flow-condition month for each Landset tile using hydrologic time series analysis; download Landset images in the selected month for each Landset, set thresholds to the modified normalized difference water index (MNDWI) to identify the

binary water mark, use RivWidth software to calculate channel widths from water marks, and compute channel surface area by multiplying river width and length.

The limitation of these large-coverage datasets can be easily identified when applied to support hydraulic modelling and inundation mapping: first, the resolution of the river network is not high enough to direct local-level inundation mapping. Taking Texas as an example, there are 20,004 HydroSHEDS flowlines in Texas, while the flowline number is 101,240 in the medium-resolution (10-meter) NHDPlus dataset. Therefore, numerous local streams, which are critical during flood events, are not detected in the existing river width and depth database. Second, only the bankfull width and depth are provided instead of a continuous relationship between stage height and channel properties. Then only a simple shape such as rectangular or triangle can be assumed for the channel, which may cause nontrivial errors in water level simulation. Third, while the objective of research in this field is to properly describe river geometry, which is a category of topographic information, researchers only focus on searching answers from remotely sensed data or in statistical approaches instead of extracting insightful information from the actual terrain. General laws summarized from statistical techniques are insufficient to depict the unique physiographic characteristics each channel has, and remote-sensed imagery only captures part of a transient state of the river system only from a top view, which is not complete. Therefore, a new approach that is able to evaluate channel geometry properties from terrain data is more rational and urgently needed. Since this new approach is based on analyzing the actual terrain, it could provide more accurate channel information, compared to the channel geometry assumption the Nation Water Model currently adopts, a trapezoidal cross-section with constant side slopes and a base width that depends on stream order, which leads to a more

accurate water level forecast. This improvement makes the new method promising to be incorporated into the National Water Model for operational use.

An information framework and GIS tools have also been developed for collecting cross sections from available local hydraulic models and referencing them onto the NHDPlus river system (Zheng, 2015). However, when the uneven distribution of local models leads to the unbalance of river geometry data availability, some reaches get relatively complete coverage by cross sections lying on them, while other unmodelled reaches have no cross section to describe their channel geometry information. The overlapping between cross sections especially at river confluences is another issue that can cause problems during a 1D hydrodynamic simulation. Also, the collection of local hydraulic models takes a lot of collaboration, which is not feasible in a short time. In a nutshell, organizing river geometry information by cross sections is not a comprehensive choice, since river geometry information is oversampled on cross sections and undersampled between cross sections. A new approach is needed that can digest all available terrain information and provide integrated channel characteristics. One essential point that needs to be clarified here is that what hydraulic modeling really needs about river geometry is not the actual channel shape but the hydraulic parameters derived from the channel shape that exist in the mass and momentum conservation equations. Therefore, if the relationships between channel hydraulic parameters and stage height can be directly derived from hydrological terrain analysis products, there is no need to keep cross sections as an intermediate product.

1.2.3 Continental Scale Inundation Mapping

The classification of "large scale" evolves as time goes on. When the first paper on large-scale floodplain modelling was published in 1990, tens of kilometers were treated as the "large scale" (Gee et al., 1990), while recent researches on large-scale inundation mapping have moved to a continental coverage or even a global coverage (Schumann, 2013; Sampson, 2015; Dottori et al., 2016). However, the best resolution that can be reached in current large-scale hydraulic models is 1-km land surface cells. Then the simulated water surface elevations are reprojected on 90-meter DEMs to create inundation maps. In that case, as discussed in the previous section, flood impact can be evaluated only for large rivers even from the reprojected inundation maps. Since previous researches were conducted on desktop machines, their ability to move to higher spatial resolutions is limited.

The most common approach to create inundation maps is planar linear interpolation: water levels measured at gauges or computed using hydraulic models using cross-sections are linearly interpolated to a uniformly sloping water surface plane. This plane is intersected with the original terrain dataset, and all areas below the interpolated water surface levels are identified as inundated (Apel et al., 2009). The simplicity of this method leads to several drawbacks: first, the flow field is not considered in the planar surface assumption, which leads to local depressions that are never connected to the flow. A cost function approach has been developed to eliminate local depressions by assigning a high cost to drylands (Werner, 2001). Second, there is no volume control or mass conservation, which results in overestimation of flows in flat areas. Flood inundation extent highly depends on topography. In flat areas, due to low gradients, small errors in modelled water surface elevations may lead to large errors in the predicted inundation

extent. Third, the effect of levees is neglected. Fourth, no dynamics of the flood process are described.

The storage cell approach is an alternative method for inundation mapping (Cunge et al., 1980; Romanowicz et al., 1996). In this type of approach, channel and floodplain cells are treated as interconnected storage reservoirs (Cunge et al., 1980). Volume/height, cross-section-area/height, wetted perimeter/height functions are derived from river geometry for each cell (Romanowicz et al., 1996). Then uniform flow formulas are implemented to designated channel and floodplain cells. Both floodplain discretization and hydraulic function derivation involve user intervention. A raster-based inundation model, LISFLOOD-FP (Bates and De Roo, 2000), has been widely implemented due to its simplicity and effectiveness. The model initially consisted of a one-dimensional kinematic wave approximation for channel dynamics and a two-dimensional diffusion wave representation of floodplain dynamics (Bates and De Roo, 2000). Cell discretization was raster-based so that it could be derived from a DEM automatically. A rectangular geometry was applied to channels and flow limiter was included to avoid instabilities caused by excessive water leaving a given cell at a single time step. Due to the kinematic wave assumption, backwater effects were ignored. A Near Channel Floodplain Storage (NCFS) scheme was then added to LISFLOOD-FP to deal with the missing floodplain storage of the coarser pixels within which the narrower channel lies (Horritt and Bates, 2001b). Later on, researchers found that the inclusion of the flow limiter led to simulation insensitivity to floodplain friction and made the results dependent on grid size and time step, so an adaptive time-stepping solution was proposed (Hunter et al., 2005). However, the optimum stable time step reduced quadratically with increasing resolution, which greatly extended the computational time. Therefore, a simplified version of the

shallow water equations that neglects advection was derived and implemented in a new version of LISFLOOD-FP (Bates et al., 2010). A new subgrid structure to simulate channel hydrodynamics was then developed for channels with much smaller width than the model grid resolution (Neal et al., 2012).

Traditional 1D and 2D hydraulic models still dominate local scale inundation mapping, and are usually treated as reference models when testing new inundation mapping approaches. Hydrologic Engineering Center's River Analysis System (HEC-RAS) (Brunner, 1997) is one of the most widely used hydraulic models, which has been accepted nationally by the National Flood Insurance Program (NFIP) (NRC, 2009). The HEC-GeoRAS interface processes geo-spatial data between HEC-RAS and GIS, which takes water surface profile data exported from HEC-RAS simulations and conducts GIS analysis for floodplain mapping (Ackerman, 2005). However, raster-based models have been implemented for continental-scale inundation mapping because the way they organize the data makes them easier to be coupled with large scale hydrologic models. Several global flood hazard frameworks for continental inundation mapping have been developed. The general idea is to downscale streamflow from a continental-scale or global-scale hydrological model run on a higher resolution river network and execute a raster-based hydraulic model with the streamflow inputs. The 2D subgrid version LISFLOOD-FP has been used in several studies (Schumann, 2013; Alfieri et al., 2014; Sampson, 2015). CA2D, a 2D hydraulic model that supports parallel local simulations for different river sections of a drainage network, has also been applied for global inundation mapping (Dottori, 2012; Dottori et al., 2016). A 1D kinematic wave river routing model with a rectangular channel assumption is coupled with the Variable Infiltration Capacity (VIC) Model to provide near-real time flood forecasting and inundation mapping for the

Global Flood Monitoring System (GFMS) with satellite precipitation data as the input (Wu, 2014). Another global inundation model has been developed for Global Assessment Report on Disaster Risk Reduction (GAR) (Herold and Rudari, 2013): a relative DEM was generated from HydroSHEDS with the elevation of each stream pixel set to 0. Cross sections of a predefined width were drawn on each river and used to extract elevations from the relative DEM and generate a rating curve using Manning's equation. Then the peak flows corresponding to a certain return period were translated into stage height, and corresponding inundation maps were drawn from the relative DEM. This methodology has some similarities with our proposed research. However, at the resolution of HydroSHEDS data, channels may not be adequately represented. Also, cross sections were adopted instead of evaluating reach-average properties. These are several improvements we are going to bring in the proposed study.

One point that needs to be emphasized here is that, in the past, researches compared different inundation mapping approaches in terms of the difference in the hydraulic modelling part. After computing node water surface elevations with different hydraulic models, the planar linear interpolation was applied among different nodes to obtain the flooded area. Few innovative mapping or interpolation techniques were introduced. Rainfall is not the only cause of flood, as sea-level rising (Woodruff, 2013) and subsidence (Nicholls, 1995; Dixon, 2006) also contribute. Therefore, separating the inundation mapping process from the hydrologic and hydraulic modelling process has its own rationality. Also, after reviewing the progress in recent inundation mapping, we can conclude that considering the complexity of the problem, generating inundation maps from physically-based hydrodynamic simulation at fine grid resolution ($\leqslant$ 10-meter) is not feasible in the near future for large areas. Therefore simplified 'non-physical'

inundation methods should be explored to help relieve the urgent pressure brought by flood events.

Inundation extents derived from remote sensing images have been treated as the observed truth for inundation model validation (Bates et al., 1997). Compared to imagery in other wavelengths, Synthetic Aperture Radar (SAR) imagery is most widely applied due to its all-weather capability. Several algorithms have been widely used to extract inundated areas from SAR imagery, including visual interpretation (Chambenoit et al., 2003), gray level threshold (Deshmukh and Shinde, 2005), texture histogram (Schumann et al., 2009), and active contour model (Horritt et al. 2007). However, errors may exist in the inundated extent extracted from remote sensing imagery, which can be caused by improper wavelength, inappropriate algorithms, wind roughening, protruding vegetation, and several other reasons. Therefore, recent research has started to emphasize the uncertainty existing in the SAR-derived images and explore the use of probabilistic inundation maps instead of traditional binary maps (Stephens et al., 2014). A number of image processing algorithms have been applied to generate multi-algorithm ensemble-based probability inundation maps (Schumann et al., 2009). Water elevations at flood edge estimated from remote sensing imagery have also been implemented to supplement information missing in binary flood classification (Mason et al., 2009). The Receiver Operating Characteristics (ROC)-based method has been explored for flood model calibration instead of traditional inundated zone extracted with a single threshold (Schumann et al., 2014).

The effect of raster resolution on inundation mapping has been highlighted in numerous researches; the aggregation of terrain information to generate DEMs with a resolution of 5-meter, 10-meter, and 25-meter (Werner, 2001) showed that differences

between flooded areas generated from different resolution were small except for the one created using the coarsest DEM under extreme flood events. This was due to the averaging effect of the low resolution DEM that blurred the artificial structures and made the local depression behind the structure become part of the connected flooded zone. However, even the finest-resolution DEM could not capture narrow structures such as floodwalls, which would lead to significant errors (Werner, 2001). The spatial resolution dependence of LISFLOOD has also been studied using varying resolution DEM from 10-meter to 1000-meter (Horritt and Bates, 2001b). The results show that the model reaches maximum performance at a resolution of 100 m with no significant improvement brought by higher-resolution DEMs (Horritt and Bates, 2001b). A study evaluated the use of several online DEMs for inundation mapping, including airborne interferometric synthetic aperture radar (IfSAR)-derived DEM, SRTM-derived DEM, NED and LiDA-derived DEM (Sanders, 2007). The results show that the LiDAR-derived DEM gives the most accurate prediction due to its high horizontal resolution, vertical accuracy and the capability of distinguishing bare-earth, buildings and vegetation; IfSAR DEM has adequate horizontal resolution but gridded elevations reflect building and vegetation; IfSAR and SRTM DEMs suffer from noise that may result in non-physical depressions; NED provides more smooth terrain, compared to IfSAR and SRTM, but tends to overestimate the inundated extent (Sanders, 2007).

1.2.4 Gaps in Available Knowledge

After reviewing the state-of the-art advancement in continental-scale flood forecast research, current gaps in knowledge can be summarized as follows: first, while continental-scale high-resolution meteorological and hydrological frameworks have been

established for operational purposes, efficient approaches for continental-scale high-resolution hydraulic simulation, inundation mapping, and flood impact evaluation are not available. Second, due to the lack of large-coverage detailed channel geometry data and computational instability issues existing in large-scale hydraulic models, fully-physical hydraulic models are not ready for operational execution at a continental scale. Therefore, on one hand, new methods based on continental-scale hydrological terrain analysis need to be developed to create continental-scale river geometry dataset, instead of the remotely sensing, hydraulic geometry, and local cross section collection approaches; on the other hand, a simplified alternative approach, which can translate streamflow into water depth, needs to be developed to ease the pressure brought by recent flood events. Third, after the water depth profile is created along a river, a more hydrologically coherent inundation mapping technique needs to be developed instead of planar linear interpolation, which is the current HAND method. Therefore, the implementation of HAND at a large scale needs to be explored. Fourth, more studies are needed to better understand the effect of terrain data resolution and river network accuracy on inundation mapping. Fifth, a terrain analysis workflow needs to be designed to automatically extract the channel zone of a river network and estimate the bankfull width for each river segment above which the main channel is separated from the floodplain.

1.3 PROBLEM STATEMENT

In consideration of the previously stated research needs, three research questions are addressed in this dissertation:

1. How to establish the links among discharge, water depth and flood inundation extent from the continental-scale terrain analysis products? How to combine the products

with a national high-resolution real-time stream discharge forecast system to generate a high-resolution river geometry data set and a real-time flood inundation mapping system with continental coverage based on hydrologic terrain analyses?

2. When we substitute low-resolution terrain inputs with lidar-derived high-resolution topographic information during our river geometry estimation and approximate inundation mapping practice, what kinds of change do we need to introduce to the workflow? Does the improvement in terrain inputs accuracy generally result in the improvement in river geometry and inundation extent outputs accuracy?

3. How can we automatically extract the channel zone for a large-scale river network from lidar-derived high-resolution terrain dataset? Does the workflow apply in different geomorphic settings?

1.4 SCOPE

To answer each of the research questions raised above, innovative analytical methods have been developed and tested in various cases. Different local watersheds in the United States where reference ground truth information is available are chosen during the prototype design and test process, and the contiguous United States is chosen as the test bed for the continental-scale implementation of the proposed methods.

Research question 1 will be addressed through the development of a hydrological terrain analysis workflow that derives reach-averaged channel geometry properties and generates a synthetic rating curve to relate flow to water level in a stream reach using the Height Above Nearest Drainage (HAND). Given the reach-average water depth converted through the synthetic rating curve, HAND defines the inundation zone and a water depth grid within this zone. This workflow has been implemented across the

contiguous U.S. using the 10-meter National Elevation Dataset (NED), and the integrity of the outputs has been validated through the comparison with best available references at multiple test sites.

Research question 2 uses research question 1 as a point of departure and is addressed through the development of a more comprehensive method named GeoFlood. In GeoFlood, the HAND river geometry estimation and inundation mapping component developed to answer question 1 is coupled with GeoNet, a computational tool for the automatic extraction of geomorphic channel features, to address the challenges associated with the application of the HAND method to lidar-derived high-resolution DEMs. A detailed analysis of a watershed in central Texas characterized by heterogeneous topography is performed to prove this new method. Results from this study also illustrate how the input terrain data resolution affects the accuracy of the output channel properties and inundation extent.

Research question 3 is addressed by modifying existing components and adding new functions in GeoNet, so it can be used in the hydro-flattening and bank detection practice. After all the changes have been introduced, the tool has been tested in natural, agriculture, and urban basins to approve its universality.

1.5 DISSERTATION OUTLINE

This dissertation is organized as five chapters. Chapter 1 introduces some background information about continental scale inundation mapping and river geometry estimation, summarizes the state-of-art of related research and presents three questions that will be addressed. Chapters 2-4 presents three journal drafts addressing research questions 1, 2 and 3 respectively. Chapter 5 summarizes the findings from all the studies

to answer the proposed research questions, highlights the intellectual merit of this research, and points out future objectives to be achieved.

Chapter 2: River channel geometry and rating curve estimation using Height Above the Nearest Drainage[1]

2.1 ABSTRACT

River channel geometry is an important input to hydraulic and hydrologic models. Traditional approaches to quantify river geometry have involved surveyed river cross-sections, which cannot be extended to ungauged basins. In this paper, we describe a method for developing a synthetic rating curve to relate flow to water level in a stream reach based on reach-averaged channel geometry properties developed using the Height Above Nearest Drainage (HAND) method. HAND uses a digital elevation model of the terrain and computes the elevation difference between each land surface cell and the stream bed cell to which it drains. Taking increments in water level in the stream, HAND defines the inundation zone and a water depth grid within this zone, and the channel characteristics are defined from this water depth grid. We apply our method to the Blanco River (TX) and the Tar River (NC) using 10-meter terrain data from the USGS 3DEP Elevation dataset. We evaluate the method's performance by comparing the reach-average stage-river geometry relationships and rating curves to those from calibrated HEC-RAS models and USGS gage observations. The results demonstrate that after some adjustment, the river geometry information and rating curves derived from HAND using national-coverage datasets are comparable to those obtained from hydraulic models or gage measurements. We evaluate the inundation extent and show that our approach is able to capture the majority of the FEMA 100-year floodplain.

[1]The text contained within this chapter has been submitted in Journal of American Water Resources Rssociation (JAWRA).

2.2 INTRODUCTION

Flooding is the most threatening natural disaster worldwide considering the fatalities and property damage it causes. It makes up about 40% of all natural disasters worldwide and causes about half of all natural hazard fatalities (Noji, 1991; Ohl et al., 2001). Under a changing climate, the magnitude (Knox, 1993) and frequency (Milly et al., 2002) of floods may increase significantly, which, together with growing population and expanding urbanization, results in more serious and frequent flood hazards. For the 136 coastal cities across the world alone, the annual losses due to flooding have been projected to increase to $52 billion per year by 2050 (the 2005 estimate was $6 billion) considering socio-economic impacts alone, and this number could even reach $1 trillion if other factors are considered (Hallegatte et al., 2013).

Inundation maps show the spatial extent of flooding and play an important role in emergency response during flood events (Apel et al., 2009; Maidment, 2017). Accurately mapping flood inundation extent requires a comprehensive description of the geometry of the channel and floodplain, since flooding water is routed by the river fluvial system (Maidment, 1992). Traditional approaches to quantifying river geometry rely on measurements of river cross sections. Attempts to combine many independently developed local HEC-RAS models have failed due to variations in model development, overlaps in cross sections from one local model to another, and gaps in coverage of some streams (Zheng, 2015).

Other approaches to obtaining channel geometry without introducing cross sectional information have also been investigated, such as hydraulic geometry relationships (Leopold et al., 1953), and remotely sensed imagery inference (Pavelsky and Smith, 2008). Andreadis et al., (2013) developed a simple global river bankfull width

and depth database using a regression relationship between bankfull discharge, drainage area and hydraulic geometry characteristics. Yamazaki et al., (2014) applied an algorithm that calculates the distance from a remotely-sensed water body edge to the river centerlines following flow directions, to produce the Global Width Database for Large Rivers (GWD-LR) using the SRTM Water Body Database and the HydroSHED (Hydrological data and maps based on SHuttle Elevation Derivatives at multiple scales) flow direction raster. Both bankfull width and effective river width without islands were computed for river channels between 60S and 60N (Yamazaki et al., 2014).

A so-called first fine-resolution, continental-scale river centerline and width database, the Landsat-derived North American River Width (NARWidth) dataset, has been developed (Allen and Pavelsky, 2015). It includes rivers ranging from approximately the fourth to the tenth Strahler stream order, the width of which are wider than 30 meters at annual mean discharge. Some limitations are found in these river geometry datasets: first, the resolution of the river network is not high enough to use in flooding studies of local streams. Taking Texas as an example, there are 20,004 HydroSHEDS flowlines in Texas, while the number of flowlines is 101,240 in the medium-resolution National Hydrograph Dataset Plus (NHDPlus) used in the National Water Model. Therefore, numerous local streams, which are critical during flood events, are not detected in the existing global river width and depth database. Additionally, only the bankfull width and depth are provided instead of a continuous relationship between stage height and channel properties, which limits the applicability of this dataset for inundation mapping.

While prior research using remotely sensed data or statistical approaches to investigate river geometry and rating curves has resulted in useful insights and

approaches (Getirana et al., 2013; Paris et al., 2016; Garambois et al., 2017), these methods do not extract information from the actual terrain. Relationships obtained from statistical analyses are thus insufficient to depict the unique physiographic characteristics of each channel and remotely-sensed imagery only captures part of a transient state of the river system from a top view, which is incomplete. Therefore, a new approach is needed to take advantage of the available terrain information and provide channel characteristics for ungauged basins.

This paper evaluates a new method that estimates channel geometry properties and rating curves from high-resolution terrain data. This method uses hydrological terrain analysis to determine the Height Above Nearest Drainage (HAND) (Rodda, 2005; Renno et al., 2008), which is defined as the height of each grid cell with respect to the nearest stream cell it drains to. The HAND value of each grid cell thus indicates the water height at which that cell is inundated. The inundated extent corresponding to a given water level may be determined by selecting all the cells with a HAND value less than or equal to the given level. The water depth at each cell can then be computed using the water level minus its HAND value. The applicability of HAND to inundation mapping has been demonstrated in several studies (Rodda, 2005, Nobre et al., 2016). However, its application in describing river geometry information and retrieving stage-discharge relationships has not been explored. What hydraulic simulation really needs about river geometry is not the actual channel shape but the hydraulic parameters derived from the channel shape that are then used in the mass and momentum conservation equations. Hence, if the relationships between channel hydraulic parameters and stage height can be directly derived from hydrological terrain analysis products, as suggested by the results of the work here presented, inundation mapping can be performed with an alternative

approach that does not rely on cross sectional information and hydraulic models (e.g. HEC-RAS).

This paper is organized as follows. Section 2.3 describes the workflow for the proposed approach: creation of HAND raster, evaluation of reach hydraulic properties and rating curves, and validation of the results. Section 2.4 presents a case study on the Blanco River (TX) and the comparison of the results with those obtained with a calibrated local HEC-RAS model. We also validate our approach on the Tar River (NC) against USGS gage observations and compare the resulting inundation extent against the FEMA 100-year flood plain. We discuss the results and remaining challenges in Section 2.5. Finally, concluding remarks are presented in Section 2.6.

2.3 METHODS

Our method consists of three parts. The first part is a hydrologic terrain analysis workflow, which is modified from the original HAND method (Renno et al., 2008), to compute the HAND raster for the NHDPlus river network. In the second part, using the calculated HAND raster, we derive hydraulic properties for all the reaches in the river network. In the third part, we take the derived hydraulic geometry and create a synthetic rating curve using Manning's equation for each reach. Following these steps, we compare the HAND-derived results to channel geometry and rating curves derived from local HEC-RAS models.

2.3.1 Hydrologic Terrain Analysis

The Height Above Nearest Drainage (HAND), first introduced by Rennó et al. (2008), is a special case of a hydrologic terrain proximity measure (Tesfa et al., 2011). There are multiple approaches to represent topography-driven flow over a terrain

represented by a digital elevation model (DEM). The D8 model (O'Callaghan et al., 1984) assigns a single flow direction from each grid cell to one of its neighbors based on the steepest descent direction. It is the earliest and simplest method developed and is still widely used due to its simplicity and the convergence of the flows, which is desirable when mapping stream flow paths. The D∞ model introduced by Tarboton (1997) generalizes D8 by representing the flow direction as a vector along the direction of the steepest downward slope on one of the eight triangular facets centered at each grid cell. Flow from a grid cell is shared between the two downslope grid cells closest to the vector flow angle based on angle proportioning (Figure 2.1). Taking the advantage of the D∞ flow model, Tesfa et al. (2011) developed methods to derive a wide range of flow related quantities useful to hydrological and environmental modeling, including the calculation of distance to stream (horizontal or vertical). The TauDEM software (Tarboton, 2016) implements these methods. Our method uses the D∞ approach for the computation of HAND (vertical distance or drop to a stream, see Figure 2.2) as implemented in the TauDEM software.

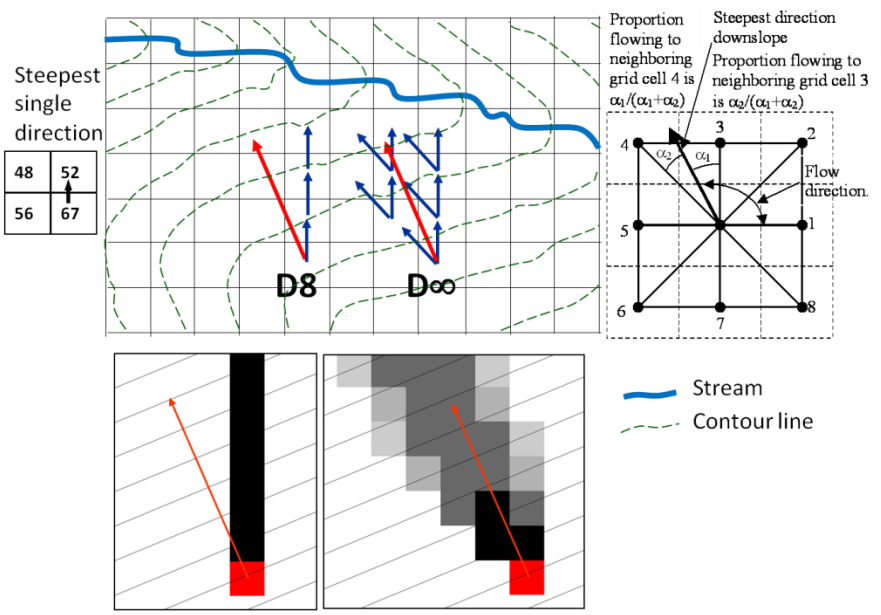

Figure 2.1: The D8 and D∞ flow models (figure reproduced from Tesfa et al., 2011).

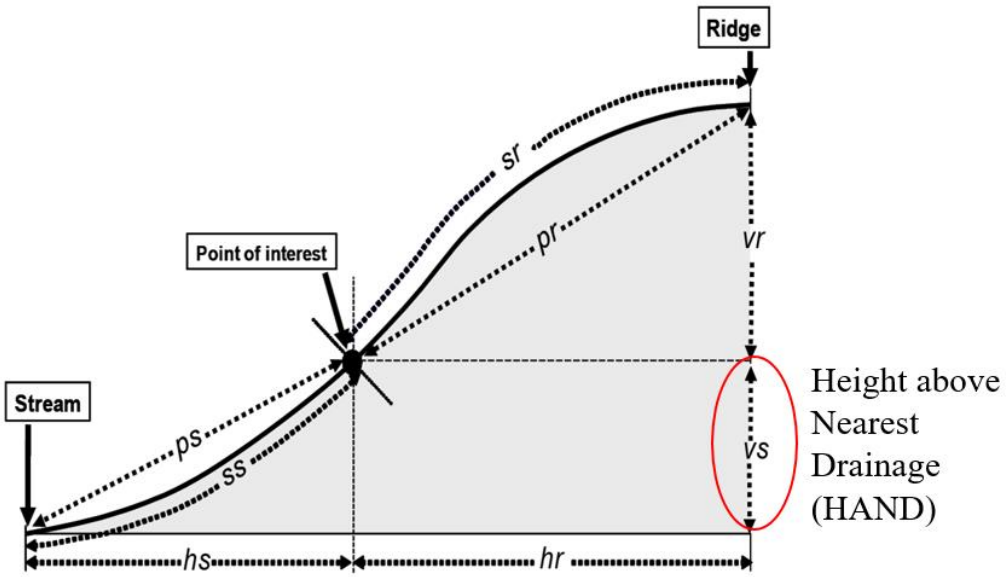

Figure 2.2: Definition of proximity measures for distances up (to ridge) and down to stream. HAND is evaluated using *vs*, the vertical drop to stream. (figure reproduced from Tesfa et al. (2011)).

The vertical drop to a stream (i.e., the HAND value) is computed as:

$$h(i) = \frac{(\sum P_{ik}(drop(i,k) + h(k))}{\sum P_{ik}} \quad (2.1)$$

where P_{ik} is the proportion of grid cell *i* that drains to grid cell *k*, *h* is the vertical drop from a grid cell to the stream, and *drop(i,k)* the drop (change in elevation) from grid cell *i* to *k* defined as:

$$drop(i,k) = z(i) - z(k) \quad (2.2)$$

where *z* represents the elevation values at grid cells *i* and *k*. In Equation (2.1) the sum is over the grid cells for which P_{ik} is greater than 0 and for which $h(k)$ exists. The denominator in (2.1) is used to normalize for flow paths that leave the domain without reaching a designated end point grid cell (there is an option implemented in the code (Tarboton, 2016) to report no data rather than use this normalization). Tesfa et al. (2011) present this function as one option within a general distance to target set function where $drop(i,k)$ may be replaced by a general distance measure computed in any number of ways (e.g. horizontally, vertically or along the slope). Note that drop to stream expressed in these equations is defined recursively with the drop from any grid cell as the weighted average of the drop from downslope cells, using cell to cell flow proportions as weights. The result is thus a form of weighted average along all the flow paths from a cell to the stream. The computation is initiated by setting the distances to 0 for all stream cells, and then enabling the evaluation of vs (i.e. HAND) for cells for which all downslope quantities in the domain have been evaluated. Grid cells where all downslope values are available are placed on a computational queue. To enable parallel computation, the domain is decomposed into portions, and a queue maintained for separate processes operating on each of them. Computational details are given in Tesfa et al. (2011).

The D∞ approach with weighted average distance to the stream is used here as it provides a smoothing of the HAND values, effectively averaging sharp HAND differences between adjacent grid cells that may drain to stream cells of different elevation resulting from the D8 approach. This approach appears to better represent the spreading out of water over the terrain when HAND is used to evaluate flood inundation and channel hydraulic properties.

A prerequisite for evaluating HAND is a raster representation of the stream network. These are stream grid cells where HAND is assigned to be 0. The TauDEM D∞ distance down function may actually be evaluated for any target zone represented by a set of grid cells to which the distance is to be computed for whatever purpose. However, in the evaluation of HAND, the target zone is a raster representation of the stream network. There are many approaches to the definition of a raster stream network based on DEM flow models. These generally use the D8 method, as defining divergent stream networks is impractical. TauDEM implements a number of methods (Tarboton and Ames, 2001; Tarboton et al., 1992; Tarboton et al., 1991), including simple contributing area threshold methods and more advanced methods based on measures of curvature to identify valley grid cells, objectively adapt to the complexity of the topography, and quantify drainage density.

In this paper, our interest is in stream networks aligned with the NHDPlus dataset used by the National Water Model. The NHDPlus stream network was mapped at a nominal 1:100,000 resolution. The USGS National Elevation Dataset (NED) DEM is currently available at 1/3 arc sec (~10 m) horizontal resolution across the continental US and represents information at a finer resolution more consistent with 1:24,000 scale mapping.

NHDPlus streams, however, do not always align with valleys in the 1/3 arc sec NED DEM. To avoid the spurious HAND values that would result from calculating HAND to a direct rasterization of NHDPlus flowlines, we derived a stream raster at the same drainage density as the NHDPlus stream network, but aligned with 1/3 arc sec NED DEM. This operation was performed by identifying the upstream channel head of each first order NHDPlus stream and representing this as a grid cell with value of 1, and setting all other grid cells to a value of 0 in a stream source weight grid. This weight grid was then used as input to a weighted flow accumulation calculation using D8 flow directions (TauDEM areaD8 function). Stream grid cells were mapped where the weighted flow accumulation was greater than 1. The result is a raster representation of a stream network originating at each source point, but following down the valleys as indicated in the 1/3 arc sec DEM (Figure 2.3). This stream raster was used as the target set in the evaluation of vertical distance using the TauDEM distance down function to obtain HAND values (Figure 2.4).

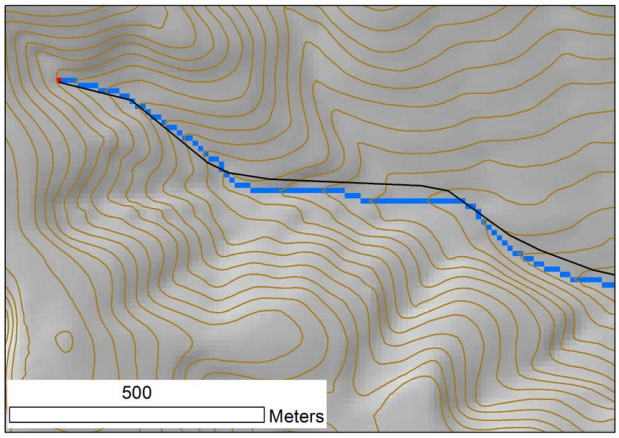

Figure 2.3: Stream raster derived from channel head sources of NHDPlus medium resolution streams. The red grid cell is the channel head source grid cell. Blue grid cells are the stream raster evaluated as a weighted flow accumulation of such red grid cells. The black line is NHDPlus stream. The lines are overlaid on elevation contoured at 2m interval. The horizontal offset between the NHDPlus streams and the valleys as depicted by contours from the 1/3 arc sec NED DEM is corrected in the stream raster.

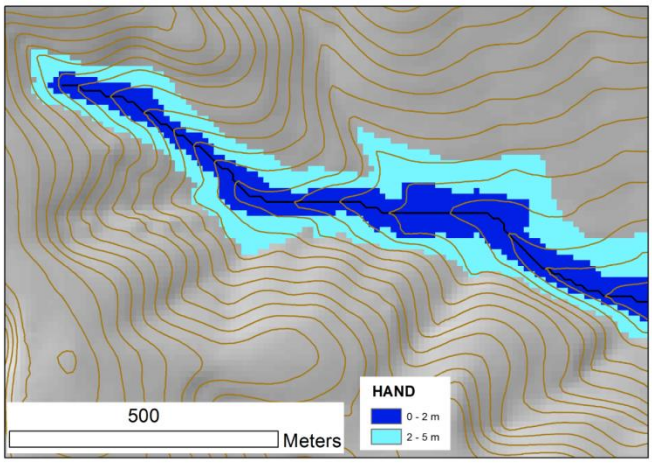

Figure 2.4: Height Above Nearest Drainage (HAND) evaluated on 1/3 arc sec NED DEM relative to a stream raster derived from NHDPlus medium resolution stream network source grid cells. 2m terrain contour interval is drawn as background.

Implementation of the above methods requires a DEM that is hydrologically conditioned, or has had the pits removed so that each grid cell can drain to the edge of the domain, or to an identified internally draining sink along a flow path that is not increasing. In this work, the TauDEM pitremove function was used to hydrologically condition the DEM prior to the analysis.

The complete set of hydrologic terrain analysis processing steps is:

1. Fill pits using TauDEM pitremove function.
2. Calculate D8 flow directions using TauDEM d8flowdir function.
3. Calculate D∞ flow directions using TauDEM dinfflowdir function.
4. Define channel head source grid cells from NHDPlus streams.
5. Calculate the weighted flow accumulation using channel head grid cells as input to TauDEM D8 contributing area function.
6. Define the stream raster using a threshold of 1 with weighted flow accumulation.
7. Calculate HAND using D∞ distance to stream function with the vertical drop option.

2.3.2 River Geometry and Rating Curve Estimation

The conceptual basis for implementing HAND in inundation mapping is as follows. A river segment is defined as a stream reach *R*. The reach catchment, *C*, contributes the local drainage area of the stream reach *R*. Let us define *L* as the length of the reach *R* measured along its thalweg line. A measure location, *m*, along reach *R* is defined by its percentage distance from the lower end of the reach, or in other words by the ratio of the length from that location to the lower end of the reach, divided by the

length of the reach *L*. The water level, *y*, at any location m along the stream channel is given by the difference between the water surface elevation and the minimum channel elevation at that location, designated by *y(m)*. The average water level along the stream reach is given by *y*. The HAND value, *h(s)*, is the elevation difference between a cell, *s*, on the land surface within the reach catchment and the minimum channel elevation at the location on the corresponding stream reach where water draining from that cell converges into the channel. The location, *s*, on the land surface is inundated if the water level in the channel reach is greater than the HAND value of that location, i.e. inundation occurs if $y > h(s)$.

The conceptual basis for implementing HAND to estimate the channel hydraulic properties (Figure 2.5) and rating curve is as follows: for reach *R* at water level *y*, all the cells *s* with a HAND value smaller than *y* compose the inundated zone *F(y)*, which is a subarea of the reach catchment *C*. The water depth at any cell *s* in the inundated zone, *d(s)*, is the difference between the reach-average water level *y* and the HAND of that cell *h(s)*, which can be represented as:

$$d(s, y) = y - h(s), s \in F(y) \tag{2.3}$$

Since a uniform reach-average water level *y* is applied to check the inundation of any cell within the catchment, the inundated zone *F(y)* refers to that reach level.

The water surface area of the inundated zone at a water depth of y, *S(y)*, can be calculated as:

$$S(y) = \sum_{s \in F(y)} A(s) \tag{2.4}$$

where *A(s)* is the area of cell *s*.

The channel bed area of the inundated zone at a water depth of *y*, *B(y)*, can be calculated as:

$$B(y) = \sum_{s \in F(y)} A(s)\sqrt{(1 + slp(s)^2)} \tag{2.5}$$

where *slp(s)* is the surface slope of cell *s*, expressed as rise over run or inverse tangent of the slope angle. This equation approximates the surface area of the grid cell as the area of the planar surface with surface slope, which intersects with the horizontal projected area of the grid cell.

The flood volume of the inundated zone *V(y)* at a water depth of *y* can be calculated as:

$$V(y) = \sum_{s \in F(y)} A(s)\ d(s, y) \tag{2.6}$$

If the reach length *L* is known, the reach-average channel width at a water depth of *y*, *W(y)*, can be calculated as:

$$W(y) = S(y)/L \tag{2.7}$$

Similarly for the reach-average cross section area *A(y)*:

$$A(y) = V(y)/L \tag{2.8}$$

and the reach-average cross section wetted perimeter *P(y)* :

$$P(y) = B(y)/L \tag{2.9}$$

Combining the reach-average cross-sectional area *A(y)* and the wetted perimeter *P(y)* gives the reach-average cross section hydraulic radius *R(y)* as:

$$R(y) = A(y)/P(y) \tag{2.10}$$

If the channel bed slope of reach *R* is *S* and a Manning's value is assumed as *n*, the Manning's equation can be applied to obtain a discharge *Q(y)* corresponding to the water depth of *y* at uniform flow as (in metric units):

$$Q(y) = \left(\frac{1.00}{n}\right) A R^{\frac{2}{3}} S^{\frac{1}{2}} \tag{2.11}$$

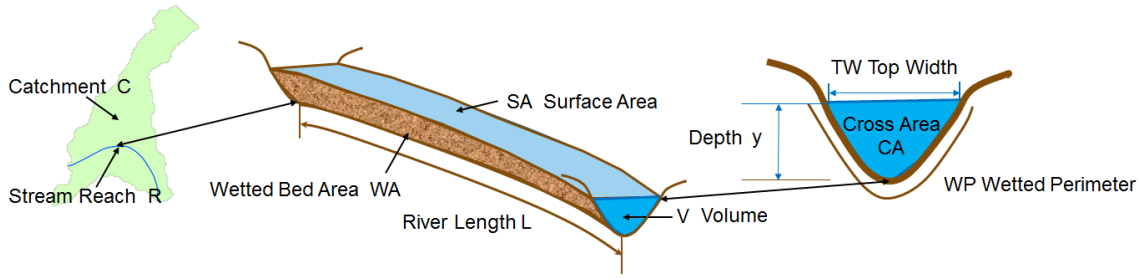

Figure 2.5: The conceptual model of HAND river geometry.

Computing the discharge $Q(y)$ for different water depths y results in a synthetic rating curve for reach R. This rating curve relates the average water depth to the discharge in the reach $y(Q)$, where the discharge is assumed to be uniform along the reach. Therefore, this synthetic rating curve can be used as a tool to convert forecast discharges generated by large scale hydrologic models into corresponding water depths.

We implement this conceptual framework in the continental U.S with the 1/3 arc sec (10-meter) USGS 3DEP Elevation dataset and the NHDPlus dataset (Liu et al., 2018). The reach length and channel bed slope come from the attribute table of the flowline feature class in the NHDPlus dataset. By conducting these computational steps, a new continental-coverage high-resolution channel property dataset can be obtained for the continental U.S., indexed by the NHDPlus Common Identifier (ComId), and can be used to support future continental river dynamics research.

2.3.3 Integrity Checking of River Geometry and Rating Curves

The river channel geometries and synthetic rating curves defined using HAND are averages over the length of a channel reach derived by slicing the terrain surface longitudinally along the channel flow path, rather than transversely to the flow path, at intervals to form individual cross-sections, as is traditionally done in one dimensional

river hydraulic models. One way of checking the integrity of the HAND-derived information is to compare the results with those derived from a HEC-RAS model of the same river. Therefore, we compare: (i) the minimum channel elevation, (ii) the stream geometry, and (iii) the synthetic rating curve.

The minimum channel elevation at a particular measure location m, $z_c(m)$, is the elevation above geodetic datum of the stream thalweg at that location. When a stream is represented by a sequence of cells in a DEM, the DEM cell that corresponds to location mi has a DEM channel elevation above geodetic datum of $z_d(m)$. Because digital elevation models are smoothed versions of land surface topography, and because the digital elevation model may have been created when the channel was partly filled with water, the DEM channel elevation is generally higher than the minimum channel elevation. The value $\Delta z(m) = z_d(m) - z_c(m)$ represents the bed elevation difference between the DEM channel elevation and the thalweg channel elevation at that location. The mean value of this bed elevation difference along a stream reach is given by Δz.

An assumption of our implementation that needs to be evaluated is whether a DEM at a resolution of 10 meters is able to capture the terrain details within the channel. One way of carrying out this evaluation is to compare the streamline bed elevation profile extracted from the 10m DEM with the minimum channel elevation in a HEC-RAS model obtained by connecting the minimum elevation of HEC-RAS cross sections from upstream to downstream. In order to keep the same profile length and elevation sampling rate in the two methods, we adopt the streamline measure system of the HEC-RAS model, and obtain the DEM-derived profile by intersecting the DEM-derived flowline with the HEC-RAS cross sections and extracting the DEM elevations of the intersected locations.

Because Δz is generally greater than zero, it is useful to introduce a bottom shift into the HAND-derived water levels reflecting the "shelf effect" where the bottom of a DEM channel is actually flat over a finite area. Using this approach, the channel width W is a positive number when the water level y is zero, so the true water depth is larger than that computed using the DEM alone.

HAND-derived channel hydraulic properties can also be compared with those derived from river geometry information stored in HEC-RAS models. The main channel property that we evaluated is the channel width, because it is a description of the river geometry that is readily obtained by the HAND method. To do this, we derive a water level-channel width relationship from the HAND raster for a river segment using Eq. (2.7). Since the cross section shape is stored in HEC-RAS, a similar relationship can be established from the shape of each cross section located on the study reach. These cross section level-width relationships form a sample space for a given stream reach. If the HAND-derived relationship falls within this sample space, we have some confidence that the accuracy of the HAND-derived river geometry information is comparable to that of the river geometry data used in local hydraulic simulations. Taking the channel widths for all the cross sections on the segment at the same water level, together with the distance between adjacent cross sections, we can compute the flood volume corresponding to the given water depth. If the volume is divided by the total length of the segment, an equivalent reach-averaged channel width can be derived from these cross sectional shapes. Repeating this process for a series of threshold water depths gives us a reach-averaged water level-width relationship derived from cross sectional shapes. Calculating the difference between this cross section-derived relationship and the HAND-derived

relationship also helps to evaluate the quality of HAND-derived river geometry information.

Finally, HAND-derived rating curves are compared with the rating curves stored in local HEC-RAS models. If a HEC-RAS project contains the simulation at multiple flow conditions, a rating curve will be generated for each cross section from the steady flow simulation results. Similar to the channel width sample space we use to validate river geometry, a rating curve sample space for the river segment is established from rating curves from different cross sections. To better quantify the water depth uncertainty brought by channel geometry, a fixed flow rate is assigned to every cross section in a HEC-RAS model for a given channel reach to create a representative flow condition that is replicated with the HAND-derived rating curve. In this way, the water depth uncertainty caused by the difference in discharge between HAND and HEC-RAS is eliminated. This median rating curve in the rating curve sample space from HEC-RAS is chosen as the reference to validate the HAND-derived rating curves. The optimal roughness value is selected for the HAND-derived rating curve by minimizing the root-mean-square error (RMSE) between the HAND-derived rating curve and the median rating curve from HEC-RAS.

2.4 APPLICATIONS

2.4.1 Study Area and Data

In order to evaluate our approach, we conduct a case study on the Blanco River (Figure 2.6) following the steps described in the Methods section. The Blanco River is located in Central Texas, which is one of the most flash-flood prone regions in North America. In May 2015, a historic flash flood occurred across parts of Central Texas

causing severe life and property losses. The Blanco River was one of the most affected areas in this flood due to a flood wave of more than 12 meters in water depth.

The network of the Blanco River watershed is composed of 170 medium-resolution NHDPlus reaches. The total drainage area is about 1,100 km^2, and the average drainage area of the individual reach catchments is 6.7 km^2. The total river length is about 540 km, and the average river length of the reaches is 3.2 km. For the hydrological terrain analysis portion, we created the HAND raster for the Blanco River watershed. The DEM used in this study is the 1/3 arc-second DEM from the USGS 3DEP Elevation dataset with horizontal resolution of about 10 meters. The RMSE is 1.5 meters and represents the vertical accuracy of the DEM (Gesch et al., 2014). A calibrated HEC-RAS steady flow model, covering the lower half of the Blanco River main channel, was provided by the Fort Worth District of the U.S. Army Corps of Engineers and used as the reference for river geometry and rating curve comparison. In particular, we implemented the approach for a single NHDPlus reach with COMID 1630223. We chose this reach because: (1) its length is close to the average river length of the entire NHDPlus network with 2.67 million reaches, making it a representative reach for the catchment; (2) the reach is covered by the local HEC-RAS model and there are 8 cross sections lying on this reach; and (3) the reach is close to Wimberley where 11 people were killed in the 2015 Memorial Day Flood, adding practical significance to understanding this reach.

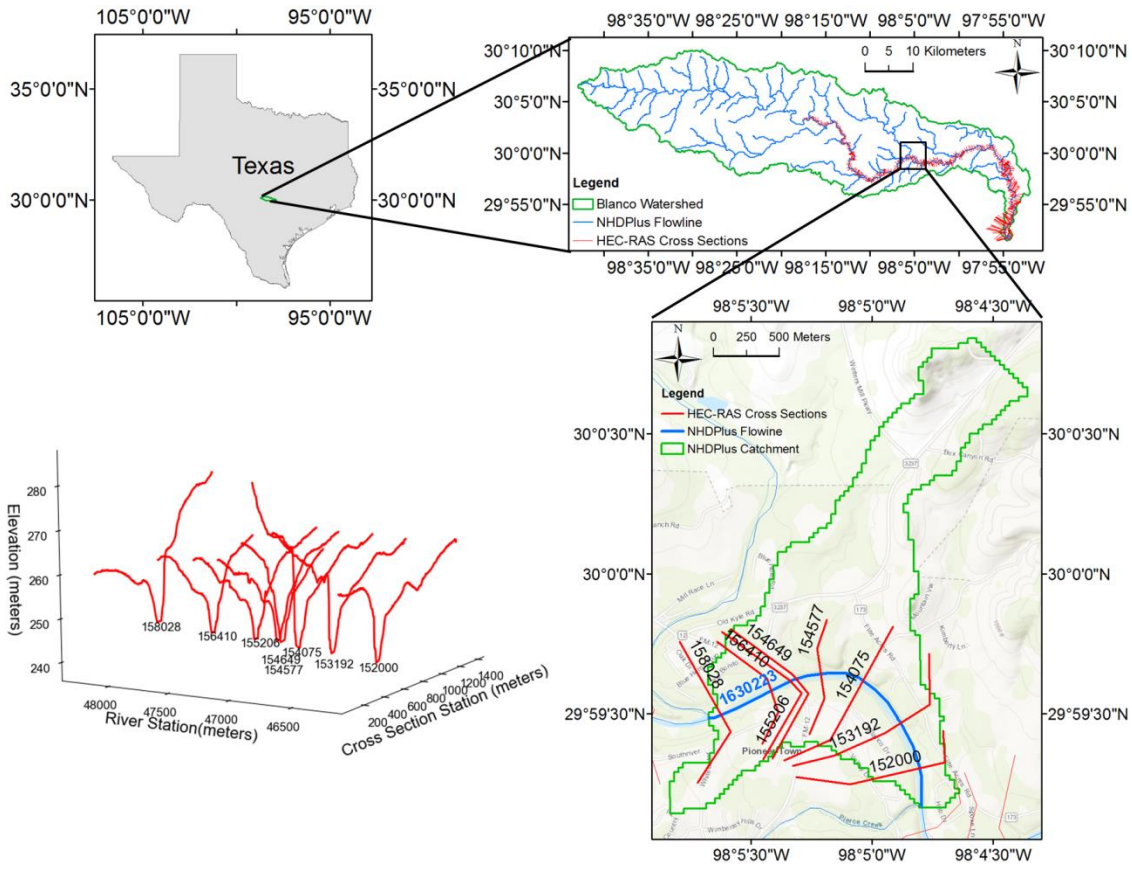

Figure 2.6: The Blanco River watershed, NHDPlus reach 1630223, and the geometry of HEC-RAS cross sections located on the reach.

The eight HEC-RAS cross sections are also shown in Figure 6. The main channel Manning's n value is 0.045 for all the cross sections, while the floodplain Manning's n varies from 0.06 to 0.1. The Manning's n values applied in the HEC-RAS model provide a proper range for roughness adoption when the depth-discharge relationship (rating curve) is established through HAND.

2.4.2 Hydrologic Terrain Analysis

A 10-meter HAND raster (Figure 2.7) was generated for the Blanco River watershed based on the 10-m resolution DEM raster and the 10-meter river network raster initiated at NHDPlus stream sources. While the original DEM has elevations that range from 165 meters to 618 meters, a difference of 453 meters, the HAND raster ranges from 0 to 161 meters. This difference in elevation range shows that HAND measures only the relief relative to streams.

In addition, since the HAND raster is built upon flow directions, derived from a hydrologically conditioned DEM, it forms a continuous surface across the whole domain. This continuity brings two advantages to the HAND method over the planar linear interpolation approach used for inundation mapping based on cross sections (Apel et al., 2009): (1) local depressions that are never connected to the flow can be avoided; and (2) the mass conservation law holds.

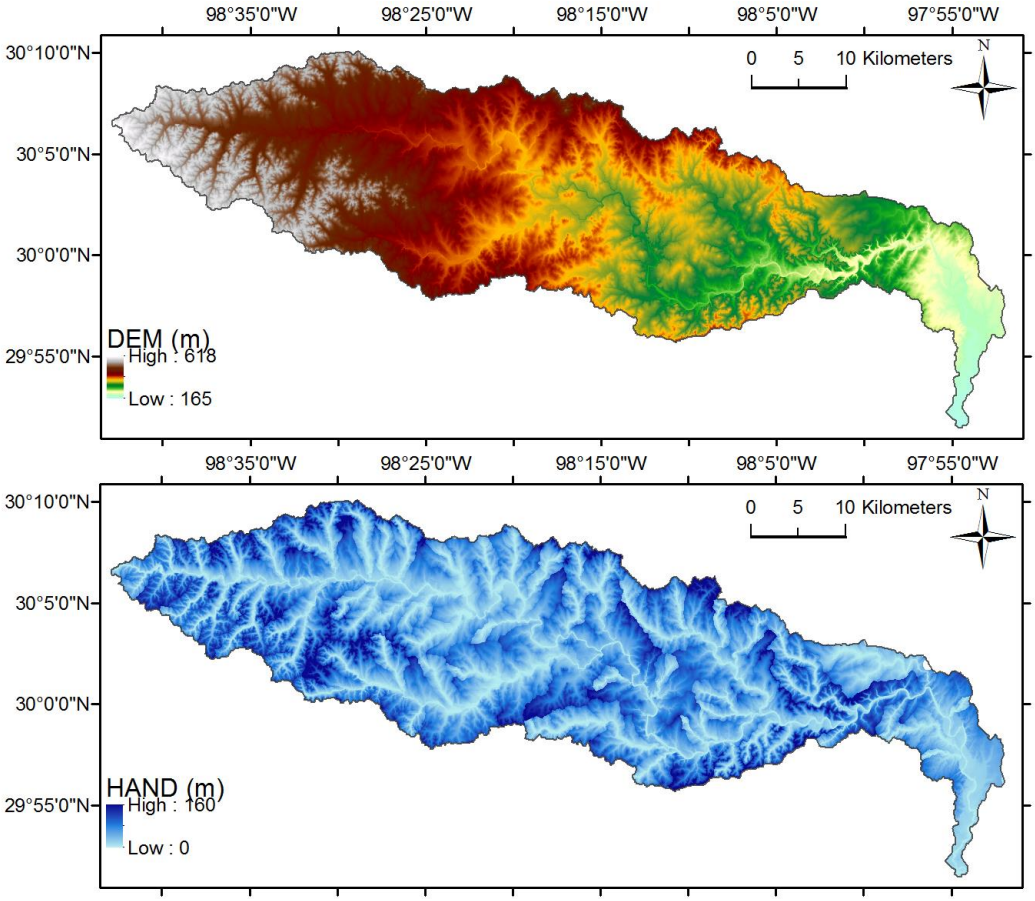

Figure 2.7: DEM and HAND for the Blanco River watershed.

Figure 2.8 illustrates the stream network and NHDPlus channel heads used to define the stream network raster for the Blanco River watershed. The blue polylines are from the NHDPlus flowline feature class. A geoprocessing tool was used to identify the channel heads of all the first-order reaches. The cells on the flow paths starting from these channel heads following the D8 flow directions were identified as stream cells. Although the majority of the DEM-derived flowlines line up with the NHDPlus flowline features, the advantage of adopting DEM-derived flowlines instead of NHDPlus

flowlines is that it guarantees that the streams pass through the valley portion of the digital terrain dataset.

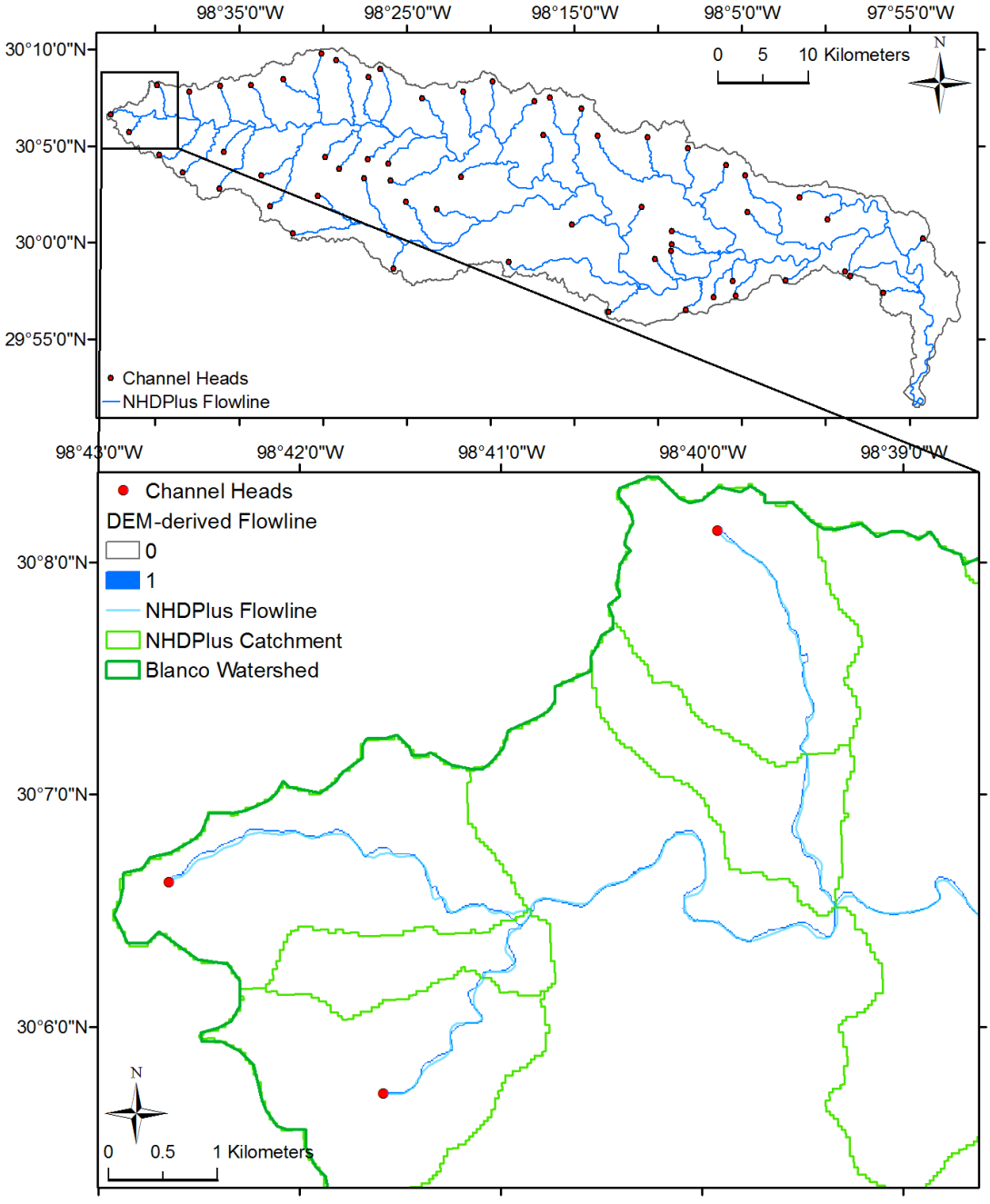

Figure 2.8: Stream definition in HAND.

2.4.3 River Geometry and Rating Curve Estimation

By setting a water level threshold to the HAND raster, the inundation extent consisting of all the cells with a HAND value smaller than the threshold can be generated. The water depth raster is then computed by using the threshold water level value subtracted from the HAND value (Eq. (2.3)). All the inundated cells have a positive water depth and the stream cells have a water depth equal to the threshold water level.

The procedure for obtaining river geometry properties for each reach is illustrated here for the selected study reach and catchment (COMID: 1630223). We first clip the Blanco River watershed HAND raster with the catchment boundary polygon to obtain a HAND subset for that catchment. From the HAND raster, we create the water depth grids that correspond to a series of threshold water levels from 0 to 18.3 meters (60 feet) at an interval of 0.3 meters (1 foot). As shown in Figure 2.9, water spreads out of the channel and the depth at the same location increases as the water level rises up. Following the method described earlier, we get the water level-channel geometric property relationships for this reach as shown in Table 2.1.

To estimate the rating curve for that reach, the derived water level-cross sectional area and water level-hydraulic radius relationships, together with the river length and reach average slope attributes of that specific reach from the NHDPlus dataset and Manning's roughness coefficient, are substituted into the Manning's flow resistance equation. In this study for reach 1630223, the segment length is 2.1 kilometers, and the channel bed slope is 0.00198. Manning's n value was taken as 0.05 for consistency with the HEC-RAS model for this river. Selection of Manning's n is a source of uncertainty in this approach and its calibration is discussed in the validation section.

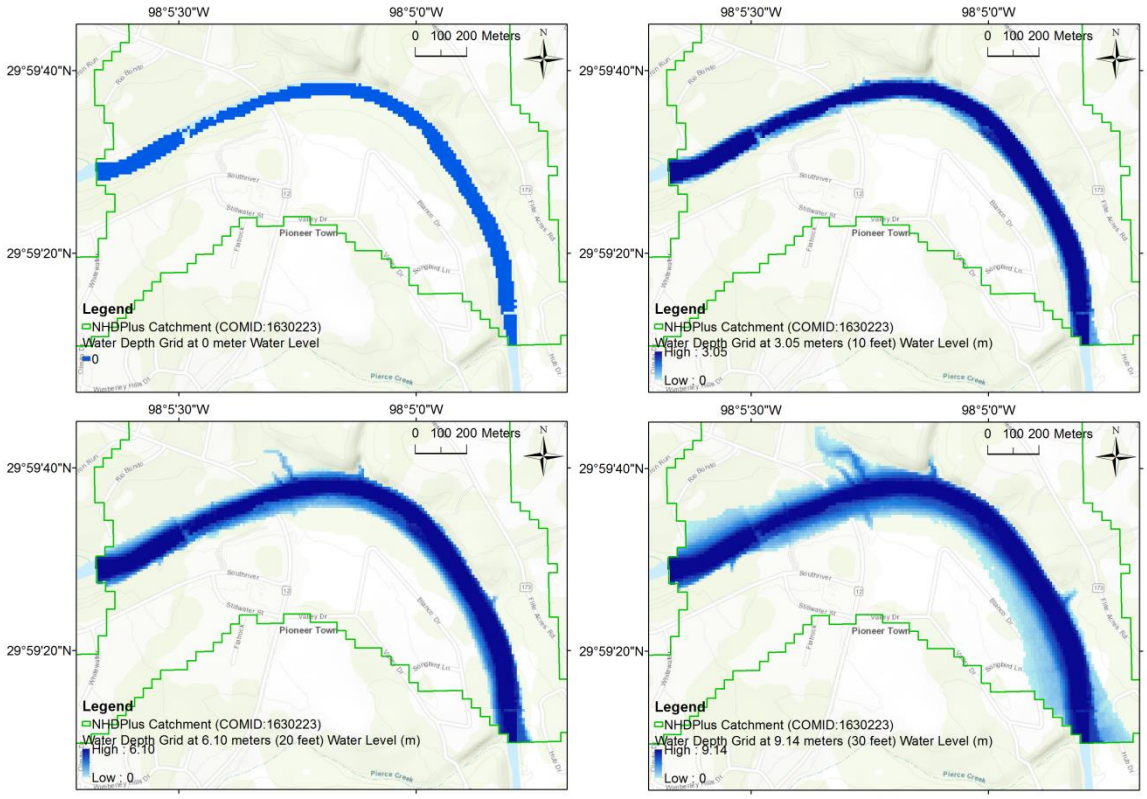

Figure 2.9: Water depth grids at different water levels (0, 3.05, 6.10, and 9.14 meters, respectively).

Table 2.1: HAND-derived river geometry parameters and rating curve for reach 1630223.

Water Level (m)	Water Surface Area (10^4 m^2)	Channel Bed Area (10^4 m^2)	Flood Volume (10^4 m^3)	Channel Width (m)	Wetted Perimeter (m)	Wet Area (m2)	Hydraulic Radius (m)	Discharge (m^3/s)
0	8	8	0	38	38	0	0	0
3.048	16	16	37	77	78	181	2.32	282
6.096	22	22	95	107	108	463	4.29	1085
9.144	33	34	176	163	164	856	5.21	2286
12.192	55	56	312	270	272	1516	5.57	4236
15.240	77	77	514	373	377	2501	6.64	7856
18.288	100	101	781	488	493	3801	7.71	13190
21.336	123	124	1124	600	605	5467	9.04	21093
24.384	146	147	1534	711	716	7467	10.43	31682

Theoretically, when the water level is equal to zero, the channel is represented by a thalweg line with a width of zero. However, from Figure 2.9(a) and the zero depth row in Table 2.1, we can see that there is a bottom width of 38 meters in the HAND-derived river geometry, meaning that the HAND-derived river geometry is not able to reach down to the level of the thalweg. Therefore, a shift must be made to the bottom of the HAND-derived river geometry information.

2.4.4 River Geometry and Rating Curve Validation with HEC-RAS

To evaluate the 10-meter terrain dataset used to estimate river geometry, a streamline profile comparison was conducted for the whole modelled river segment and the single reach 1630223. For the profile comparison of reach 1630223 (shown in Figure 2.10(a)), the DEM-derived profile is 0.13 meters higher than the HEC-RAS profile on average with a standard deviation of 0.12 meters. The profile derived from the pit-removed DEM, which is the actual one used in HAND computation, is 0.88 meters higher than the HEC-RAS profile on average, with a standard deviation of 0.95 meters. The results show that for this reach, the 10-meter DEM is very close to the thalweg, but the pit filling process introduces extra bias to the accuracy of the terrain dataset, and affects the accuracy of HAND results. The same comparison is repeated for the entire profile across the modelled channel shown as Figure 2.10(b) and the same conclusion can be drawn. For the entire 82-kilometer modelled segment, the DEM-derived profile is 0.49 meters higher than the HEC-RAS profile on average with a standard deviation of 1.23 meters; the profile derived from the pit-removed DEM is 0.99 meters higher than the HEC-RAS profile on average with a standard deviation of 1.26 meters.

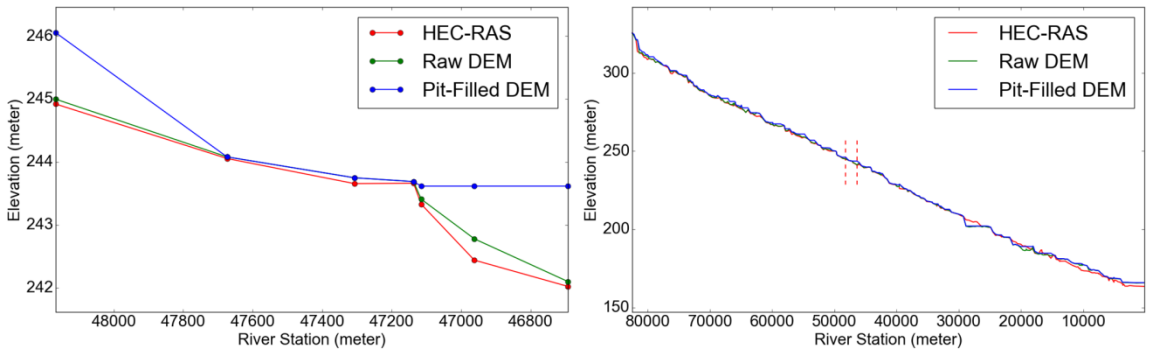

Figure 2.10: Comparison between the minimum channel elevation profiles from the DEM, the pit-filled DEM, and HEC-RAS streamline profile comparison.

To validate the HAND-derived river geometry, we computed a water level-channel width relationship for each cross section and a reach-average relationship, depending on cross sectional shapes and distances. These relationships compose the validation reference (shown by the dotted red line in Figure 2.11) derived from the HEC-RAS model. According to Table 2.1, when the water depth is zero, a corresponding channel width of 38-meter is derived from the HAND raster for reach 1630223. From Figure 2.11, a depth of 0.64 meters is interpolated on the reach-average water level-width relationship for a 38-meter channel width. This depth is treated as the bottom shift needed to adjust HAND-derived river geometry in this reach due to the limitation caused by the terrain dataset resolution. After the adjustment is made, the comparison between HAND-derived depth-width relationship and HEC-RAS-derived depth-width relationship is shown as Figure 2.11. As we can see, the HAND-derived depth-width relationship always falls in the sample space composed of individual cross section depth-width relationships. The RAS-derived reach-average channel width is 12.04 meters wider than the HAND-derived reach average width on is within the depth range from 0.92 meters (3 feet) to

15.24 meters (50 feet). The standard deviation of the width difference is 19.33 meters. If the difference is normalized with the RAS-derived reach-average channel width in that range, the relative mean difference is 3.2 percent, which demonstrates a good fit of the HAND-derived river geometry to the actual channel hydraulic condition.

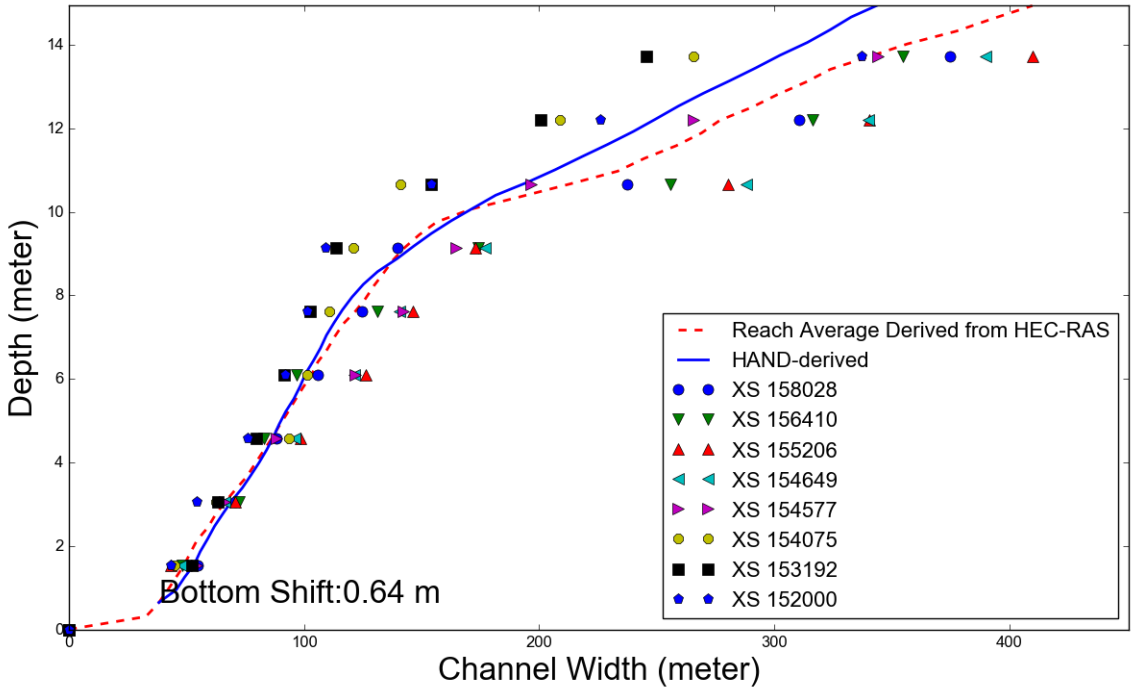

Figure 2.11: Comparison between HAND-derived and RAS-derived depth-width relationships on reach 1630223 ("XS" stands for "Cross Section". The distribution and geometry of cross sections can be found in Figure 2.6).

To validate the rating curves derived with HAND, we conducted steady flow simulation with HEC-RAS under multiple flow conditions. In each cross section, the water level-discharge data pair under a single flow condition is a point on the rating curve of that cross section and the rating curves of all the cross sections in a reach compose the reference rating curve sample space. There are eight flow conditions (profiles) stored in

the approved HEC-RAS model, which correspond to the 2-yr (232 m^3/s), 5-yr (736 m^3/s), 10-yr (1249 m^3/s), 25-yr (2067 m^3/s), 50-yr (2784 m^3/s), 100-yr (3568 m^3/s), 250-yr (4701 m^3/s), and 500-yr (5607 m^3/s) floods in the Blanco River. To better represent the depth-discharge relationship in low flow condition, we added six extra profiles. One of these profiles is the annual mean flow condition (2 m^3/s), which is stored as an attribute of every reach in the NHDPlus flowline attribute table. The other three profiles correspond to 20% (0.4 m^3/s), 50% (1 $m^{3/}s$) and 80% (1.6 m^3/s) mean annual flow. The last two profiles (79 m^3/s and 155 m^3/s) are obtained by linearly interpolating between the annual mean flow and the 2-yr flood. The downstream boundary condition of the steady flow simulation is set as the normal depth. Since we set a constant flow rate to all the cross sections across the reach, for each flow condition, a box plot can be used to quantify the variability in stage across the cross sections due to shape differences and other hydraulic interactions. Connecting the median stage of each box plot produces a median rating curve. This median rating curve is applied to identify the corresponding discharge for the channel bottom missing in the HAND-derived river geometry and rating curve. For the depth shift of 0.64 m, the discharge added to the bottom of the HAND-derived rating curve is 22 m^3/s. Then the entire HAND-derived rating curve is shifted with a depth of 0.64 m and a discharge of 22 m^3/s. Figure 2.12 shows the comparison between the HAND-derived rating curve (after shift) and the HEC-RAS rating curve sample space. The Manning's n roughness value used to build this rating curve is 0.05. Flow conditions larger than the minimum discharge in HAND-rating curve are used to quantify the fitness of HAND-derived rating curve and the reference median rating curve. Therefore, 10 of these 14 flow conditions are adopted. For those specific flow rates, corresponding stage heights are obtained from the HAND-derived rating curve and the

HEC-RAS median rating curve. For the case with the Manning's n of 0.05, the water level read from the HAND-derived rating curve is 0.52 meters higher than the stage height read from the HEC-RAS median rating curve on average with a standard deviation of 0.09. If the difference is normalized using the median stage height, it represents a mean difference of 7.7 percent.

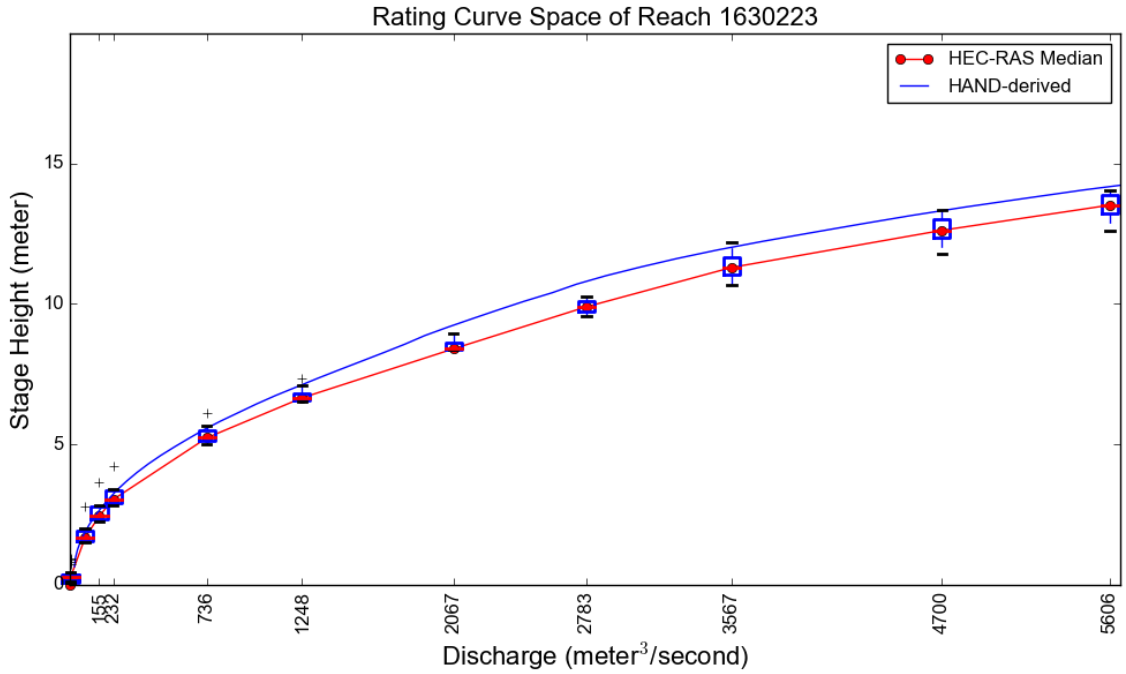

Figure 2.12: Comparison between HAND-derived and RAS-derived rating curves on reach 1630223 (n=0.05).

The optimal roughness value is determined by minimizing the mean stage height difference in absolute value for the given flow conditions searching across Manning's n values between 0.040 and 0.06 at an interval of 0.001. The variation of the mean stage height difference within this range is shown in Figure 2.13. The mean stage height difference absolute value is minimized to 0.02 meters at a Manning's n of 0.043, which is

slightly smaller than the channel roughness value used in the HEC-RAS model (0.045). This difference is inconsequential. If the actual 0.045 Manning's n value is adopted, the mean difference is 0.17 meters, which is an acceptable conversion for inundation mapping purposes. The rating curve comparison with the Manning's n of 0.045 is shown in Figure 2.14. The fact that the calibrated and HEC-RAS n values are close and the rating curves consistent, supports the finding that the HAND DEM analysis is a valid approach to determine hydraulic parameters and is expected to produce results comparable to the more data intensive HEC-RAS approach, which is difficult to apply at continental scale.

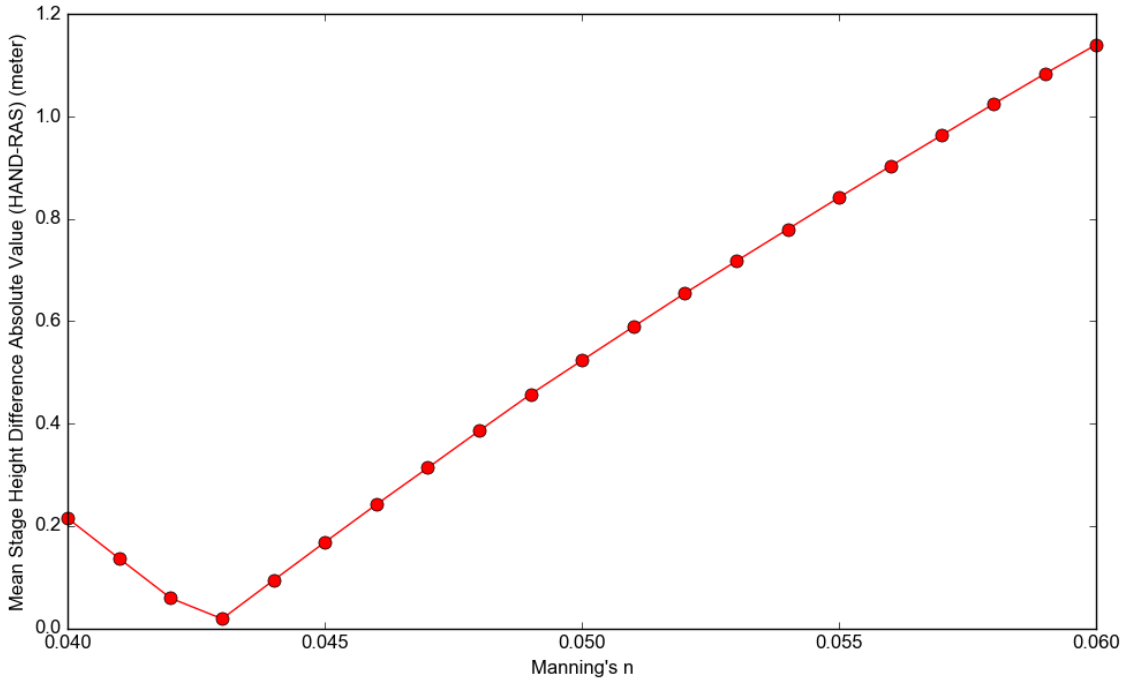

Figure 2.13: Relationship between Manning's n and the mean stage height difference absolute value.

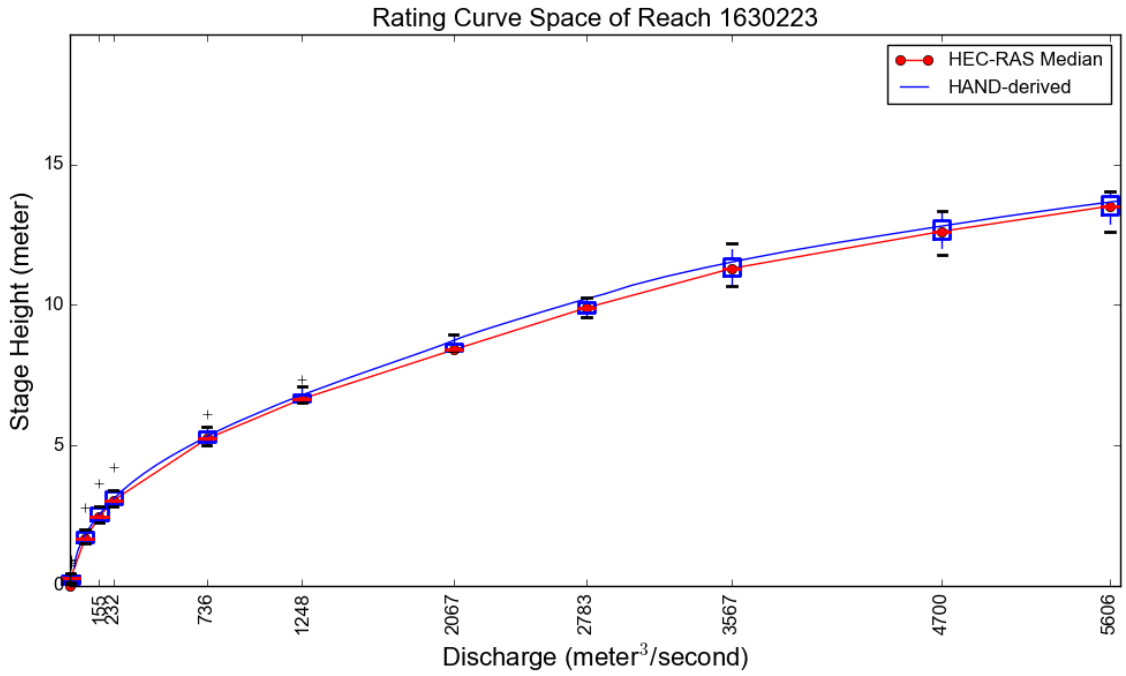

Figure 2.14: Comparison between HAND-derived and RAS-derived rating curves on reach 1630223 (n=0.045).

2.4.5 Comparison of Rating Curve and USGS Gage Observations

To better estimate the performance of HAND-derived synthetic rating curves and the effect of Manning's n calibration on the performance we compared the HAND-derived synthetic rating curves with those at USGS stream gages. The Tar River watershed in North Carolina was selected as the test bed (Figure 2.15). In this watershed, local hydraulic models have been integrated into a sophisticated flood risk information system. Within the domain covered by local models, observed rating curves are collected from nine USGS stream gages. The metric we use to compare the performance of rating curves obtained from multiple approaches is the difference in water depth converted from the 100-year flood discharge. Two types of information collected from local hydraulic

models are adopted when we conduct this comparison at each stream gage: the first one is the 100-year flow estimated from flood frequency analyses conducted by local model providers; the second one is the Manning's n range for channel and overbank zone from FEMA flood insurance study reports organized by county. After we obtained the 100-year discharge at each gage station from the local HEC-RAS model, we first converted it into the corresponding water depth using the gage measured rating curves, then performed another conversion with the HAND-derived rating curve computed with the default Manning's n value 0.05. Finally, we tuned the Manning's n value within the given n range to generate different rating curves and identified the optimal Manning's n, which led to a depth closest to USGS gage measurements.

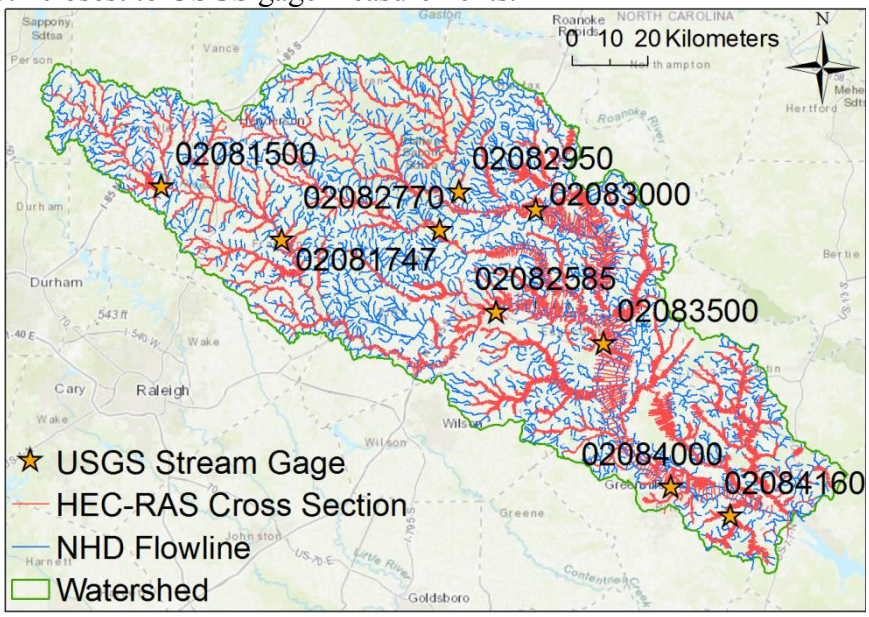

Figure 2.15: USGS stream gages with available measured rating curves in the Tar River watershed.

Table 2.2: Comparison of centerline water depths corresponding to the 100-year flood discharge converted through the USGS observed rating curve and the HAND-derived rating curve with default Manning's n (0.05) and optimal Manning's n. ($n_{channel}$: channel zone Manning's n range, $n_{floodplain}$: overbank zone Manning's n range, $Q_{100\text{-}year}$: 100-year flood discharge at given site, H_{usgs}: 100-year flood centerline water depth converted using USGS measured rating curve, $H_{hand\text{-}0.05}$: 100-year flood centerline water depth converted using HAND-derived synthetic rating curve with default Manning's n, $H_{hand\text{-}best}$: 100-year flood centerline water depth converted using HAND-derived synthetic rating curve with optimal Manning's n, n_{best}: optimal Manning's n value that produces the synthetic rating curve closest to USGS gage measurement)

USGS Site ID	$n_{channel}$	$n_{floodplain}$	$Q_{100\text{-}year}$ (m^3/s)	H_{usgs} (m)	$H_{hand\text{-}0.05}$ (m)	$H_{hand\text{-}best}$ (m)	n_{best}
02081500	0.03 - 0.058	0.1 - 0.17	543	6.79	6.15	6.56	0.058
02081747	0.03 - 0.042	0.08 - 0.15	715	7.07	8.82	7.04	0.031
02082585	0.025 - 0.05	0.05 - 0.16	784	8.52	7.28	8.52	0.096
02083500	0.025 - 0.05	0.05 - 0.16	1334	11.41	6.75	11.39	0.123
02084000	0.045 - 0.08	0.06 - 1	1504	7.91	8.4	7.95	0.045
02082770	0.042 - 0.06	0.05 - 0.15	511	5.54	3.31	5.31	0.15
02082950	0.044 - 0.065	0.05 - 0.16	394	7.28	6.23	7.27	0.077
02083000	0.04 - 0.08	0.035 - 0.2	688	5.65	4.28	5.65	0.103
02084160	0.045 - 0.055	0.1 - 0.165	152	2.19	1.41	2.19	0.104

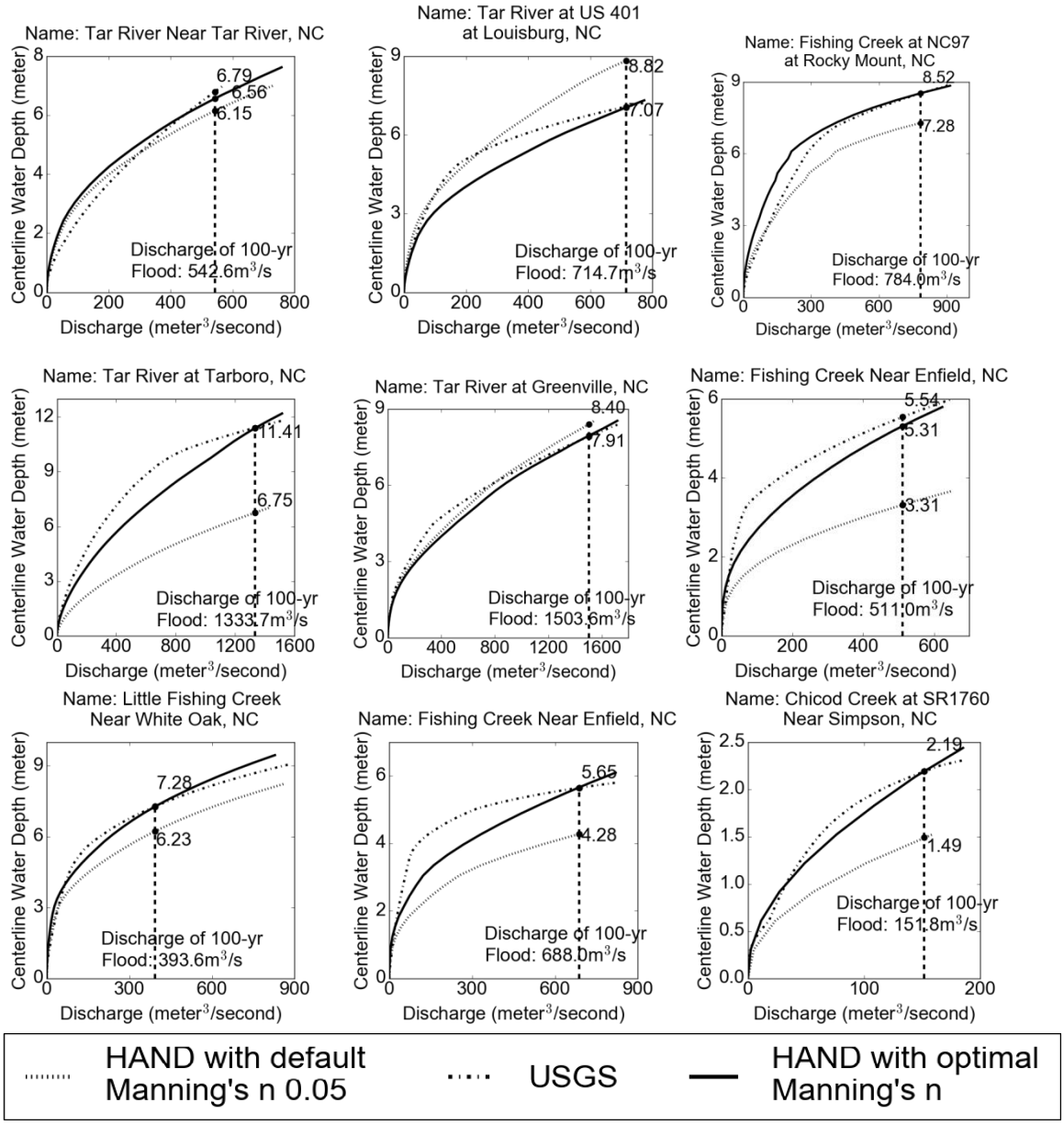

Figure 2.16: Comparison of measured rating curves and HAND-derived synthetic rating curves at USGS stream gages in the Tar River watershed.

The results (Table 2.1, Figure 2.16) show that compared to the observed discharge-stage relationships, although synthetic rating curves derived from the HAND raster with a constant Manning's n assigned globally could not reach a significantly high

accuracy everywhere, tuning Manning's n within a reasonable range can achieve near-real water depth prediction if more information about the channel roughness condition is available.

2.4.6 Inundation Extent Validation versus FEMA 100-year Floodplain

Although the estimation of HAND inundation mapping products is not the main focus of this study, we compare the HAND-derived inundation maps with FEMA 100-year floodplains to generally demonstrate the effectiveness of our HAND approach when it is applied to inundation mapping practice. The comparison is conducted within the same nine NHD catchments at the Tar River watershed where the stream gages are located. We generate the inundation extent corresponding to the 100-year flood depth obtained from previous analyses. To test how the accuracy of water depth prediction affects the accuracy of inundation mapping extent, we adopt different water depths computed from the observed rating curve and the synthetic rating curve with an uncalibrated Manning's n value (0.05).

Table 2.3: Comparison of FEMA 100-year floodplain and HAND-derived inundation extent in Tar River NHD catchments where USGS streamgages are located. ($Area_{FEMA}$: area of FEMA floodplain, $Area_{USGS}$: area of HAND-derived inundation extent corresponding to the centerline depth predicted from USGS rating curve, $Area_{Initial}$: area of HAND-derived inundation extent corresponding to the centerline depth predicted from synthetic rating curve with Manning's n of 0.05, F_{USGS} & C_{USGS}: F Index and C Index computed using $Area_{FEMA}$ and $Area_{USGS}$, $F_{Initial}$ & $C_{Initial}$: F Index and C Index computed using $Area_{FEMA}$ and $Area_{Initial}$)

USGS Site ID	$Area_{FEMA}$ (km^2)	$Area_{USGS}$ (km^2)	$Area_{Initial}$ (km^2)	F_{USGS}	C_{USGS}	$F_{Initial}$	$C_{Initial}$
02081500	0.16	0.15	0.14	0.90	0.99	0.93	0.98
02081747	0.19	0.21	0.34	0.82	0.99	0.54	1.00
02082585	1.63	1.78	1.40	0.86	0.99	0.84	0.88
02082770	1.88	2.26	1.64	0.80	1.00	0.91	0.92
02082950	1.39	1.64	1.33	0.79	1.00	0.91	0.97
02083000	1.24	1.27	1.18	0.94	1.00	0.97	0.98
02083500	0.35	0.51	0.46	0.65	1.00	0.66	0.95
02084000	0.49	0.53	0.56	0.87	1.00	0.82	1.00
02084160	0.37	0.27	0.22	0.81	0.82	0.67	0.67

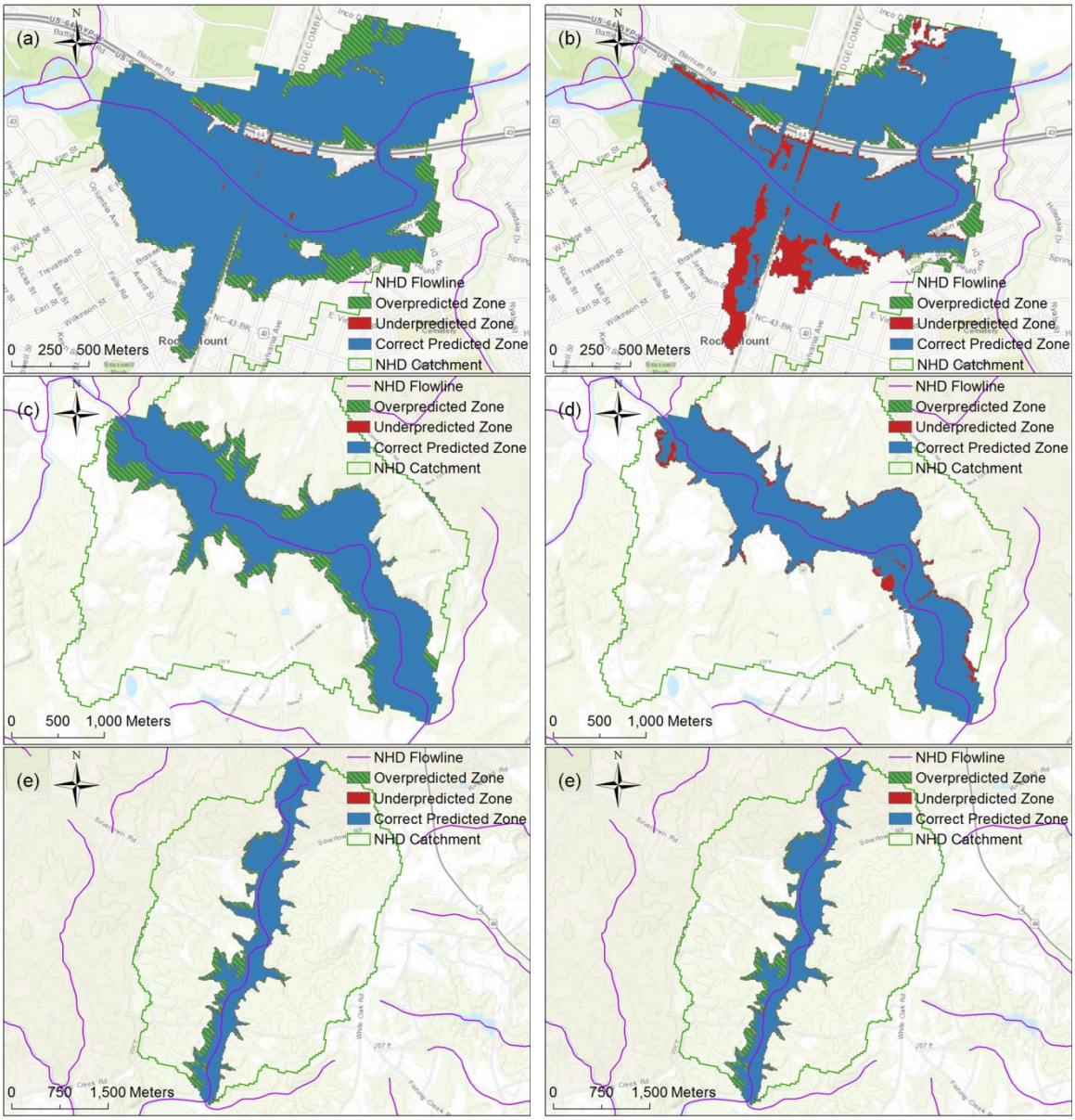

Figure 2.17: Comparison of FEMA 100-year floodplain and HAND-derived inundation extent in Tar River NHD catchments where USGS stream gages are located. (Catchments with top three inundated area size are selected to present, (a)(b): USGS gage 02082585, (c)(d):USGS gage 02082770, (e)(f):USGS gage 02082950. (a)(c)(e) show HAND the inundation extent generated with the water depth predicted from USGS observed rating curves, (b)(d)(f) show the HAND inundation extent generated with the water depth predicted from HAND-derived synthetic rating curves with Manning's n of 0.05)

The results in Table 2.3 and Figure 2.17 show that in general, the inundation extent produced with the HAND approach is able to capture the majority of FEMA floodplain, even without a calibration of the Manning's n coefficient. Due to the absence of the bathymetric portion, the water depth computed from the terrain data with our HAND approach is often higher than the actual water depth. Therefore, a more accurate prediction of flood depth does not necessarily lead to a better estimation of the inundation extent with our approach. Instead, a slight over-prediction of inundation extent is detected at many sites. We also observed that the HAND inundation mapping method performs better in the hilly, rural catchments where the flood routing process is controlled by the topographic setting, compared to the flat, urbanized catchments where artificial structures significantly affect the hydrodynamic process. To capture the mass and momentum exchange within the affected flood zones, we need more sophisticated physical methods.

2.5 DISCUSSION

This paper has presented a new method for the determination of reach average hydraulic properties from a digital elevation model based on the Height Above Nearest Drainage (HAND) approach. The comparison to HEC-RAS cross sections showed that the method can produce reasonable results. This holds promise, as the method can be fully automated and is based on readily available national data and can thus be applied rapidly across the whole country reducing the need for detailed cross section-based flood inundation mapping. We believe that this method has the potential to support national scale modeling, such as the National Water Model. In this section, we discuss some limitations of our approach and our preliminary exploration work to address them. Our approach assumes that the input DEM represents the shape of the river channel, which is

a limitation on data fidelity. We found that, with the HEC-RAS comparisons, that adjustment of the base elevation may be needed in certain cases. We expect that as DEMs are improved, especially if and when they include channel bed bathymetry obtained from water penetrating lidar or sonic depth measurement, that the need for such adjustments may be reduced, and that the results from HAND may improve. We also acknowledge the preliminary and approximate nature of this method, particularly in areas where artificial hydraulic structures or momentum interaction between channel and floodplain controls the propagation of flood waves. Therefore, we suggest it be used primarily as a screening tool to identify locations where more detailed study is warranted.

In particular, we are considering a number of DEM and hydrography issues when applying HAND. We illustrated how the pit filling process needed to ensure a hydrologically conditioned DEM where each grid cell drains to the edge of the domain, can result in inflated DEM values along the streams. Some of these values occur behind barriers due to artefacts in the DEM production process and due to the DEM representing the elevation of road/railway crossings and not the elevation of the bridge or drain beneath these crossings through which water passes. We are investigating ways to use high resolution hydrography information (e.g. NHD HR, nominally at 1:24,000 scale (ftp://rockyftp.cr.usgs.gov/vdelivery/Datasets/Staged/Hydrography/NHD/National/HighResolution/) that represents flow lines with greater fidelity than NHDPlus) to adjust the DEM so that elevation is non increasing along hydrographically mapped flow lines. This provides the capability to punch through barriers where the hydrography indicates that flow crosses the barrier, partially alleviating this problem. We are also investigating using geodesic approaches to map flow paths (e.g., Passalacqua et al., 2010a; Sangireddy

et al., 2016) to overcome barriers more automatically using geomorphologically based filtering approaches without the requirement for hydrographic mapping.

We also showed how hydrography, notably the NHDplus medium resolution hydrography used in the National Water Model can be misaligned with valley paths in a DEM. The HAND approach follows flow directions downslope and requires streams aligned with the DEM. Using the NHDPlus flowlines directly would have resulted in spurious results for the area (as illustrated in Figures 3 and 4), and this motivated our use of the DEM stream delineation approach starting from NHDPlus channel heads. However, even with this approach, a one to one mapping between stream segments in the DEM delineated network and NHDPlus is not guaranteed and areas draining to DEM stream segments may not align exactly with NHDPlus catchments, resulting in some errors around the edges when clipping the HAND raster based on the NHDPlus catchment boundaries. There is thus a need, in national datasets, for better alignment and reconciliation of elevation and hydrography representations of streams. An example of ongoing effort is the NHDPlusHR (Viger et al., 2016).

Channel properties are currently organized by reach and a uniform water depth is assigned to a reach during the inundation mapping process. Sometimes reaches are quite long and assuming a uniform depth is unreasonable. It is possible to split reaches into shorter segments, but we leave to future work the exploration of the best length to use. The optimal distance between cross sections in 1D hydraulic modelling has been shown to be proportional to the bankfull width (Samuels, 1990; Castellarin, 2009); adding extra cross sections within the optimal spacing decreases the accuracy of the simulation due to rounding errors (Castellarin, 2009). If the segments of a reach can be specified and exported during the HAND computational process, these new profiles across the stream

cells have a potential to replace the traditional cross sections used in 1-D hydraulic models. Organizing hydraulic properties in a segment unit smaller than a reach also has the potential to help resolve the instability problem in large-scale hydraulic models when a sudden channel shape change happens at a river confluence. The validation of HAND channel geometry properties through the comparison with HEC-RAS-derived reach-average channel should be extended to a larger sample size. To ensure comprehensiveness, this sample should cover reaches of different stream orders and with different physiographic settings.

A generic way to evaluate channel and floodplain roughness values from land cover information or any other instructive variables would be helpful to improve the accuracy of the HAND rating curves. If the bankfull depth information of all the rivers in a large-scale network could be derived from the geometry data, instead of applying a single Manning's equation to all water levels in a reach, a compound uniform flow equation could be implemented to better describe the hydraulics when the water level reaches the floodplain with a different roughness value. Also, the hydraulic conductance underestimation problem of empirical hydraulic equations at high flow condition needs to be considered. If a large-scale hydrodynamic model such as SPRNT (Liu and Hodges, 2014) is used, rating curves can be generated from the dynamic simulation with HAND river geometry information fed to the model. Note that, if a different method is used to determine the water depth in the channel, such as by direct observation or by using a solution of the full Saint Venant equations (SPRNT), then the hydraulic geometry data and the HAND raster can be used to produce an inundation map without the need for use of a synthetic rating curve.

2.6 CONCLUSION

In this paper, a workflow for computing river geometry and estimating channel reach rating curves based on DEM derived Height Above Nearest Drainage (HAND) was presented. This was illustrated for NHDPlus reaches of the Blanco River watershed using the 1/3 arc sec USGS 3DEP Elevation dataset DEM. The workflow requires as input a DEM, the channel heads (or a stream network from which they can be extracted), and a Manning's n value. The hydraulic geometry properties and rating curve derived from the HAND approach were shown to be generally consistent with similar information derived from more traditional cross sections and HEC-RAS hydraulic modeling, which require a much more labor and data intensive process. Issues related to DEM fidelity and the need for adjustments in the base elevation were identified and discussed. Calibration to determine an optimal Manning's n roughness parameter produced a value very close to the value used in HEC-RAS modeling, further validating the approach. Overall, this approach was shown to hold promise for supporting quantitative hydraulic modeling at continental scale using readily available national datasets. A companion paper (Liu et al., 2018) applies this approach to nationally available data using high performance computing.

Our method has attracted interest from the community, industry, and government agencies. Starting with the 2016 National Flood Interoperability Experiment, researchers have been working extensively to test the performance of our inundation approach against other methods (Afshari et al., 2018; Zhang et al., 2018). Esri has integrated different components of our workflow into the latest ArcHydro toolbox. The NOAA National Water Center implemented the HAND workflow during Hurricane Harvey to produce real-time flood maps for over 60,000 kilometers of streams and river in

Southeast Texas. In 2018, NOAA proposed to implement the HAND inundation mapping operationally for the West Gulf forecast region. Although limitations exist in our method due to the terrain-only consideration and the one-dimensional steady flow assumption, we think it is a valid approach for approximate inundation mapping especially in those areas where detailed hydraulic studies are not available. We encourage readers to test our method under different flow and terrain scenarios to achieve a comprehensive understanding of its performance and limitations.

Chapter 3: GeoFlood: large scale flood inundation mapping based on high resolution terrain analysis[2]

3.1 ABSTRACT

Recent fast-occurring, extreme-magnitude, wide-spreading deluges caused by hurricanes and associated intense precipitation events call for responsive and real-time inundation mapping solutions of broad coverage and high resolution. Several approaches to large-scale approximate inundation mapping based on hydrodynamic simulation and conceptual models have been proposed and applied to low-resolution terrain inputs. High-resolution topographic data derived from lidar technology reveals unprecedented topographic details and is increasingly available toward national coverage, providing extremely valuable information for improving inundation mapping accuracy. The enrichment of terrain details from these datasets, however, also brings challenges to the application of many classic approaches designed for lower-resolution data. We argue that more advanced methods need to be developed to better use lidar-derived terrain data for inundation mapping.

We propose a complete workflow, GeoFlood, for approximate inundation mapping using high-resolution terrain inputs with low physical complexity and low computational cost, thus responding to the needs of emergency responders. First, GeoNet, a method for automatic channel network extraction from high-resolution topographic data, is modified to produce a low-density, high-fidelity river network. Then, a Height Above Nearest Drainage (HAND) raster of the same resolution of the input terrain data is computed to qualify the elevation difference between each land surface cell and the stream bed cell to which it drains, using the network extracted from high-resolution

[2]The text contained within this chapter has been submitted in Water Resources Research (WRR).

terrain data. This HAND raster is then used to compute reach-average channel hydraulic parameters and synthetic stage-discharge rating curves. Inundation maps are generated from the HAND raster by obtaining a water depth for a given flood discharge from the synthetic rating curve. We perform comprehensive evaluation of our approach by applying it in the Onion Creek Watershed in Central Texas. The inundation extent results are compared with FEMA 100-year floodplains obtained with detailed local hydraulic studies. We show that the inundation extent produced by GeoFlood overlaps 60%~90% percent of the FEMA floodplain coverage.

3.2 INTRODUCTION

Flooding is the most threatening natural disaster worldwide considering the fatalities and property damage it causes. It makes up to 40% of all natural disasters worldwide and causes about half of all natural hazard fatalities (Noji, 1991; Ohl et al., 2001). Recent flood disasters resulting from hurricanes of the unusually active 2017 Atlantic hurricane season have raised concerns for accurate and responsive inundation forecast due to the rapid spread and astonishing destructive power of these events. In this work, we propose a novel approach, called GeoFlood, for approximate inundation mapping on high-resolution topographic data. Our approach couples the effective Height Above Nearest Drainage (HAND) (Nobre et al., 2011; Nobre et al, 2016) method and a channel extraction method designed for high-resolution lidar-derived terrain data (Passalacqua et al., 2010a).

Inundation mapping captures the spatial extent of flooding and is one of the critical products used by first responders during flood emergency response (Apel et al., 2009). Flood disasters caused by hurricanes Harvey, Irma, and Maria emphasized the

need for rapid flood inundation mapping over very large areas. Existing approaches to inundation mapping can be classified in three categories (Teng et al., 2017): empirical methods, hydrodynamic models, and simplified conceptual models. Empirical methods are based on observations (Stephens et al., 2014; Schumann et al., 2009) and can only provide guidance for real-time monitoring and post-event evaluation. Hydrodynamic models create inundation maps by solving one-dimensional Saint-Venant equations or two-dimensional shallow water equations. Although these models can be parallelized to leverage a large amount of computing power and create continental-scale inundation maps at 30-meter resolution or coarser (Wing et al., 2017; Schumann et al., 2013; Sampson et al., 2015; Dottori et al., 2016), running such models at higher resolutions or during real-time flood events remains computationally impractical. On the other hand, simplified GIS-based conceptual inundation mapping strategies have been developed (Zheng et al., in review) and implemented at the continental-scale at 10-meter resolution (Liu et al., in review). Efficient implementation on parallel computing platforms has accelerated classical hydrological terrain analyses, such as pit filling, flow direction and flow accumulation area computation, from a monthly or daily task to an hourly task when performed at continental-scale (Liu et al., in review). Therefore, compared to the more physically rigorous but more computationally intensive hydrodynamic models, conceptual approaches are better prepared for emergency response by ingesting detailed inputs quickly because of their simplicity.

Previous research (Thomas et al., 2016) suggested that inundation details derived from terrain information at fine spatial resolutions may be unnecessary and cause overconfidence in the mapping outputs. However, the opportunities provided by high-resolution topographic data derived from advanced remote sensing technology such as

light detection and ranging (lidar) cannot be underestimated (Casas et al., 2006; Hilldale and Raff, 2008; Bates, 2012; Tarolli, 2014; Passalacqua et al., 2015). This type of data is especially critical for inundation mapping in areas where artificial structures such as buildings and roads dominate flow patterns and may be undetectable in coarse terrain data sets (when the grid cell is larger than the feature of interest). On the other hand, high-resolution terrain data introduces both highly detailed information and data uncertainties (e.g., errors) that may not exist from terrain data of coarse resolutions and may significantly influence inundation mapping model assumptions, applicability, and results. For instance, artificial structures may need to be identified and processed to create the flow continuum (i.e., a burn-in process for appropriate flow direction detection) if a model assumes a flow continuum on a study area. Also, the discrepancies between the flow network derived from high-resolution Digital Elevation Model (DEM) and that in published flow network dataset of lower resolution (e.g., NHDPlus) become more significant. Errors in lidar-derived DEM such as voids and vertical errors may also need explicit handling for a study area of high horizontal resolution. While it has been suggested that higher spatial resolution improves the local prediction of water depth rather than the extent of inundation (Leskens et al., 2014), systematic quantitative comparisons between inundation maps created with different resolution terrain inputs have not been performed thus far over areas of different characteristics.

The main goal of this paper is to propose a method, called GeoFlood, that is able to create high-resolution inundation maps at low computational cost. Our method uses a simplified conceptual inundation mapping approach (Zheng et al., in review) and lidar-derived high-resolution topographic data and it is based on the Height Above Nearest Drainage (HAND) method (Nobre et al., 2011; Nobre et al, 2016). The HAND method

has been already applied and tested at the continental scale using a 10-meter DEM over the continental U.S. (Liu et al., in review). One key output of this approach is a HAND raster that provides the elevation difference between each land surface cell and the stream bed cell to which it drains. In a recently proposed approach (Zheng et al., in review) this HAND raster is used to derive the channel geometric properties of each stream segment. A synthetic rating curve for each reach is then computed from these channel properties and then used to convert a flow time series into a corresponding water level time series (Zheng et al., in review). Inundation maps are then created for the water level at each time step from the HAND raster. In the approach of Zheng et al. (in review), a DEM-derived channel network is used as the local datum to evaluate the flood vulnerability at any given location. Therefore, the accuracy of the channel centerline may significantly affect the resulting inundation extent. Innovative approaches for automatic channel extraction from lidar data have been developed (e.g. Passalacqua et al., 2010a; Orlandini et al., 2011; Johansen et al.; Pelletier 2013; Sangireddy et al., 2016), but these approaches have not been coupled with inundation mapping techniques. Here we further develop the approach of Zheng et al. (in review) for its application to high resolution terrain data. To address formidable challenges of river network identification associated with high-resolution terrain data, we extract channel networks for HAND computation and inundation mapping by enhancing GeoNet (Passalacqua et al., 2010a), a method for the automatic extraction of channel networks from lidar-derived DEMs. The GeoNet approach combines nonlinear multiscale filtering and geodesic least-cost-path search to handle data precision and uncertainty issues in high-resolution DEM. The coupling of GeoNet and HAND creates GeoFlood, a novel approach for high resolution inundation mapping.

The paper is organized as follows: after introducing the study area (the Onion Creek watershed, Central Texas) and data preparation (Section 3.3), we present how the GeoNet approach and the HAND approach are coupled (Section 3.4) to extract an improved river network and create a complete inundation mapping workflow. To comprehensively understand the performance of our coupled workflow, we create inundation maps for several streams in our test watershed, which flow through different landscape settings, under the 100-year flood scenario defined by the FEMA flood insurance study. HAND-derived synthetic rating curves and inundation maps are compared with field observations and simulated outputs (Section 3.5). We discuss possible reasons for the differences shown in the results (Section 3.6) and conclude that although strict momentum conservation is absent, our approach is able to capture the general inundation patterns, and shows significant potential in guiding real-time flood disaster preparedness and response (Section 3.7).

3.3 STUDY AREA

Our study area (Figure 3.1) is the Onion Creek watershed, a tributary watershed of 892 km^2 to the Colorado River. Morphologically, this watershed represents a typical rolling terrain transition from the eastern edge of the Edwards Plateau to the western edge of the Gulf Coastal Plain. High-resolution bare-earth DEM (3 m resolution) was generated by combining point clouds acquired in aerial collections during the leaf-off season of 2007, 2008 and 2012 with different coverage. The complete DEM was provided by the Texas Natural Resources Information System (TNRIS). The elevation of this DEM ranges from 113 to 510 m a.s.l. with an average of 289 m. The slope varies from 0° to 77.3° with an average of 4°.

The area lies on the border between a sub-tropical humid climate and a sub-tropical subhumid climate with a mean annual rainfall of about 850 mm. Precipitation occurs mainly in late spring and early autumn. Flash flooding caused by short-term high-intense storms during these periods brings serious threats to life and property in this watershed. On October 31 in 2013, a flood event resulted in 4 fatalities, 825 impacted homes, 40 closed roads, and more than $10 million public infrastructure damage. Flooding reached the highest recorded depth of 12.2 meters since 1921 with an estimated discharge of 3820 m^3/s. Two years later, another storm was recorded over the same area on October 30, 2015, when 35 cm of precipitation fell on the Onion Creek watershed in six hours. Water level measurements at USGS gage 08159000 reached 12 meters with a peak discharge of 3454 m^3/s. The 2015 flooding led to 3 fatalities and 400 damaged structures mainly located in the same area as the 2013 flood. Frequent severe flooding disasters call for more comprehensive understanding of the flooding process in this watershed, providing practical reasons for choosing it as a test site.

Calibrated hydraulic models and inundation maps are available for the main stem river and major tributaries in the Onion Creek watershed. These models were created by local consulting companies and approved by the City of Austin and FEMA for flood mitigation purposes. However, these inundation maps only simulate the scenarios corresponding to several given return-period flood events such as the 100-yr flood (Figure 3.1b) and the 25-yr flood estimated with flood frequency analysis. Therefore, these maps cannot capture the complex dynamic characteristics of an extreme flood event, which may exceed the magnitude of the simulated scenarios. This limitation was confirmed by the impact estimation process after the 2015 flood, which concluded that extensive flooding occurred beyond the mapped floodplains (Vigil et al., 2016).

To evaluate the quality of different components produced by GeoFlood, we selected multiple standardized datasets available in the public domain as references: the National Hydrography Dataset Plus Medium Resolution (NHDPlus MR) to test the extracted channel network, measured rating curves at six USGS stream gages located on the test creeks to test the synthetic rating curves, and the FEMA 100-year floodplains on five streams in the Onion Creek watershed (Onion Creek, Slaughter Creek, Williamson Creek, Marble Creek and Boggy Creek) where a calibrated engineering hydraulic model is available.

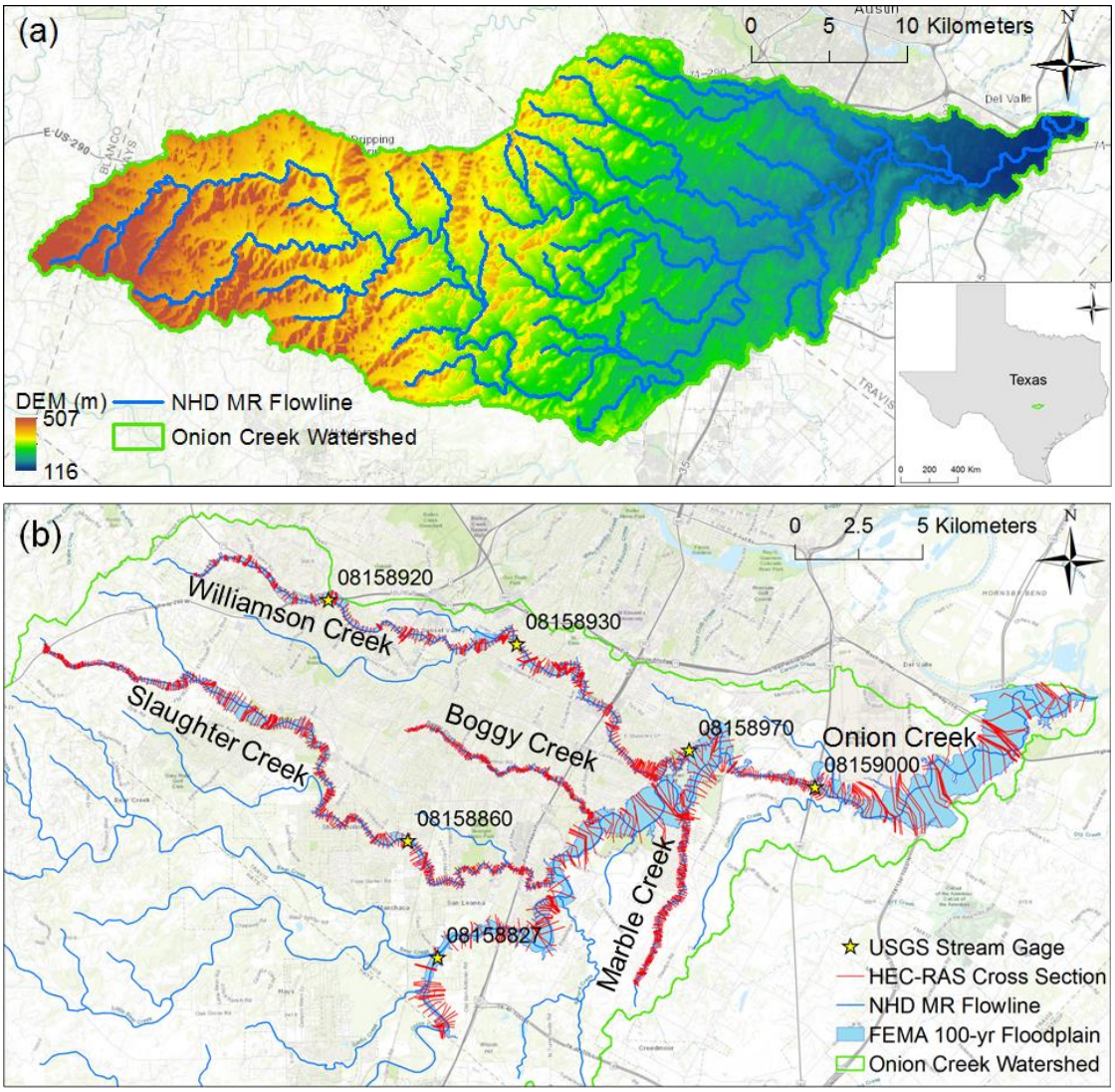

Figure 3.1: The Onion Creek Watershed study area: (a) Location map of the study area and NHDPlus MR network with 3-meter DEM as background. The watershed outlet is located at 30°12′18″N, 97°35′24″W. (b) Lower portion of the watershed and cross sections on five streams from the local HEC-RAS model and FEMA 100-yr floodplain.

3.4 METHODS

3.4.1 Automatic Channel Network Extraction

As first step of our GeoFlood workflow, we use GeoNet (Passalacqua et al., 2010a; Sangireddy et al., 2016) to automatically extract the river network centerlines from lidar-derived terrain datasets. The first step performed in GeoNet is a nonlinear filtering operation (Perona and Malik, 1990) to smooth out terrain variability at scales smaller than the scale of interest, which is considered as noise for the network extraction task. Following the filtering operation, we compute the geometric curvature κ on the filtered DEM, defined as the gradient of the elevation gradient normalized by its magnitude:

$$\kappa = \nabla \cdot \left(\frac{\nabla h}{|\nabla h|} \right) \tag{3.1}$$

where h indicates elevation.

Convergent features of the landscape with positive curvature above a threshold are identified as likely channelized zones and referred to as a skeleton. The curvature threshold is automatically detected from a quantile-quantile plot, which compares the statistical distribution of curvature to a normal distribution. The transition from hillslope to valley is identified at the deviation of the curvature distribution from a straight line (normal distribution) in the positive tail (Lashermes et al., 2007). An additional threshold, called the skeleton thinning parameter, is applied to further thin the set of likely channelized pixels identified with the curvature analysis. This thinning operation is able to exclude small convergent areas that are not part of the channel network (Passalacqua et al., 2010a).

Local artificial structures (e.g., roads, bridges, and dams) present in the terrain may disrupt the skeleton. This issue is addressed by extracting channel centerlines with a

geodesic minimization approach, which ensures the continuity of the extracted network. This approach uses a geodesic cost function (Passalacqua et al., 2015) defined as:

$$\psi = \frac{1}{\alpha A + \beta \kappa + \gamma S} \tag{3.2}$$

where α, β, and γ are constants used for dimensionality and to normalize the difference in order of magnitude of the accumulation (A), curvature (κ) and skeleton (S) terms. The river network comprises the least-cost-paths connecting the channel heads to the watershed outlet.

The classic GeoNet workflow has two limitations when applied to inundation mapping. First, GeoNet automatically identifies channel heads as the upstream end points of the skeleton branches. As GeoNet extracts the network based on terrain convergence, those extracted paths may or may not carry water at all times, resulting in a network that may be denser than the perennial one. Furthermore, slope-based flow directions computed from the DEM are affected by the presence of artificial structures, because the terrain signal reports the elevation at the top of the structure (e.g., a bridge) unless the structure is manually removed (e.g., cells covering major roads in the 10m National Elevation Dataset (NED)). The computed flow accumulation area may thus have errors, resulting in inaccuracies of the extracted network. The density of the extracted network is reduced by using channel heads of perennial rivers defined in the NHDPlus MR. The stream network of the NHDPlus MR with the continental U.S. coverage is derived from the 30 meter resolution NED using a classic slope-based approach with extensive manual corrections. Because the accuracy of the NHDPlus MR is limited by its input spatial resolution and the extraction method, it is not suitable for direct use in high-resolution hydrological terrain analyses, but it provides helpful information on the approximate location of the river centerline. We propose to use the NHDPlus MR river network to

create a prior sample space of likely channelized pixels within which accurate flowpaths can be extracted, removing the inaccuracies introduced by topographic barriers and the coarser data resolution of the NHDPlus MR. We use the skeleton identified by GeoNet based on terrain curvature and flow accumulation as the likelihood function to update prior knowledge. We then develop an innovative Bayesian approach to obtain the posterior estimation of the river network.

The detailed steps of this Bayesian extraction approach are as follows (Figure 3.2):

(1) A buffer zone is created around the NHDPlus MR river network. The width of the buffer zone is set to be wider than the maximum channel width at a given site.

(2) The buffer zone is converted into a binary raster in which the value of 1 is assigned to all the cells that compose the flowlines (stream cells) and the value of 0 at all other cells.

(3) For each cell within the buffer zone we identify its nearest stream cell based on Euclidean distance.

(4) We compute the relative height between each cell and its nearest stream cell on NHDPlus MR flowline and keep all the cells with a non-positive relative height in order to create the prior sample space of likely channelized pixels.

(5) A probability of 0.99 is assigned to all the cells within the prior sample space and 0.01 otherwise. The assumption behind this operation is that if the NHDPlus MR flow vertex is located on the thalweg, it will be retained, as the elevation of any other point along the transect profile will be relatively higher than its elevation. Otherwise, if the vertex is located outside the thalweg or outside the channel zone, only the cells that are relatively lower than its elevation are considered part of the centerline.

(6) Flow accumulation and curvature information are used to assign different likelihood probabilities to the cells in the prior sample space: if a pixel is part of the GeoNet skeleton (i.e., it has a large upstream contributing area and a positive curvature), it is very likely to be a theoretical centerline pixel. Therefore, its likelihood probability is 0.99. The probability of other pixels within the prior sample space is assigned equal to 0.01. The likelihood probability assignment forces the final network product to pass through as many skeleton pixels as possible.

(7) We define our cost function as the reciprocal of the posterior probability. The river network is then extracted as a set of least-cost paths connecting the channel heads to their corresponding watershed outlet.

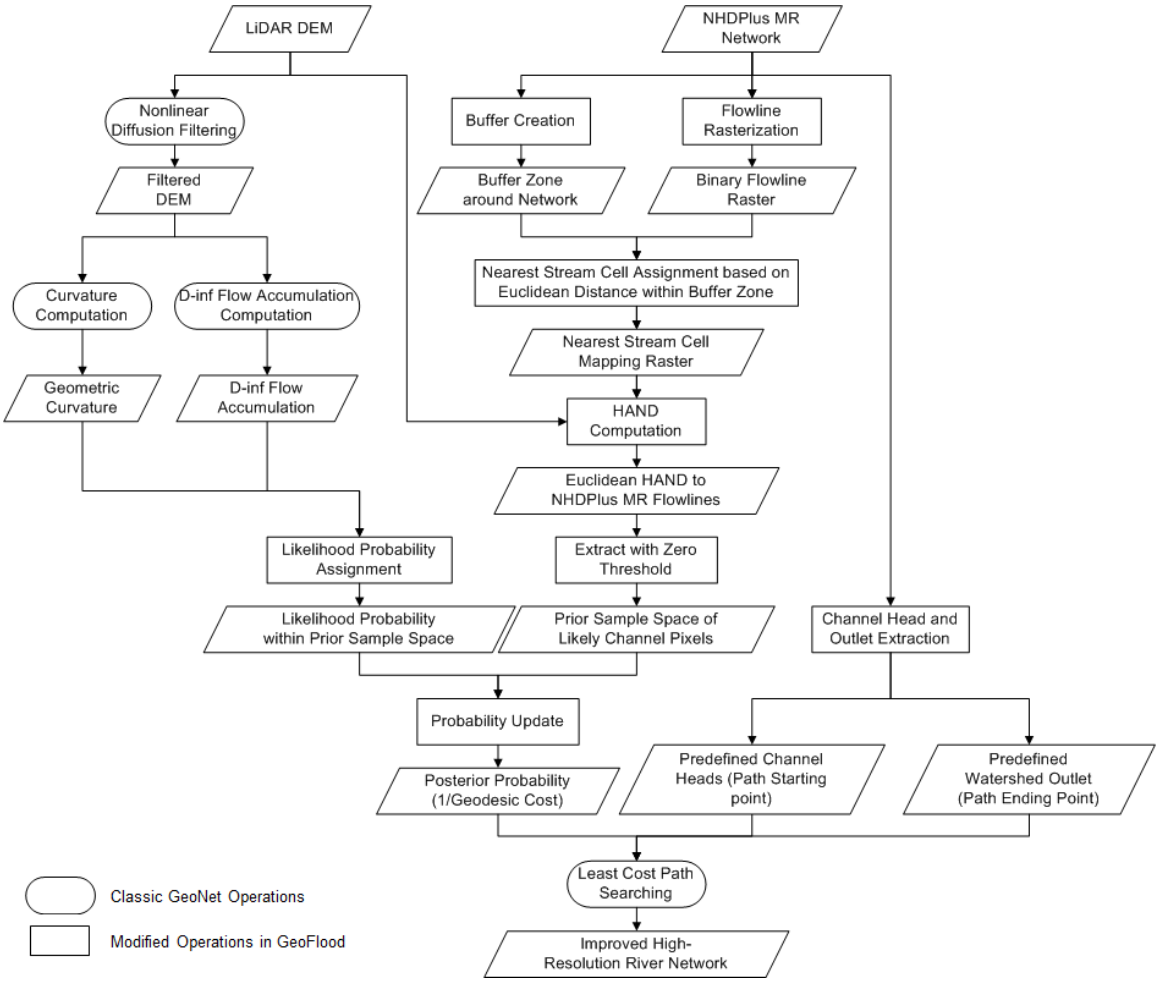

Figure 3.2: The channel network extraction workflow in GeoFlood.

3.4.2 Channel Hydraulic Property and Rating Curve Estimation

Once the river network is extracted, a HAND raster is computed from the original DEM as the relative height of each cell with respect to the nearest stream cell it drains to, determined using the D-infinity approach (Tarboton, 1997). The HAND value of each pixel is calculated by subtracting the elevation of its nearest stream cell from the cell's original elevation. At local depressions with elevation lower than the channel centerline datum, the elevation is filled during a pit-remove process to ensure connectivity to the

stream pixels. However, the HAND value of these local depressions is computed from the raw DEM, thus may have a negative value, even though the flow directions are derived from a pit-filled DEM.

An innovative approach for estimating channel hydraulic property and rating curve from the HAND raster has been recently proposed in (Zheng et al., in review) and followed to derive channel hydraulic properties and estimate rating curves. We summarize the approach here for completeness. Given a centerline water depth h at a river segment, the HAND raster is used to produce a water depth grid of the inundated area *F(h)* within the local catchment draining to that segment. The water depth d at any location *i* is computed as:

$$d_i = \begin{cases} h - hand_i, if\ hand_i \le h\ (flooded,\ i \in F(h)) \\ 0, if\ hand_i > h\ (not\ flooded,\ i \notin F(h)) \end{cases} \tag{3.3}$$

Flood volume *V*, inundated surface area *SA*, and inundated bed area *BA* corresponding to the given depth are then derived from that depth grid:

$$\begin{aligned} V &= \sum_{i \in F(h)} d_i \cdot da_i \\ SA &= \sum_{i \in F(h)} da_i \\ BA &= \sum_{i \in F(h)} s_i \cdot da_i \end{aligned} \tag{3.4}$$

where da_i is the cell area at location *i* and s_i is the planar slope computed with the D-inf algorithm at location *i*.

When the volume, surface area, and bed area are divided by the segment length *L*, the cross sectional area *A*, the channel top width *W*, and the wetted perimeter *P* can be estimated for any water depth *h*:

$$A = \frac{V}{L}$$

$$W = \frac{SA}{L} \tag{3.5}$$
$$P = \frac{BA}{L}$$

The channel hydraulic radius R is then derived as:

$$R = \frac{A}{P} \tag{3.6}$$

Under the assumption of one-dimensional steady flow, the Manning's equation is then applied using the derived hydraulic properties to obtain a synthetic rating curve that links discharge Q and centerline water depth h:

$$Q = \frac{AR^{\frac{2}{3}}S^{\frac{1}{2}}}{n} \tag{3.7}$$

where S is the channel bed slope and n is the surface roughness coefficient.

To establish the aforementioned hydraulic properties for a river network, the extracted river centerlines are divided into segments (reaches) and the channel hydraulic properties are estimated separately for each segment. It is worth noting that if the reach length is too short, local terrain heterogeneity may cause variability of bed slope and other variables; on the other hand, if the reach length is too long, the hydraulic properties may bulk together too many channel geometric details, reducing the accuracy of the estimated hydraulic geometry characteristics on that reach.

3.4.3 Inundation Mapping

As the last step of GeoFlood, a segment-based inundation mapping process is conducted using the HAND raster and the synthetic rating curves. During a flood event, a discharge time series is assigned to each segment in the network based on the results of hydrological simulation. From the discharge time series, we obtain the corresponding water depth time series using the synthetic rating curve. At each time step, the HAND value of any cell within the local catchment draining to the segment is compared to its

real-time water depth estimation. If the HAND value is smaller than the depth, that cell is treated as inundated and the water depth at that cell is computed as the difference between the depth and the HAND value.

To evaluate the performance of the HAND mapping results, two binary metrics, the fit index and the correct index, are calculated from the confusion matrix (Table 3.1):

Table 3.1: The Confusion Matrix

		Hydrodynamic Simulated Inundation Extent	
		Wet	Dry
HAND Inundation Extent	Wet	TW	FW
	Dry	FD	TD

The fit index (F) provides an overview of the method performance, and accounts for overprediction and underprediction at the same time:

$$F = \frac{TW}{TW + FD + FW} \tag{3.8}$$

The range of the F index varies from 0 (no overlap between two sets) to 1 (complete overlap).

The correct index (C) quantifies the percentage of the reference map inundation extent predicted:

$$\mathrm{C} = \frac{\mathrm{TW}}{\mathrm{TW} + \mathrm{FD}} \tag{3.9}$$

This metric only evaluates a model's tendency toward underestimation, and therefore, is less strict than the fit index. The range of the C index also varies from 0 (no coverage) to 1 (complete coverage of the reference extent).

3.5 RESULTS

To test the performance of GeoFlood, we implement it over the Onion Creek watershed. The NHDPlus MR flowlines extracted from a lower-resolution DEM are not

able to accurately match the actual valley location as detected in the high-resolution terrain dataset (see road in Figure 3.3a). Also, artificial structures, e.g., roads, are present in the topographic dataset at this site, challenging the application of classic gradient-based channel extraction approaches (Figure 3.3a). As explained above, a negative height zone (relative to the NHDPlus MR flowline pixels) is identified based on the Euclidean distance (Figure 3.3b). This zone confines the likely channelized pixels within a smaller but uninterrupted domain. Curvature and flow accumulation are then used to assign likelihood probabilities to these pixels (Figure 3.3c). The new network extracted as the least-cost path from a given channel head to the outlet is more accurate than the original NHDPlus network (Figure 3.3d).

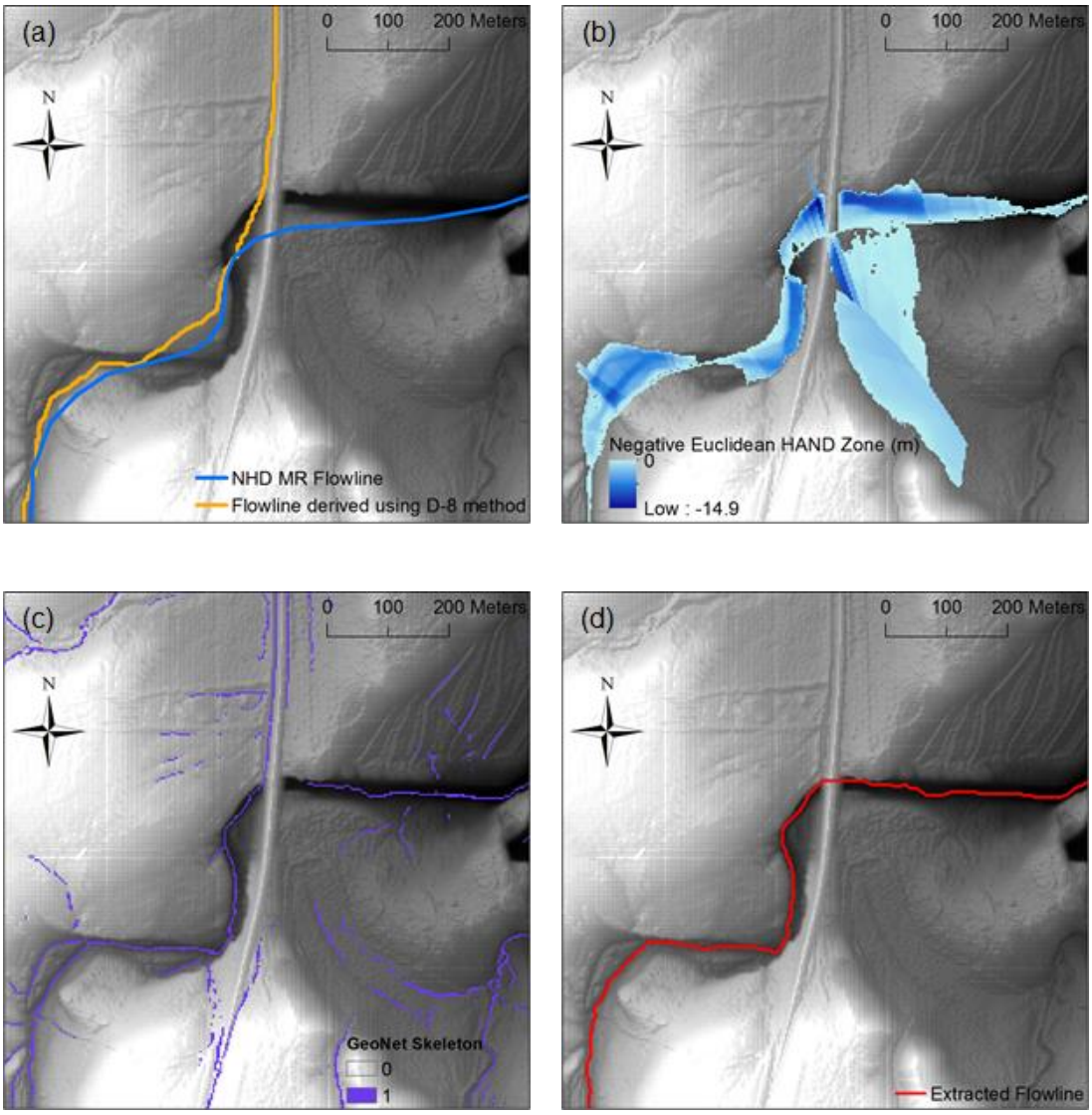

Figure 3.3: An example of the GeoFlood channel extraction method on a river crossing underneath a highway road: (a) Location of the original NHDPlus medium resolution flowline and the centerline extracted with the D-8 algorithm. (b) Negative HAND zone identified relative to the NHDPlus flowline based on Euclidean distance. (c) The skeleton of likely channelized pixels based on curvature and flow accumulation. (d) The geodesic least-cost path extracted as the final centerline product.

Once the stream network is extracted, the extracted centerline pixels are treated as the local datum used in the HAND calculation. A HAND raster is created from the raw 3-

meter DEM (Figure 3.4a). Since the streamline elevation change is normalized in HAND, the elevation range of the Onion Creek watershed has been reduced from 391 meters in the original DEM to 121 meters in the new HAND raster. These centerlines are divided into segments with an optimal length of 1.5 km, as recommended by previous studies (Johnson et al., 2017). The local drainage catchment is delineated for each segment and reach-average channel hydraulic parameters are derived for each river segment (Figure 3.4b) from the HAND subset within its local drainage catchment (Figure 3.5).

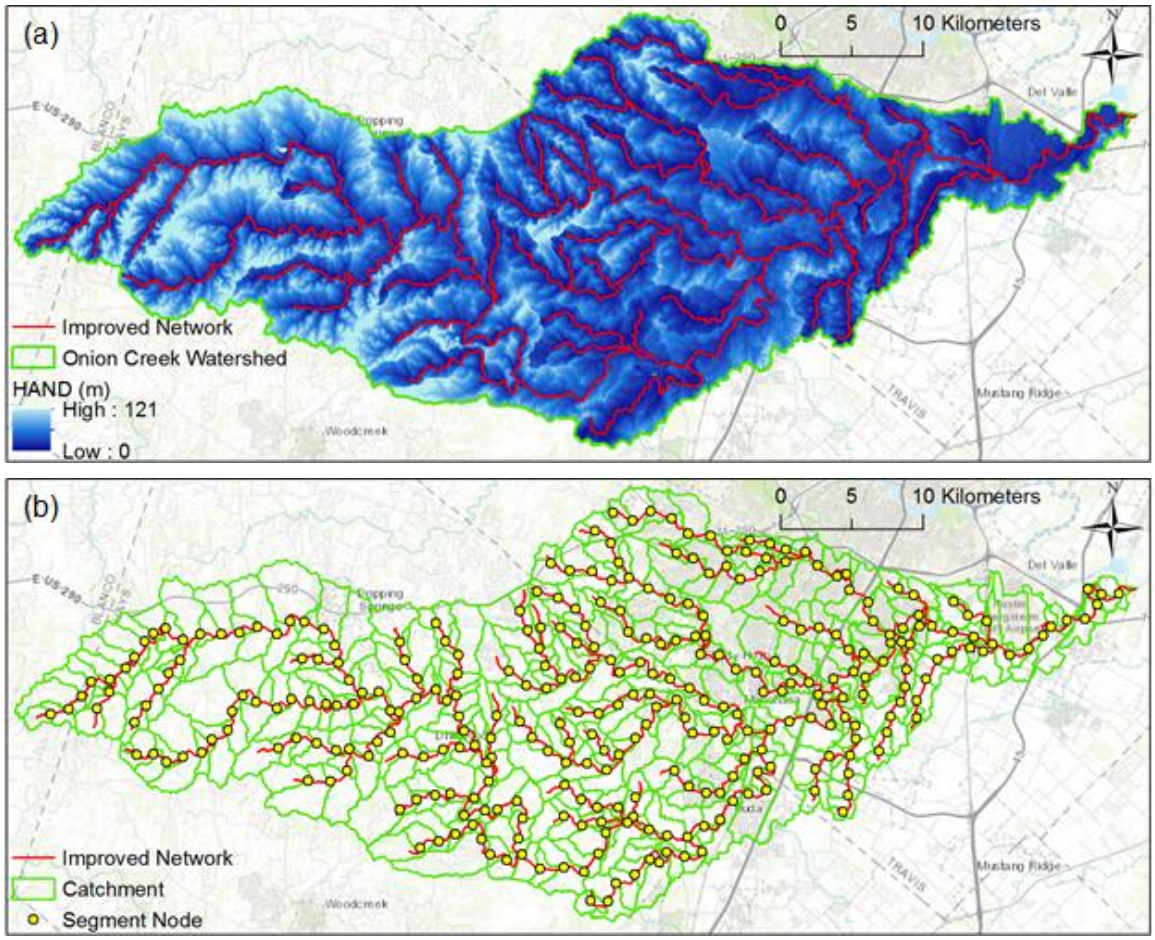

Figure 3.4: Hydrological terrain analysis products for the Onion Creek Watershed. (a) The improved river network extracted with the GeoFlood approach, overlaid with the 3-meter HAND raster generated from the LiDAR-derived DEM. (b) Constant-length segments along the network and local drainage catchment delineated for each segment. Flowlines that share the same stream level are merged as one. Each segment starts from the downstream end of each merged flowline.

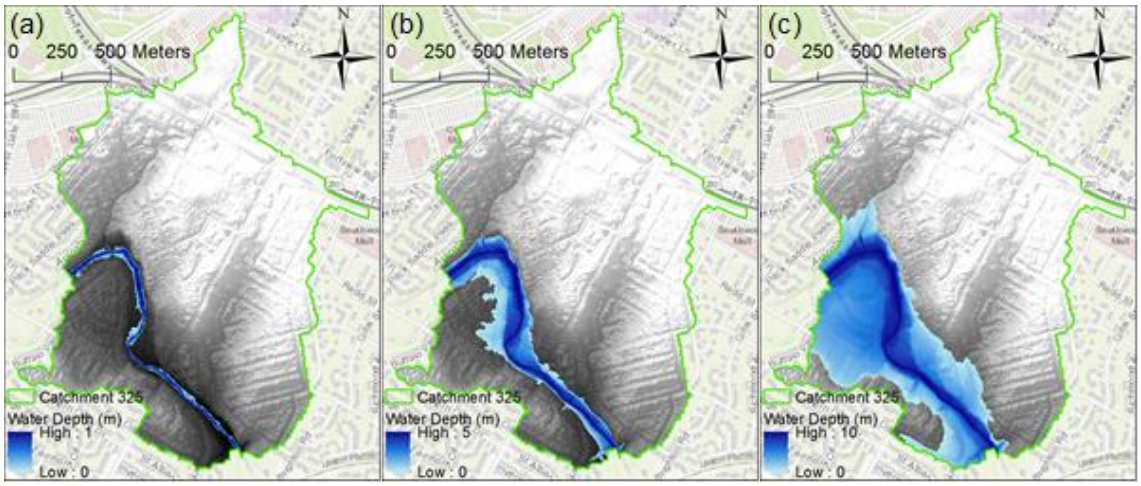

Figure 3.5: Example of GeoFlood inundation mapping derived from the HAND raster corresponding to the 1-meter (a), 5-meter (b), and 10-meter (c) water depth.

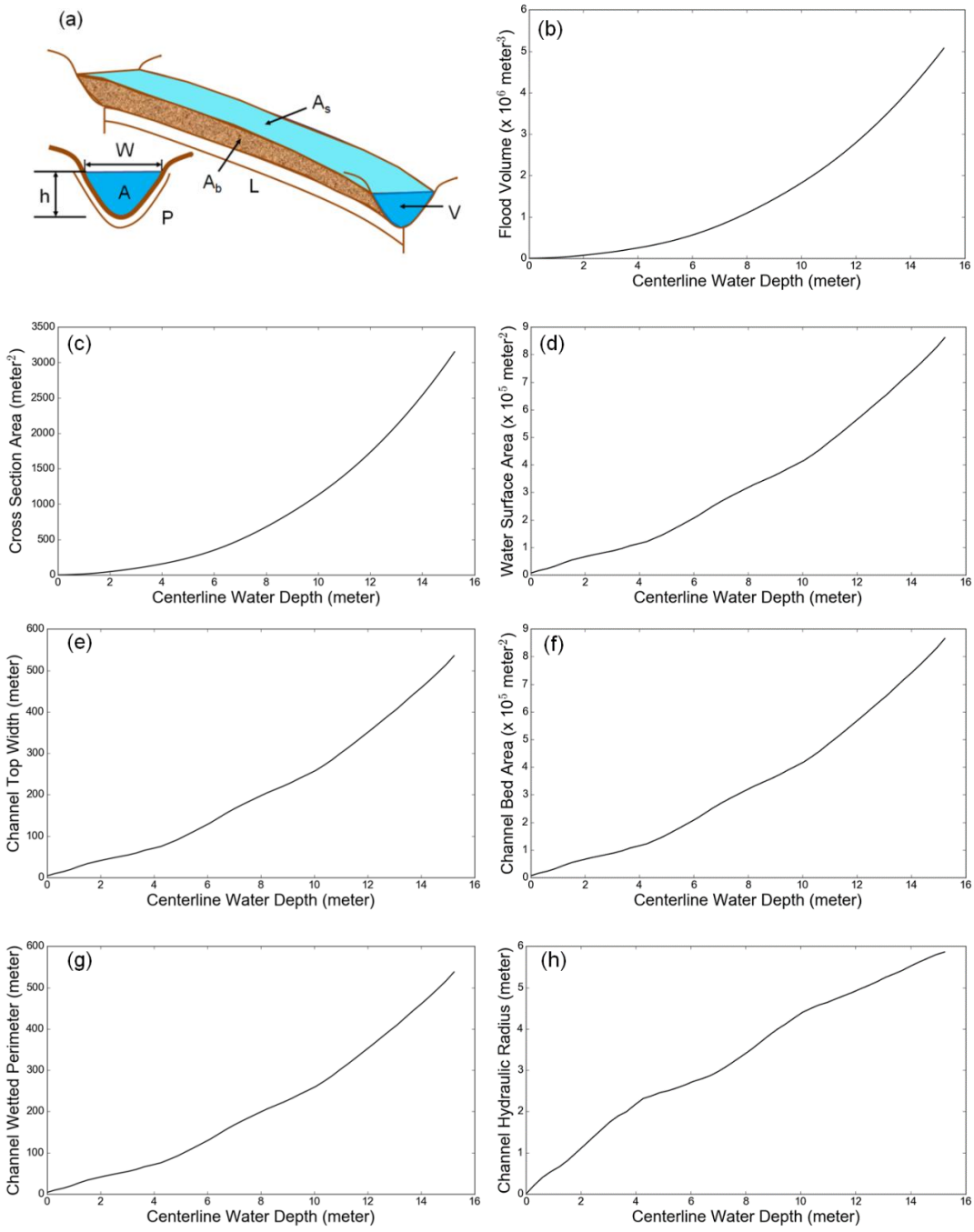

Figure 3.6: Schematic representation of a channel segment (a) and example of channel hydraulic parameters derived from the HAND raster: flood volume (b), cross section area (c), water surface area (d), channel top width (e), channel bed area (f), channel wetted perimeter (g), and channel hydraulic radius (h).

These hydraulic parameters (Figure 3.6) are used in Manning's equation to derive a stage-discharge rating curve for each segment. Since all the rivers have been simulated with hydraulic models, the median Manning's n value of all intersecting cross sections is given by the reach-average value for a segment. If a USGS gauge measured rating curve is available, we compare our HAND-derived synthetic rating curve of the segment to the field measurement where the gauge is located.

To quantitatively evaluate the performance of the HAND-derived rating curves, we compute the difference in water depths converted from the 100-year flood discharge with two types of rating curves. If the 100-year flood discharge is beyond the range of the gauge-measured rating curve, we use the 10-year flood discharge instead. The flow conditions of given return periods are estimated from flood frequency analyses conducted by local model providers (FEMA, 2016).

The results (Figure 3.7, Table 3.2) show that for the same magnitude flowrate of a given return-period flood, the water depth converted from HAND-derived synthetic rating curves has an error of up to 30%. We find that the error tends to be larger on large rivers where the normal depth is deeper, compared to small tributaries. Two possible factors may account for this error: (i) the uncertainty of the roughness value applied in the Manning's equation, which we discuss in a later section; and (ii) the bathymetric information under normal flow condition, which is missing in lidar-derived terrain datasets (most of lidar data are collected using a laser beam, which has limited capability of penetrating the water). Although it may lead to water depth underestimation, the effect on the final mapping accuracy may not be equivalently large, considering the limited portion of the total flood volume occupied by water in the channel during extreme flood events. We will return to this point later in this paper.

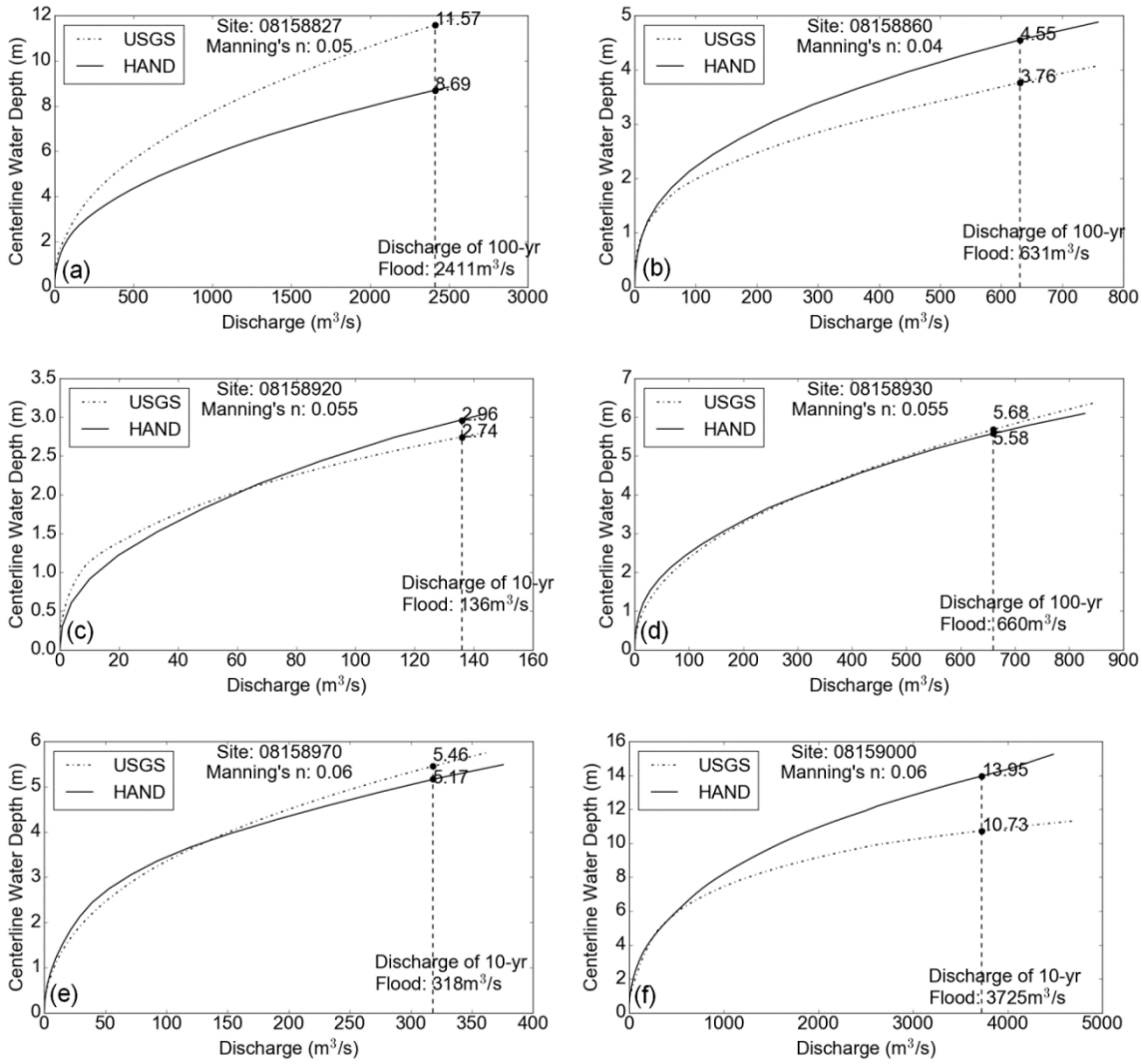

Figure 3.7: HAND-derived synthetic rating curve and USGS gage-measured rating curve comparison at six USGS stream gages in the Onion Creek watershed: (a) Onion Creek at Twin Creeks Road near Manchaca, TX; (b) Slaughter Creek at FM 2304 near Austin, TX; (c) Williamson Creek at Oak Hill, TX; (d) Williamson Creek at Manchaca Road, Austin, TX; (e) Williamson Creek at Jimmy Clay Road, Austin, TX; (f) Onion Creek at US Highway 183, Austin, TX.

Table 3.2: Comparison of water depths converted with HAND-derived synthetic rating curves and USGS gage-measured rating curves for given return-period discharges.

USGS Stream Gauge Site ID	Discharge (m^3/s)	Return Period (year)	Manning's n	Gauge Measure Water Depth (m)	HAND Derived Water Depth (m)	Absolute Error (m)	Relative Error (%)
08158827	2411	100	0.05	11.57	8.69	2.88	24.89
08158860	631	100	0.04	3.76	4.55	-0.79	-21.01
08158920	136	10	0.055	2.74	2.96	-0.22	-8.03
08158930	660	100	0.055	5.68	5.58	0.1	1.76
08158970	318	10	0.06	5.46	5.17	0.29	5.31
08159000	3725	100	0.06	10.73	13.95	-3.22	-30.01

Acknowledging the uncertainties associated with the HAND-derived reach-average rating curves, we use these curves to convert the 100-year-flood information from FEMA-approved HEC-RAS models into corresponding centerline water depth for each river segment. Within a single river segment, the centerline water depth is assigned as a constant value. Across different segments, the depth varies but the variation along a river is still within a reasonable range (Figure 3.8). The HAND raster is then used to map the corresponding inundation zone of each catchment. The output inundation extent map is then compared to the FEMA 100-yr inundation maps. Only river segments covered by FEMA hydraulic simulation are considered in the comparison. The results show that in general, our method can reproduce 60%~90% of the FEMA floodplain coverage (Figure 3.8, Figure 3.9, Table 3.3).

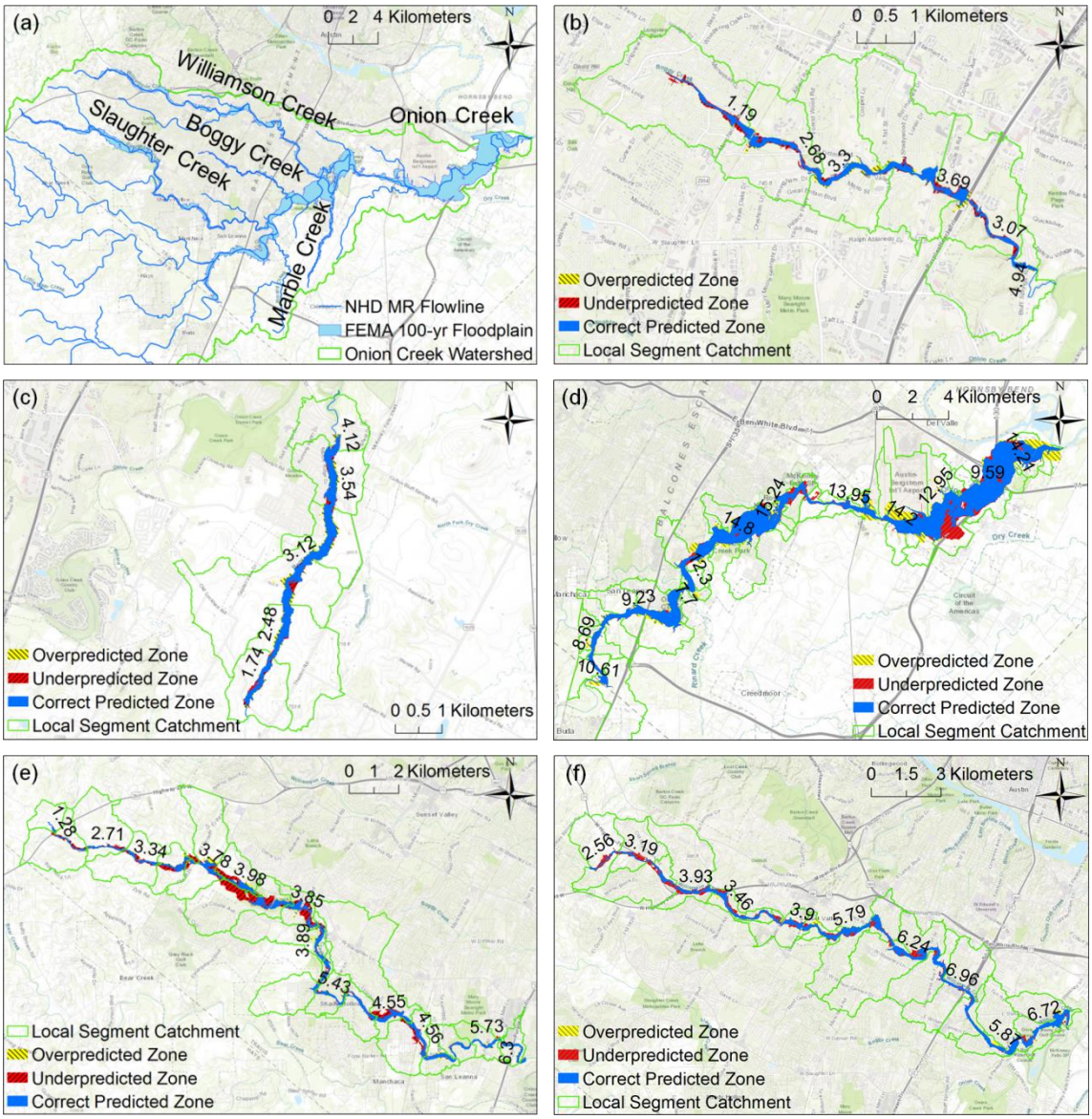

Figure 3.8: Comparison of HAND 100-year inundation extent and FEMA 100-year inundation layer (a) on Boggy Creek (b), Marble Creek (c), Onion Creek (d), Slaughter Creek (e), and Williamson Creek (f).

Table 3.3: Summary of HAND and FEMA 100-year inundation extent comparison

River	HAND Inundation Area (x10^4 m^2)	FEMA Inundation Area (x10^4 m^2)	Correct Predicted Area (x10^4 m^2)	Under predicted Area (x10^4 m^2)	Over predicted Area (x10^4 m^2)	F Index	C Index	Area Ratio (HAND/FEMA)
Boggy Creek	56.59	63.96	49.42	14.54	7.17	0.69	0.77	0.88
Marble Creek	89.57	84.14	76.57	7.58	13.01	0.79	0.91	1.06
Onion Creek	2088.44	1931.83	1697.20	234.63	391.24	0.73	0.88	1.08
Slaughter Creek	307.37	437.16	273.69	163.47	33.67	0.58	0.63	0.70
Williamson Creek	358.10	427.34	324.43	102.91	33.77	0.70	0.76	0.84

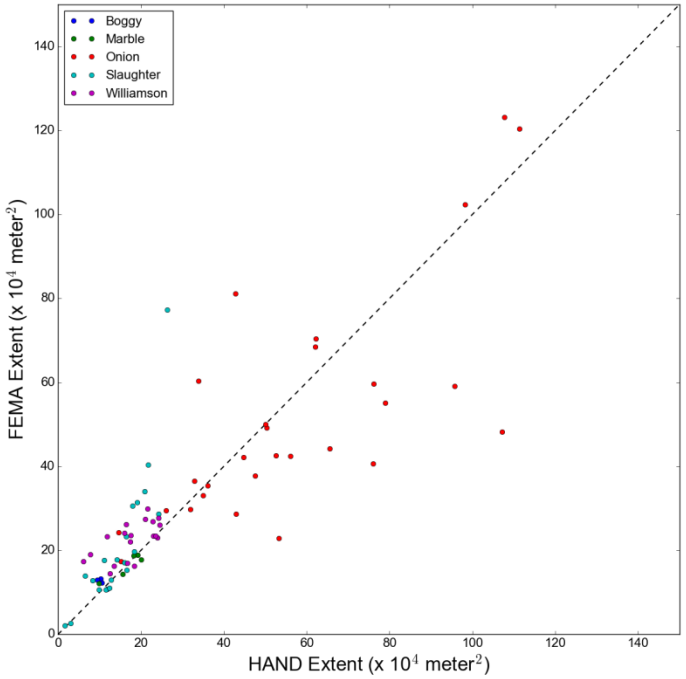

Figure 3.9: Comparison of the 100-year inundation extent spatial cover obtained with HAND and by FEMA.

3.6 SENSITIVITY ANALYSIS: EFFECT OF ROUGHNESS COEFFICIENT AND TERRAIN CHARACTERISTICS

3.6.1 Manning's n adopted in rating curve derivation

The synthetic rating curves were derived with the Manning's *n* value adopted in local hydraulic models for each segment. The roughness coefficient (*n*) is determined by the type and size of riverbed materials, the character of the river, and the vegetation type and density. The coefficient estimated for individual cross sections, thus, may not reflect the average flow resistance of a river segment and large uncertainties exist in the coefficient estimation process. To further understand the effect of the roughness coefficient on the accuracy of the synthetic rating curves, we collected information on the possible Manning's *n* range for each river in the FEMA flood insurance study and tested the sensitivity of the water depth change associated with the change in Manning's *n*. We then tuned the *n* value in the given range to improve the water depth prediction corresponding to a given return-period flow condition. After tuning the *n* value within a range, synthetic rating curves close to the USGS gage measurements can be derived with the HAND approach. We find that careful estimation of a reasonable roughness coefficient is required to predict accurate water depths.

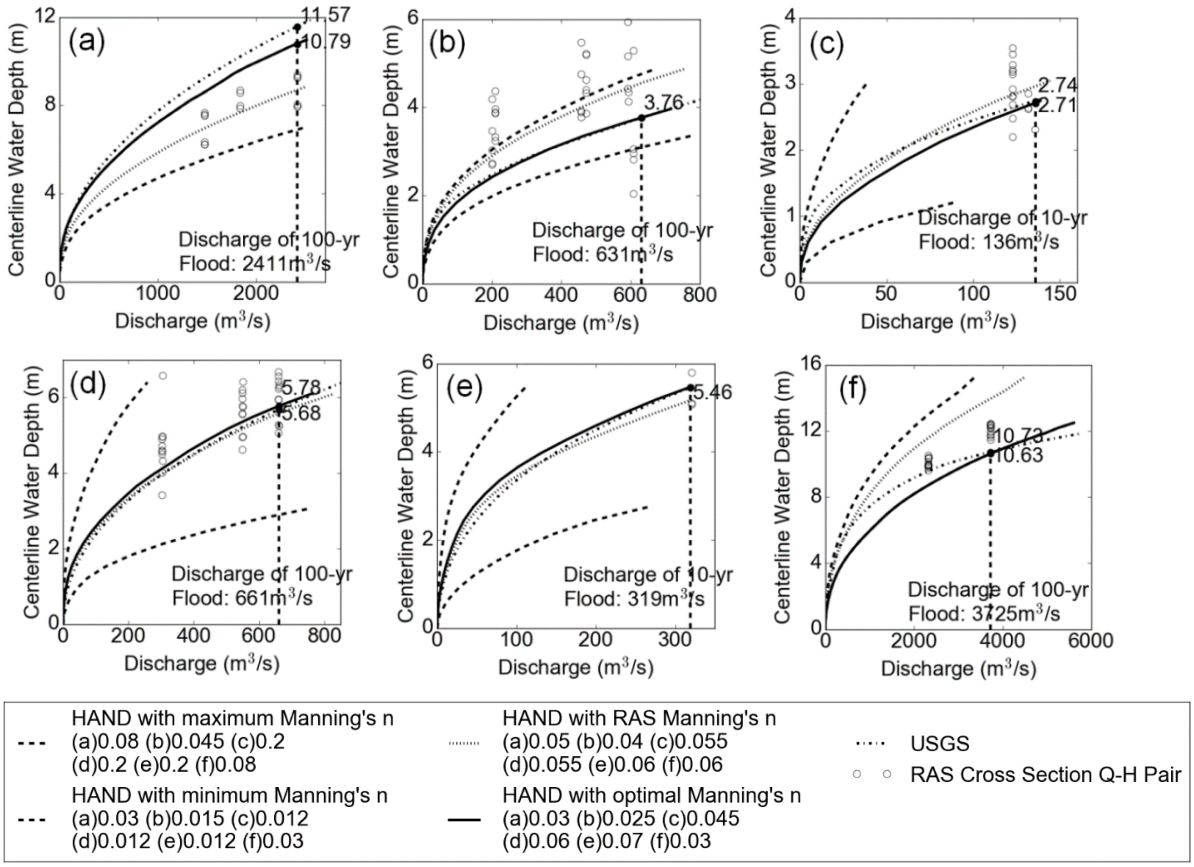

Figure 3.10: Roughness coefficient calibration for HAND-derived synthetic rating curve performance improvement with USGS gage measured rating curves and HEC-RAS simulated flow-depth data pairs as reference: (a) Onion Creek at Twin Creeks Road near Manchaca, TX; (b) Slaughter Creek at FM 2304 near Austin, TX; (c) Williamson Creek at Oak Hill, TX; (d) Williamson Creek at Manchaca Road, Austin, TX; (e) Williamson Creek at Jimmy Clay Road, Austin, TX; (f) Onion Creek at US Highway 183, Austin, TX.

In the current implementation of GeoFlood, a constant roughness coefficient is assigned to a given river segment without considering the resistance difference between the channel and the floodplain. Implementing a compound channel floodplain approach is possible but requires an approach for identifying the location where roughness or geometric changes occur. We do not explore the compound approach here. However, it is

a promising direction for future work that could improve the performance of HAND-derived synthetic rating curves.

3.6.2 Evaluation of uncertainty propagation from rating curve to flood extent

To better understand how the uncertainty in rating curves caused by the adoption of different Manning's *n* affects the accuracy of the inundation extent, we produced inundation extent at different water levels, computed the corresponding mapping metrics in comparison with the FEMA extents, and investigated how these metrics vary in the given water level range (Figure 3.11). The water level range is obtained by converting the 100-year flood discharge with the rating curves generated with the maximum and minimum Manning's *n* value for a given reach (Figure 3.10). The results show that the most accurate prediction of water depth does not necessarily result in the highest mapping accuracy. For some catchments (i.e., Figure 3.11(b)(c)), the adjustment of Manning's *n* within a reasonable range still does not ensure the best performance in terms of HAND flood extent, suggesting that additional modifications in the channel bed slope and river geometry estimation may be needed. At other sites, compared to the FEMA 100-year floodplain, the highest F index of the HAND extent reaches 0.79~0.87, which represents the upper limit of the HAND inundation mapping approach. The residual errors are due to the more complex hydrodynamic processes which we are not able to capture with the current approach based only on terrain information.

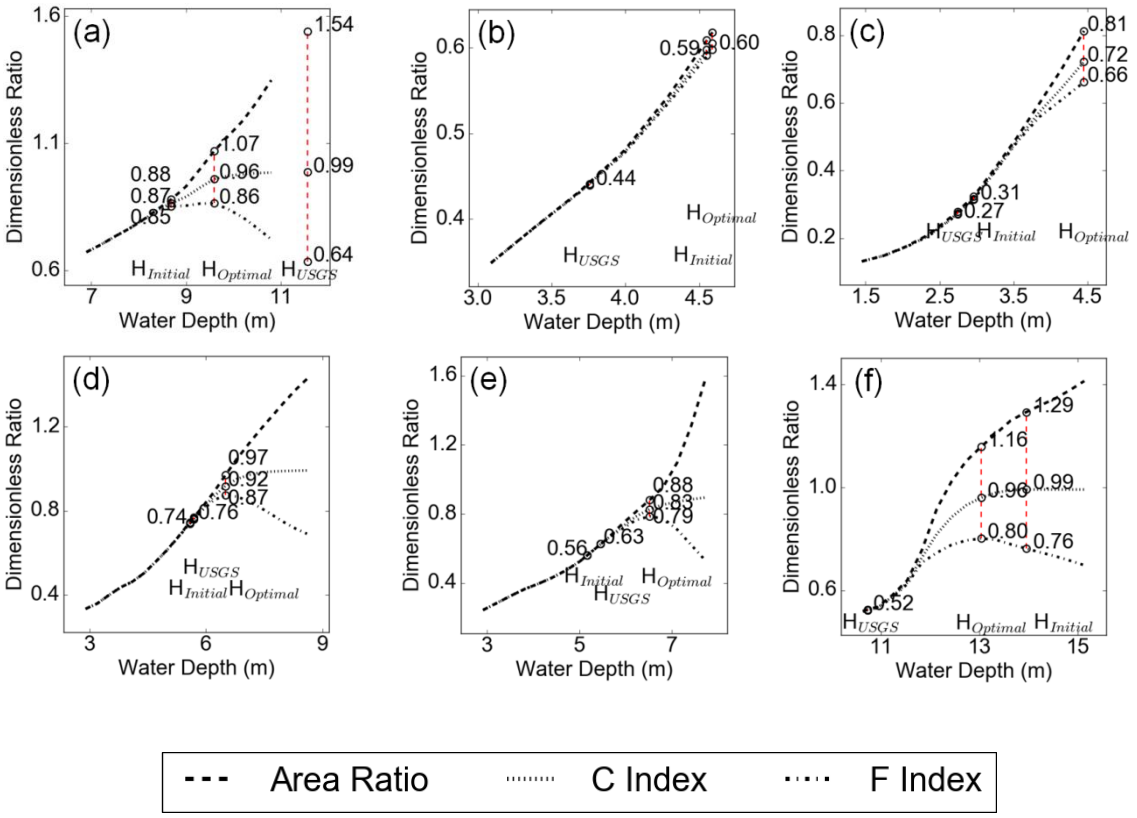

Figure 3.11: Change in the 100-year inundation extent within the water depth range converted from rating curves with different Manning's n values: (a) Onion Creek at Twin Creeks Road near Manchaca, (b) Slaughter Creek at FM 2304 near Austin, (c) Williamson Creek at Oak Hill, (d) Williamson Creek at Manchaca Road, Austin, (e) Williamson Creek at Jimmy Clay Road, Austin, (f) Onion Creek at US Highway 183, Austin. The plot range on the x axis is based on the centerline water depth range corresponding to the 100-year flood discharge (Figure 3.10). The area ratio refers to the ratio of the area of the HAND inundation extent to that of the FEMA 100-year floodplain.

3.6.3 Analysis of catchments with lower mapping accuracy

We examine the limitations of GeoFlood in two catchments where the lowest mapping performance was reported.

The first catchment analyzed is that draining to segment 237 in the Onion Creek watershed (Figure 3.12). This catchment has a unique topographic setting: the Austin

International Airport is on the left hand side (upper) of the river, representing a typical urbanized flat area, while on the right hand side (lower) is a natural hillside terrain. This difference can be easily seen in both the raw terrain data and the derived HAND product. In addition, several waterbodies unconnected to the main stem of Onion Creek are located on the right hand side of the river. Since our HAND raster is created with the raw DEM instead of the pit-filled elevation, the HAND values of these waterbodies are relatively low, making them more vulnerable to flooding.

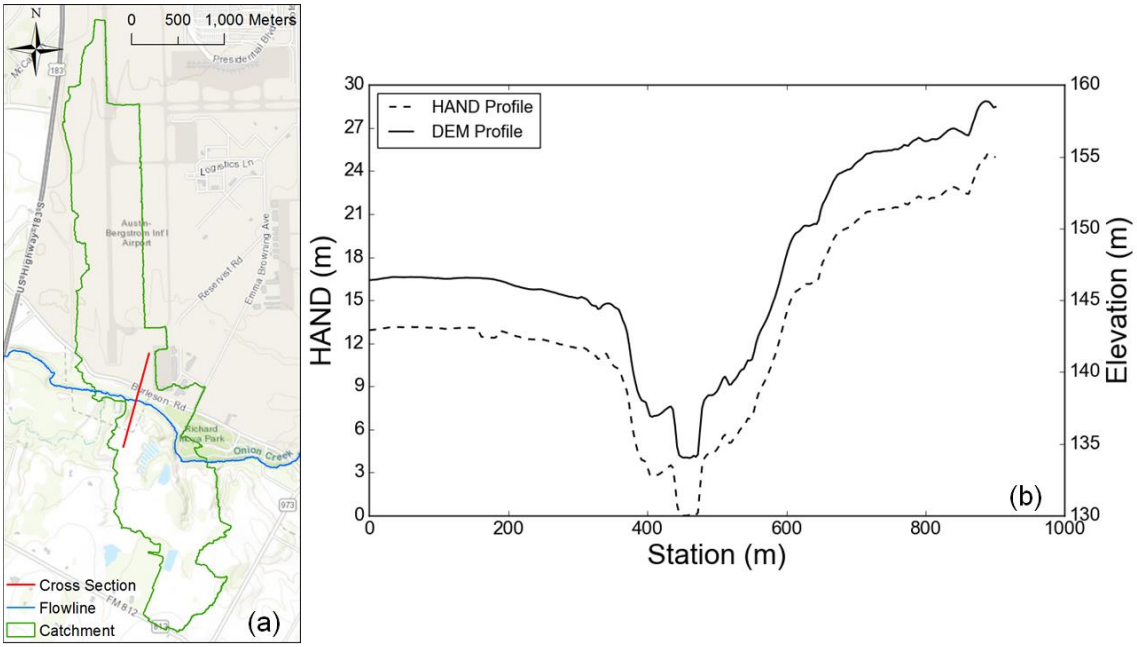

Figure 3.12: The location (a) and profile (b) of a cross section showing the different landscape setting on two sides of a river: a flat, urbanized terrain on the left hand side and a hilly, natural terrain on the right hand side.

The initial HAND calculation for this catchment overestimates the flooding extent, compared to the FEMA 100-yr floodplain (Figure 3.13a). This initial extent was generated from the HAND raster using a threshold of 14.2 meters, given by the 100-yr flow on the HAND-derived synthetic rating curve. In order to better match our inundation

extent with the FEMA one, we identified the HAND values of the pixels on the edge of the FEMA floodplain, and used these values to produce updated flooding extents. The extent corresponding to 12.7-meter water depth was created to capture the sharp edge on the upper left corner (Figure 3.13b). Another extent corresponding to 11.2-meter water depth was created to capture the boundary on the right hand side (Figure 3.13c). The results demonstrate that even with a significant change in water depth of 3 meters, if the channel/floodplain is well-shaped as in the natural landscape, the variation in flooding extent is relatively small; on the other hand, for flat, urbanized areas, the inundation extent obtained with the HAND approach changes dramatically with small changes in water depth. This analysis illustrates that our HAND inundation mapping approach is more suitable as an approximate flood mapping strategy for rural areas. Also, local depressions such as ponds or waterbodies can be identified as flooded with the HAND approach even if they are not connected with the main stem river.

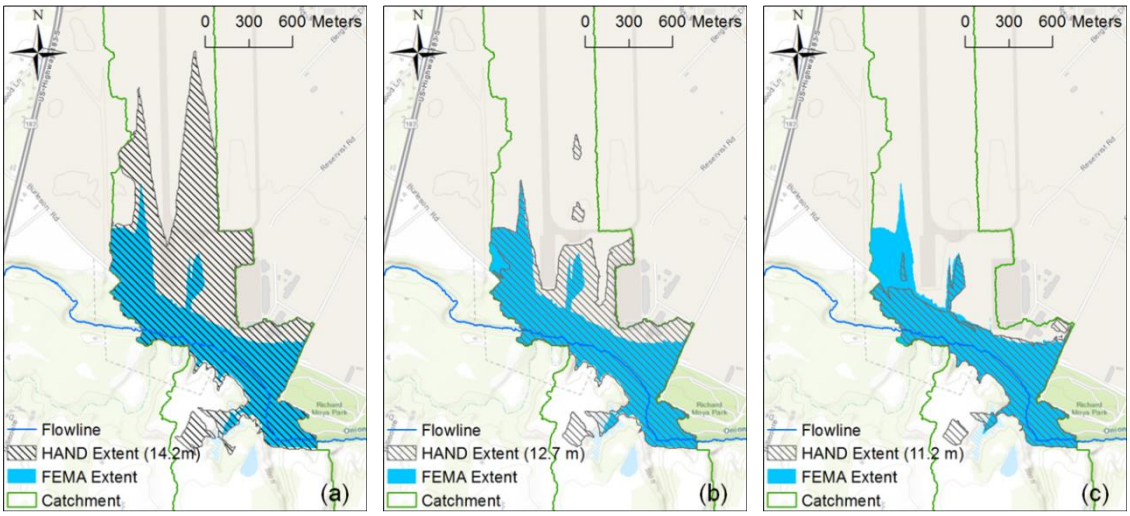

Figure 3.13: Inundation extents generated with the HAND approach corresponding to the 14.2-meter (a), 12.7-meter (b), and 11.2-meter (c) water depth, showing how the sensitivity of mapping accuracy is affected by local topographic setting.

To illustrate how the flow direction change associated with water depths affects the flood extent accuracy, we analyzed the second catchment corresponding to segment 254 on Onion Creek (Figure 3.14). Part of a local road is identified as the catchment boundary. Here on the east side of the catchment boundary road, the elevation drop in the raw DEM is larger than that in the HAND raster, as the stream segments chosen as the local datum for the HAND computation are different for two sides of the road: the closer upstream segment is the datum for the western side and the further downstream segment is the datum for the eastern side. This choice results in relatively high HAND values for the eastern side pixels. However, the water depth of the upstream segment is higher than the HAND value at the catchment boundary, the nearest draining river segment for the eastern side pixels changes from the downstream one to the upstream one, reflecting the actual flood vulnerability in this area. This change is not addressed by our current method

as the nearest drainage relationship and the corresponding HAND values are always fixed for different water levels. Therefore, the flooded area near the catchment boundary is underestimated (Figure 3.15). The top elevation of a highway that passes through this catchment is detected by the lidar data, resulting in high HAND values for pixels where the highway bridge passes through. Therefore, the inundated area around the highway is also underestimated. This is a limitation of our approximate inundation mapping method due to the use of terrain information only. Detailed hydraulic models are able to account for artificial structures and may be necessary to depict a more accurate inundation extent in the proximity of these structures.

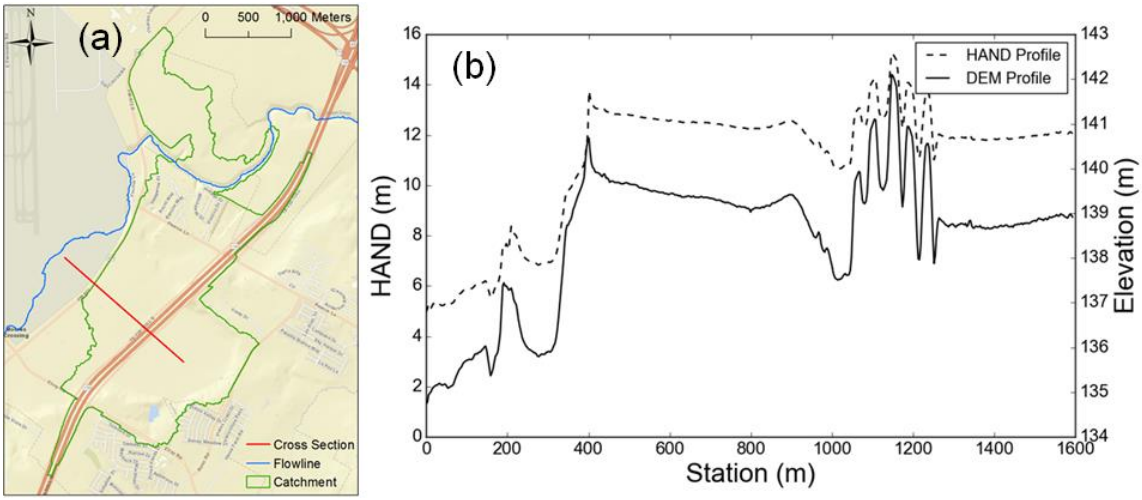

Figure 3.14: The location (a) and profile (b) in correspondence of artificial structures.

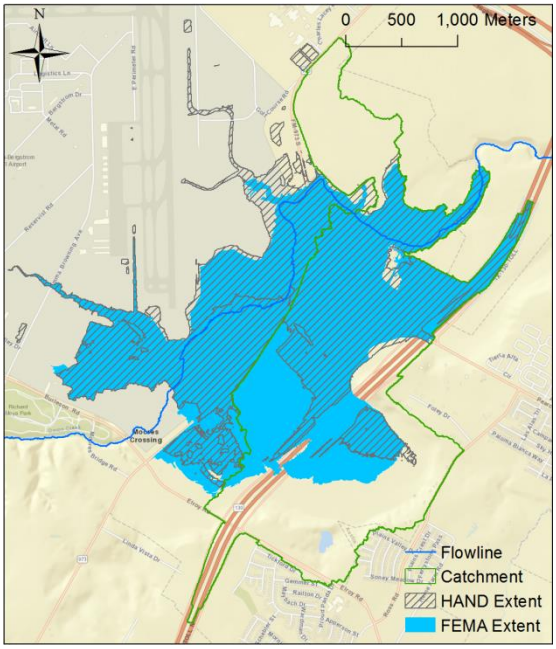

Figure 3.15: Underestimated HAND inundation extents caused by the change of drainage pattern at different water levels and artificial structure elevation recorded in the DEM.

3.7 CONCLUSIONS

Fast-deployable, frequently-updated, and high-resolution inundation mapping with broad coverage products are increasingly needed to support flood emergency preparation and response, calling for higher timeliness requirements to current mapping strategies. The increasing availability of high-resolution topography data over large areas makes its application in inundation mapping practice imperative. Additional challenges have to be addressed, including the high computational cost.

We presented a workflow, called GeoFlood, to address these challenges that relies on the application of the Height Above Nearest Drainage method to lidar-derived high-resolution DEMs. In particular, we presented a detailed analysis of a watershed in central Texas characterized by heterogeneous topography. Our proposed method extracts a high-fidelity network with a predefined network structure and density, derives reach-average

channel hydraulic properties and stage-discharge rating curves for constant-length river segments in the network, and produces inundation maps for any segment of interest given the flood discharge. We compared our rating curves to USGS gage measurement and the inundation maps obtained with GeoFlood to those generated with detailed local hydraulic studies. Our results show that the inundation extent produced by our method overlaps 60%~90% percent of the extent computed with models. A sensitivity analysis shows that the accurate estimation of the roughness coefficient impacts the performance of the method in estimating an accurate synthetic rating curve. Also, the change in inundation extent corresponding to the change in water depth is larger in flat areas with artificial structures than hilly terrain, indicating that our method performs better as an approximate inundation mapping method for fluvial flooding in hilly areas over large scales.

The novelty of our method lies in the adoption and enhancement of an advanced channel extraction approach, GeoNet, which is designed for analyzing high-resolution LiDAR-derived topographic data, in order to meet the requirements associated with inundation mapping. The original NHDPlus network, which is the foundation of continental-scale hydrologic simulation, is reorganized into constant-length segments as parts of a continental-scale hydraulic framework to provide stable reach-average channel properties and synthetic rating curves. Our test results show that, given a sound estimation of the roughness coefficient, HAND-derived synthetic rating curves can approximate USGS gage-measured stage-discharge relationships, which will be useful for hydrologic and hydraulic analyses in ungauged watersheds. While detailed terrain information is used in our inundation mapping strategy, its complexity and computational cost are still relatively low compared to fully-physical hydrodynamic approaches, making it a promising tool for large scale inundation mapping of high resolution.

Chapter 4: An automatic and objective approach to hydro-flatten high resolution topographic data[3]

4.1 ABSTRACT

Hydro-flattening is an operation often required to generate deliverable terrain products after lidar survey collections and it usually requires extensive manual intervention. In this paper, we develop new modules of GeoNet, a computational tool for the automatic extraction of geomorphic channel features from high resolution topography, for detecting channel banks and produce a hydro-flattened Digital Terrain Model (DTM). We first review the original GeoNet workflow and then describe how it has been modified to extract a river network with given channel heads and outlets. A modified cost function is used to extract channels as the least-cost-paths from channel heads to outlets. A new code component enables the identification of the hydro-flattened zone using curvature and connectivity information. A raster-based routine for extracting the geomorphic channel zone based on a statistical analysis of slope distribution has also been added to the toolbox. We tested our new components using three different test cases. Compared to manually delineated hydro-flattened zones and to the water extent identified from satellite imagery, our results show high consistency and the capabilities of our method to automatically perform hydro-flatten high-resolution topographic data.

4.2 INTRODUCTION

Over the last two decades, the availability of high resolution terrain data obtained using remote-sensing techniques has provided an unprecedented opportunity for better understanding Earth surface features and processes (Tarolli, 2014; Passalacqua et al.,

[3]The text contained within this chapter has been submitted in Environmental Modelling and Software (EMS).

2015). Among these technologies, airborne lidar (Light Detection and Ranging) has been a game changer (Tarolli et al., 2009; Roering et al., 2013). Both the raw data and information derived from point clouds have been widely used in geomorphology (Hilldale et al., 2008; Notebaert et al., 2009; Hohenthal et al., 2011), hydrology (Lyon et al., 2015), flood risk evaluation (Casas et al., 2006; Bates, 2012; Chen et al., 2017), and natural resources management (Hudak et al., 2009). In all these applications, the extraction of land surface features such as coastlines (Stockdonf et al., 2002; Liu et al., 2007; Chust et al., 2008), roads (Ferraz et al., 2016), terrain depressions (Doctor et al., 2013), waterbodies (Toscano 2015), and river networks (Passalacqua et al., 2010a; Pelletier 2013; Sangireddy et al., 2016) has been challenging.

Among features of interest on the Earth surface, the boundary between a river and its floodplain is critical for improving the performance of channel routing schemes and inundation mapping, as distinct geometry and roughness characterize these two portions of a landscape. Being able to distinguish these two featuress has become even more important with the implementation of continental-scale hydrologic simulations (Maidment, 2017).

A similar task commonly conducted in cartography is hydro-flattening. During this process, breaklines are added along the banks of surface waterbodies to identify the boundary between water and land. When a surveying plane collects data over surface waterbodies, the return signal provides elevation information from the water surface, ground underneath the surface, and vegetation over the surface. The portions of the landscape with water have to be identified and delimited by breaklines and a constant slope applied to these areas. In this way, acceptable water surfaces are ensured in the final digital terrain products.

The difference between geomorphic bankline detection and cartographic breakline delineation is that a bankline is overall static unless significant geomorphic change happens through time while a breakline only represents the instantaneous water-land boundary during the survey period and varies with flow conditions (Figure 4.1). Thus, breaklines represent the land-water boundary in regular flow conditions while banklines represent the land-water boundary in flooding condition.

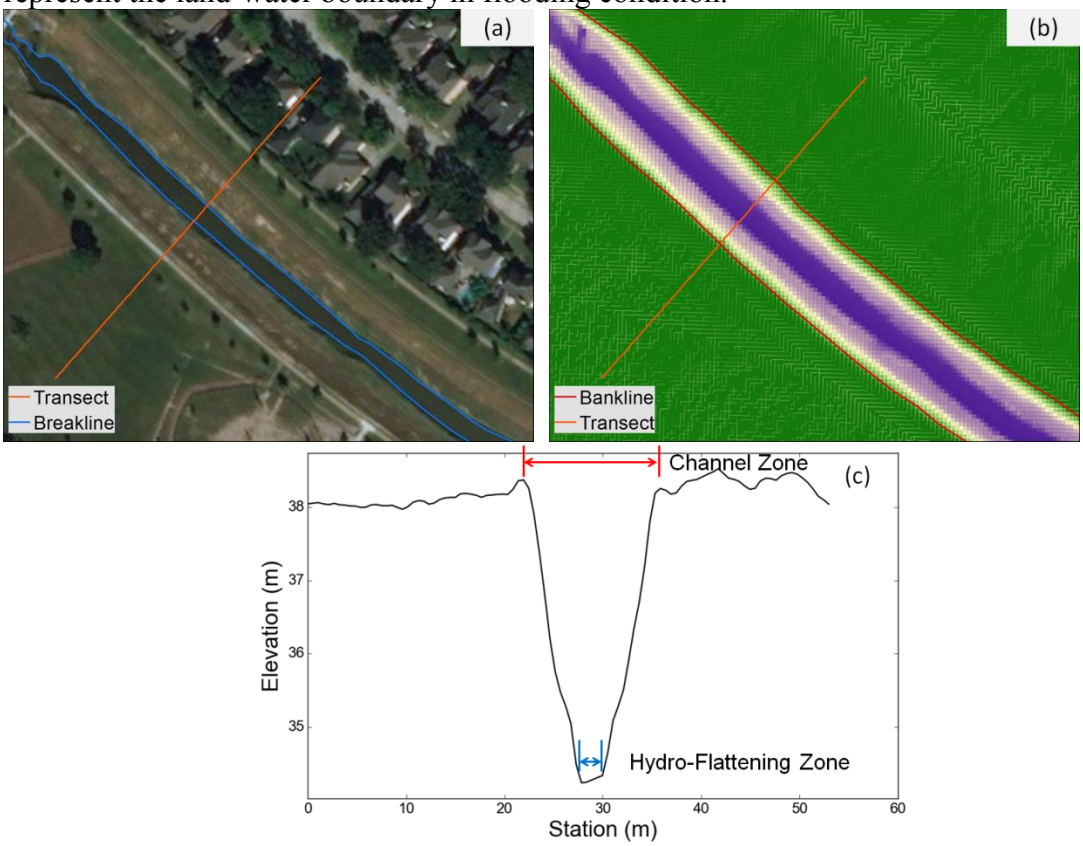

Figure 4.1: Illustration of the difference between a geomorphic bankline and a cartographic breakline: (a) breakline with high-resolution satellite imagery as background; (b) bankline with high-resolution terrain as background; (c) elevation profile along the transect.

In the past, the delineation of banklines and breaklines has been conducted manually, which was expensive, time-consuming and labor-intensive. Automatic approaches have been developed and tested; some of them rely on the raw point cloud for classification, while others extract information from the elevation, signal intensity, and point density raster. Höfle et al. (2009), for example, proposed a method that first applies an intensity correction and a dropout (signal absent zone) simulation, and then uses an object-based classification to identify the land-water-surface boundary from point-cloud-derived segments. Another study used the NHD flowline as reference (Deshpande et al., 2017), to trace cross sections perpendicular to the reference line and identify the lowest elevation point along the cross section as water surface elevation. Then, a constant level was added to that elevation to generate a virtual water surface, the intersection between this virtual surface and the raw surface identifies the bank location. A problem associated with using raw point clouds is that the size of the raw data is much greater than the processed raster products, requiring more computational resources. Other methods extract breaklines by combining elevation and intensity data (Toscano et al., 2013; Toscano et al., 2014; Acharjee, 2017), or point density information (Smeeckaert et al., 2013; Johansen et al., 2011; Johansen et al., 2013; Worstell et al. 2014).

There are two limitations when using lidar return intensity information for water classification: first, significant variation in return intensity can be present within the waterbodies (Acharjee, 2017; Chen et al., 2017), making the low intensity assumption used in water classification problematic. Additionally, intensity data are not as widely available as elevation. Furthermore, density-based approaches may misclassify roads as water. The density difference between land and water may not be detectable if the water depth in a channel is shallow or the channel is located in survey strip overlapping zones.

Here, we propose a method to hydro-flatten high resolution topographic data by using only the elevation raster, which is the most commonly available topographic data product. Our approach uses only few adjustable parameters whose values are applicable to a variety of areas. The proposed method builds upon GeoNet (Passalacqua et al., 2010a, Sangireddy et al., 2016), an open source, automatic tool for geomorphic feature extraction from high resolution topographic data. In GeoNet, a nonlinear filter is first applied to the elevation data to remove local terrain variablity and enhance features of interest. Terrain attributes, including curvature and flow accumulation, are computed from the filtered DEM. Based on a properly defined cost function, channel centerlines are extracted as lines of minimum cost from each channel head to the watershed outlet. The first version of GeoNet only extracted channel heads and centerlines (Passalacqua et al., 2010a). Later on, we added tools for extracting channel cross sections, bank locations, and bankfull water surface elevation (Passalacqua et al., 2012). Recently, the channel head and centerline extraction portion has been rewritten in Python from the original MATLAB and C version (Sangireddy et al., 2016). However, the cross section and bank extraction portion has not been added and its capability of detecting geomorphic banklines has not been tested.

The goal of this paper is to propose a better solution for extracting geomorphic banks over large-scale river networks and estimating reach-average bankfull width using GeoNet. We first describe the three study areas used to test our tool (Section 4.3). We then review the original GeoNet workflow, and discuss its limitations in delineating channel banklines (Section 4.4.1). Next, we present our proposed approach to solve these limitations (Section 4.4.2), and implement it in our study sites. We compare the results to

observations to demonstrate the effectiveness of our method and identify its limitations (Section 4.5). Finally, we summarize the conclusions of this work (Section 4.6).

4.3 STUDY SITES

4.3.1 Natural basin: East Branch Sturgeon River subwatershed, MI

The East Branch Sturgeon River subwatershed (Figure 4.2) is located in Dickinson County, Michigan. It has a total drainage area of 55.32 km^2 and the total length of the NHDPlus river network within it is 9.84 km. The maximum annual mean flow of a given stream segment in this basin is less than 0.6 m^3/s. A 1m-resolution lidar-derived bare-earth DEM was provided by National Geospatial Center of Excellence (NGCE) of USDA Natural Resources Conservation Service (NRCS).

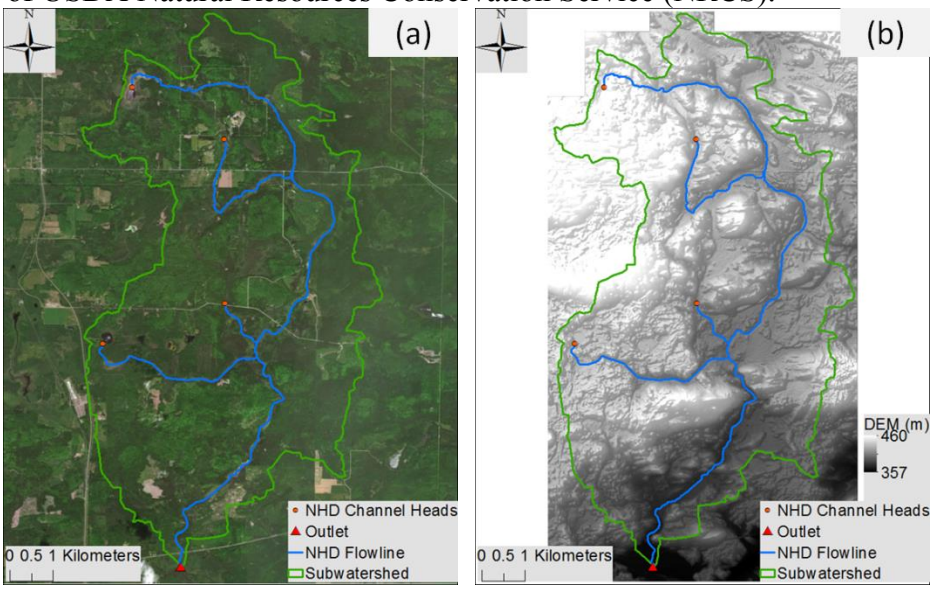

Figure 4.2: East Branch Sturgeon River Subwatershed, Dickinson, MI: (a) NHD subwatershed boundary, flowlines, channel heads, and outlet with satellite imagery as background; (b) 1-meter DEM obtained from NGCE.

4.3.2 Agricultural basin: Stony Creek-Black River subwatershed, NY

The Stony Creek-Black River Subwatershed (Figure 4.3) is located in Lewis County, New York. It has a total drainage area of 71.25 km^2 and the total length of the NHD river network within it is 52.3 km. The main stem river passing through this subwatershed is the Black River, which has a mean annual flow of about 100 m^3/s. As commonly found in agricultural landscapes, in this watershed the flow is also conveyed by artificial drainage ditches. A 1m-resolution lidar-derived bare-earth DEM was provided by NGCE with hydro-flattening breaklines along the main stem river, which will be used as reference to evaluate the performance of our method.

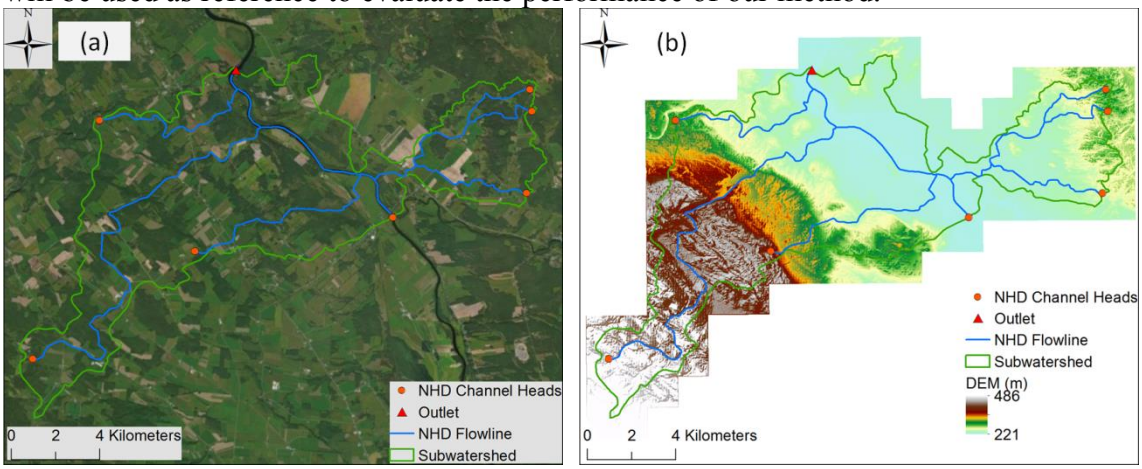

Figure 4.3: Stony Creek-Black River Subwatershed, Lewis, NY: (a) NHD subwatershed boundary, flowlines, channel heads, and outlet with satellite imagery as background; (b) 1-meter DEM obtained from NGCE.

4.3.3 Urban basin: Jersey Lake-Whiteoak Bayou subwatershed, TX

The Jersey Lake-Whiteoak Bayou subwatershed (Figure 4.4) is located in Harris County, Texas and is a part of the greater metropolitan area of the city of Houston area. It is a highly-urbanized area with many artificial structures that act as barriers during the river networking extraction. The total drainage area of this subwatershed is 59.68 km^2

and the total length of the NHD river network within it is 22.2 km. A lidar-derived DEM was provided by Texas Natural Resources Information System (TNRIS) at a resolution of 1.5 meters (5 feet). TNRIS also provided manually delineated hydro-flattening breaklines, which will be used as reference to evaluate the performance of our method.

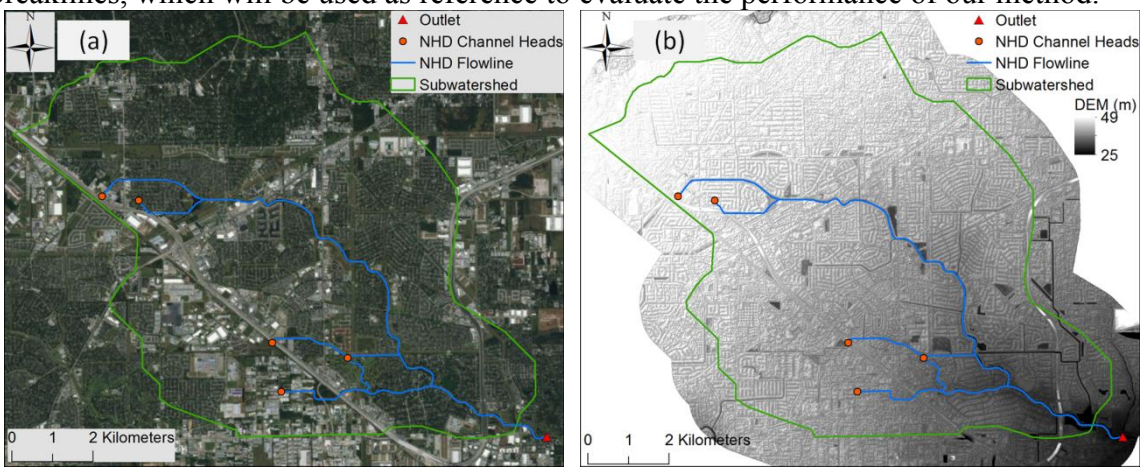

Figure 4.4: Jersey Lake-Whiteoak Bayou Subwatershed, Harris, TX: (a) NHD subwatershed boundary, flowlines, channel heads, and outlet with satellite imagery as background; (b) 1.5-meter DEM obtained from TNRIS.

4.4 METHODS

4.4.1 Review of the original GeoNet workflow

The original GeoNet workflow comprises three major parts: nonlinear filtering of the elevation data, identification of the skeleton (the set of likely channelized pixels) based on curvature and accumulation area computed on the filtered DEM, and a least-cost-path approach for channel network identification.

Filtering is a common operation adopted in feature extraction from lidar data to remove local terrain variability. The most common filter is the Gaussian filter, which can be expressed as:

$$h(x, y, t) = h_0(x, y) \star G(x, y; t) \tag{4.1}$$

where $\star$ denotes the convolution operation, $h_0(x,y)$ represents the raw elevation at location (x,y), $G(x,y;t)$ is a two-dimensional Gaussian kernel with a standard deviation t centered at (x,y), and $h(x,y,t)$ represents the filtered elevation. The value of t specifies the size of the local neighborhood involved in the filtering operation. The main problem associated with this filter is the blurring of the feature edges which limits the ability to detect the exact location of the features of interest (Lashermes et al., 2007; Passalacqua et al, 2010a). Therefore, GeoNet implements a nonlinear filter (Perona and Malik, 1990) defined as:

$$\frac{\partial h(x,y,t)}{\partial t} = \nabla \cdot [c(x,y;t)\nabla h] \tag{4.2}$$

where c is the diffusion coefficient. This coefficient can be computed as:

$$c = e^{\left(-\left(\frac{|\nabla h|}{\lambda}\right)^2\right)} \qquad c = \frac{1}{1 + (\frac{|\nabla h|}{\lambda})^2} \tag{4.3}$$

In the equations above, $|\nabla h|$ is the absolute value of the elevation gradient at location (x,y), t is the iteration time step, and λ is the edge stopping threshold computed as the 90th quantile of the gradient distribution (Perona and Malik, 1990). Since gradients are high across feature boundaries, the diffusion coefficient promotes diffusion within the feature boundaries and penalizes it across the boundaries, so that the exact boundary location is preserved.

Once the filtering operation is completed, curvature is computed on the filtered DEM to help identify likely channelized pixels (skeleton). Two kinds of curvature have been adopted in GeoNet. The first one is the Laplacian curvature, which is defined as the gradient of the elevation gradient ∇h:

$$\kappa = \nabla^2 h \tag{4.4}$$

The second one is the geometric curvature, which is defined as the gradient of the elevation gradient normalized by its magnitude:

$$\kappa = \nabla \cdot \left(\frac{\nabla h}{|\nabla h|}\right) \tag{4.5}$$

The geometric curvature works better for preserving all convergent features and thus it is predominantly used in natural landscapes, while the Laplacian curvature tends to favor the most convergent features and ignore those with smaller curvature (Passalacqua et al., 2012).

This curvature information is used for the extraction of the skeleton by identifying all the pixels with a curvature value larger than a threshold detected from a quantile-quantile plot of curvature. The value of curvature at which the curvature distribution deviates from a straight line in the positive tail marks the transition from hillslopes to valleys (Lashermes et al., 2007). The skeleton of likely channelized pixels based on the curvature threshold can be noisy, as small convergent areas that are not part of the channel network may be identified. Therefore, a thinning operation is performed to thin the skeleton based on flow accumulation area (Passalacqua et al.,2010a).

Once the skeleton is identified, the channel heads and channel network are extracted based on geodesic minimization principles. A geodesic cost function is first computed for each pixel to measure the degree of difficulty for water to pass through it. This cost function ψ is based on topographic attributes (i.e., contributing area (A), curvature (κ), and skeleton (S)) and expressed as:

$$\psi = \frac{1}{1 \cdot A + A_{mean} \cdot S + A_{mean} \cdot \kappa} \tag{4.6}$$

where A_{mean} is the mean flow accumulation area computed across the entire watershed, which is used to normalize the difference in dimension and order of magnitude of the different terms. The geodesic distance of each pixel from the output is

then computed using the fast-marching algorithm (Sethian, 1996) as the minimum cost from that pixel to the watershed outlet.

Following the calculation of geodesic distance, channel heads are identified automatically as the upstream end pixel (with the largest geodesic distance) of each skeleton connected component scanned using a search box. River centerlines are then extracted as the least-cost-path from each channel head to the watershed outlet.

After the extraction of the river network, the original GeoNet workflow allows the extraction of cross sections along the centerlines and the identification of bank locations at each cross section (Passalacqua et al., 2012). For a given location (x,y), the coordinates of stream cells along the same path five units away from it (both upstream (x_u,y_u) and downstream (x_d,y_d)) are used to estimate the streamline direction vector $\vec{r}$ as:

$$\vec{r} = (x_d - x_u)\vec{\imath} + (y_d - y_u)\vec{\jmath} \tag{4.7}$$

Then the orthogonal vector $\vec{c}$ representing the transverse direction is computed as:

$$\vec{c} = (-r_2)\vec{\imath} + (r_1)\vec{\jmath} \tag{4.8}$$

In this way, a cross section with a predefined length L is drawn centered at (x,y) following the direction of $\vec{c}$. To identify the channel bank locations, the slope is computed along the transect and on each side of the centerline, the location corresponding to the peak of the slope is marked as the bank location. Therefore, the original GeoNet workflow can be used to identify banklines by connecting the bank points on adjacent cross sections from upstream to downstream along each centerline of the network. This approach has some limitations as explained in the next section.

4.4.2 New approach for hydro-flattening and bank detection

4.4.2.1 Junction detection and network segmentation

The original GeoNet workflow extracts each channel separately from a channel head to the outlet, resulting in overlapping centerlines on the main stem river (Figure 4.5a). We have added a post-processing operation to properly segment the network at river confluences. In this process, after all the flowlines have been extracted, a table is created with the coordinates of each stream cell and the number of flowlines that pass through that cell. Then the network is reconstructed following the rule that each flowline only owns stream cells with the same passing flowline number. When a change in pass count happens, the original flowline is interrupted, and the start point of a segment with a larger pass count is identified as a junction, unless it coincides with the watershed outlet (Figure 4.5b).

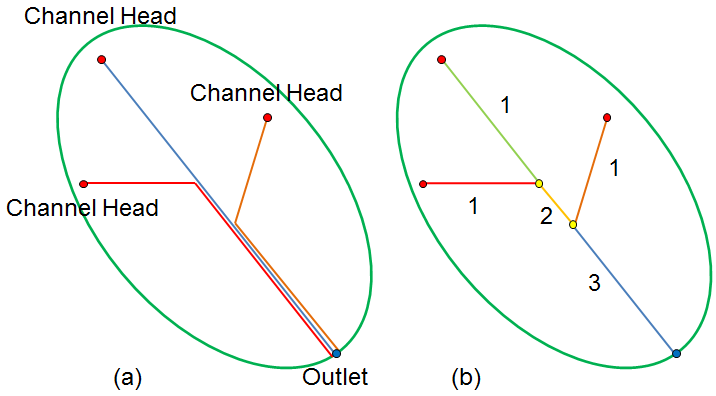

Figure 4.5: Illustration of network segmentation and identification of network junctions: (a) channel network extracted with the original GeoNet workflow; (b) channel network extracted with the new approach. The numbers indicate the pass count of each river segment.

4.4.2.2 Network extraction workflow adjustment and cost function modification

Since our goal is to estimate the bankfull width and conduct the hydro-flattening operation across a large domain, we are only interested in perennial streams, often referred to as "blue-line" streams in topographic maps. Therefore, instead of using the channel heads automatically detected by GeoNet, we extract channel heads from the National Hydrography Dataset Plus Medium Resolution (NHDPlus MR). The NHDPlus MR is a digital database that contains a national-coverage stream network derived from 30 meter resolution National Elevation Dataset (NED) using a classic slope-based approach with extensive manual corrections. Due to the coarse spatial resolution of the input elevation data and the extraction method, the centerlines in the NHDPlus network appear to deviate from the terrain concavities once overlaid on lidar data. While this dataset is only available in the U.S., our approach can be applied in other areas where an equivalent cartographic river network is available.

The channel heads extracted from the NHDPlus MR are used as the starting point of the optimal path searching calculation in GeoNet. The corresponding end point of each path could be the end point of the orginal flowline feature, or the unique outlet of the entire watershed. Either alternative has its pros and cons: if the end point of the original flowline feature is used, the junction locations identified in the initial network are inherited thus the delineation of each flowline can be performed within a local drainage catchment independently, leading to an easy parallel implementation. Also, since the extraction is bounded by the local catchment boundary, shortcuts of least cost paths across catchment boundaries are not possible. Using the outlet of the entire watershed as the end point of all paths, instead, allows GeoNet to automatically extract the network

junctions. However, since in this case paths are searched within a large domain, shortcuts across ridges may appear. Specific examples will be shown in the result section.

Since the channel heads are predefined in our workflow, we do not need to compute the geodesic distance at every pixel, reducing computational expenses. Instead, we only need to find the least-cost-path between each start-end point pair according to the local cost field. As we mentioned in the previous section, the NHDMR river network provides a rough centerline location. Therefore, to further reduce the computational cost, instead of scanning the entire terrain, we can only focus on analyzing a buffer zone around the initial river network and extract within it the features of interest. The flow accumulation computed within the buffer zone may not be the exact upstream drainage area relative to the entire watershed, but the relative magnitude among different pixels indicates which pixel is more likely to be a channel pixel.

In flat areas, or areas with artificial structures, elevation-gradient-based flow accumulation often results in inaccurate flow paths, thus causing problems for the computation of the cost function. Taking a 10^4x10^4 study domain as an example, the order of magnitude for the accumulation term varies from 10^0 to 10^8, while for the curvature and skeleton, the maximum order of magnitude is usually 10^0. The magnitude of the mean flow accumulation area is about 10^4. Therefore, even if A_{mean} is used as a normalization parameter in the expression of the cost function (Equation 4.6), the curvature and skeleton terms are still small, compared to the accumulation value of a downstream stream cell, which may range from 10^6 to 10^8. Thus, flow accumulation tends to dominate the other two terms. To address this issue, we compute the local geodesic cost with a normalized flow accumulation term. The normalization is implemented by first converting the accumulation values to log scale and then

downscaling the log accumulation values from their original range to a range from 0 to 1. To keep the change consistent across different factors, we also perform a normalization of the curvature term. Additionally, we explored the introduction of new terms in the cost function based on our recently proposed Bayesian channel extraction approach (Zheng et al., in review). In this method, information from the approximate river network derived from low-resolution terrain is used as a prior sample space for the extraction of the river network from lidar data. The assumption of this approach is that, given a previously extracted river network within a buffer zone of the actual channel, only nearby cells with an elevation lower than or equal to the elevation of the original flowline feature can be selected as part of the new network. Using this idea, we add another binary term, h, to the cost function, which represents the height of a pixel relative to its nearest original channel pixel. The value of 1 is assigned to the pixels with a negative or zero h, and 0 to those with a positive h. The value of h is obtained by identifying the nearest original channel pixel location for each pixel based on Euclidean distance, and then computing h as the pixel elevation minus the nearest stream cell elevation. Thus, the modified cost function used in this study is given by:

$$\psi = \frac{1}{A_N + \kappa_N + S + h} \tag{4.9}$$

where the N subscript indicates that both the accumulation term (A) and the curvature term (κ) have been normalized. In this formulation, all the terms have the same weight since all of them take values in a range from 0 to 1.

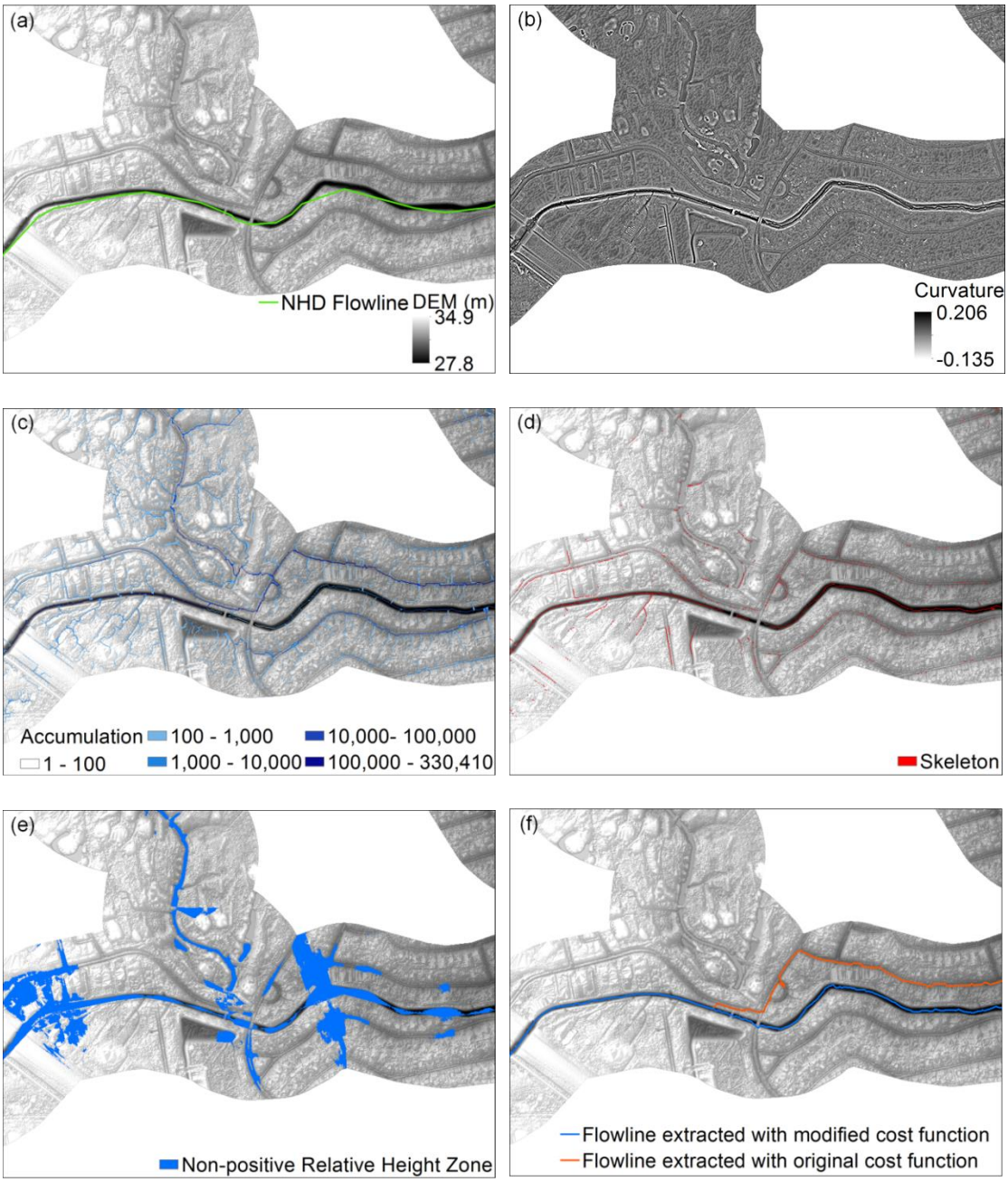

Figure 4.6: Inputs, intermediate variables, and outputs of the network extraction process. (a) Input DEM and NHD flowline; (b) curvature derived from the filtered DEM; (c) flow accumulation (upstream cell numbers) derived from the filtered DEM; (d) skeleton based on curvature and flow accumulation threshold; (e) negative relative height zone computed based on the NHD flowline and DEM; (f) example of flowline extracted with the original GeoNet cost function and modified cost function.

The complete flowchart of the modified river network extraction workflow is in Figure 4.7.

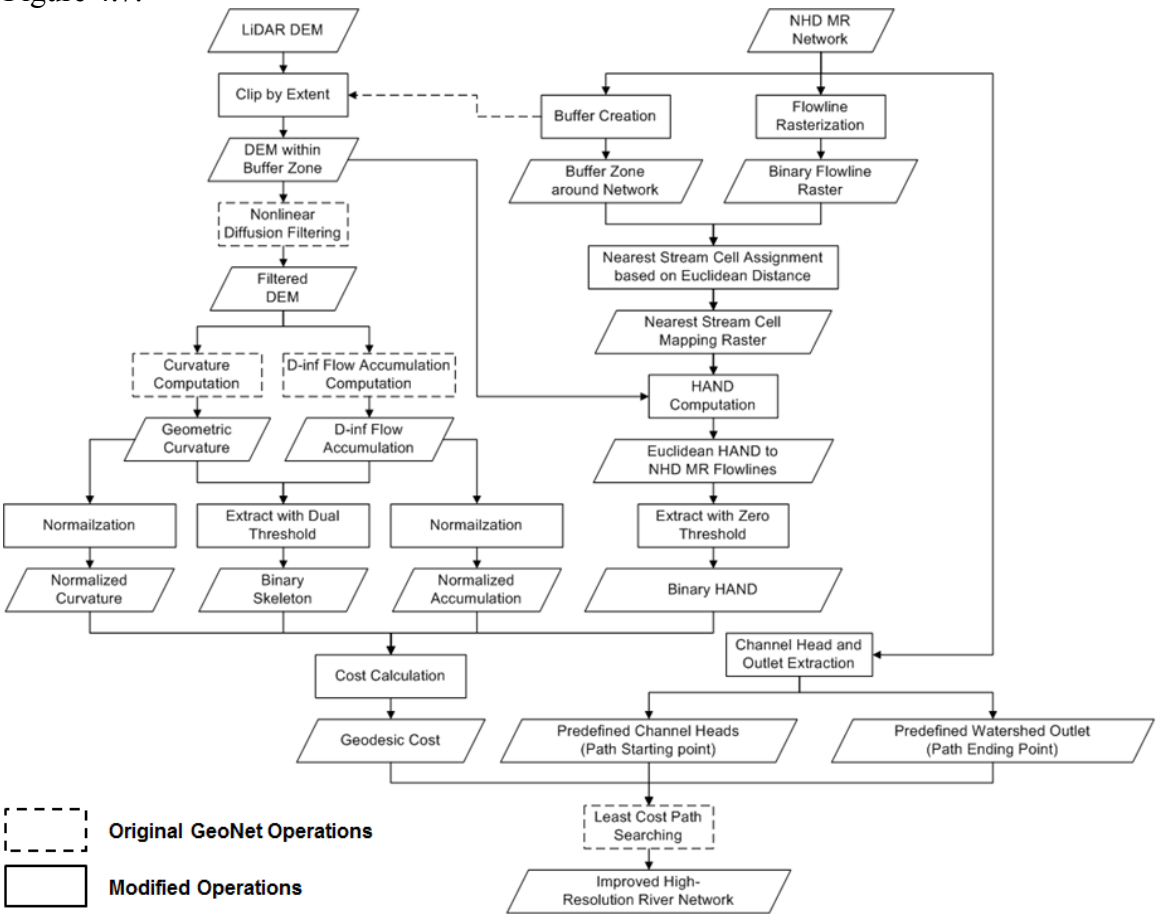

Figure 4.7: Flowchart for the river network extraction workflow, indicating which operations of the original GeoNet workflow have been modified.

4.4.2.3 Raster-based hydro-flatten zone extraction

We propose a raster-based method to hydro-flatten high resolution topographic data based on curvature and connectivity (Figure 4.8). The theoretical foundation of this method is that the channel is a convergent zone of the terrain and thus has positive curvature, while the banks represent the transition from the channel to the floodplain and

have negative curvature. Therefore, by setting a threshold on curvature equal to zero, the channel pixels are above this threshold and any other pixels with zero curvature, which allows us to also detect waterbodies in the watershed. Selecting pixels based on a curvature threshold may result in capturing also convergent features that do not connect to the channel network. We solve this problem by checking the connectivity between the filtered pixels and the network centerlines previously extracted. After identifying all the pixels with a non-negative curvature, we use this filtered raster to mask the flow directions derived from the flow accumulation calculation. Thus keeping only those pixels for which a continuous path can be traced to any centerline pixel following flow directions. The distance from each connected pixel to the extracted centerline is computed and stored in the output raster.

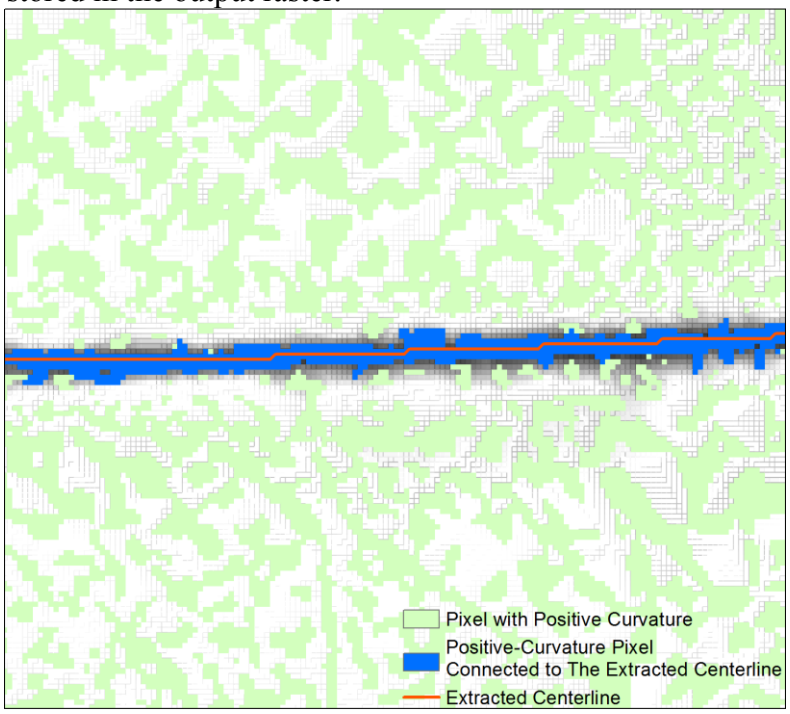

Figure 4.8: Hydro-flattened zone identification based on positive curvature and connectivity to the extracted centerline.

Small tributaries or ditches draining to the main river may be captured with this approach (Figure 4.9). However, since their centerlines are not included as a part of our network, these pixels have a relatively long distance to the centerline. Therefore, we take advantage of this property to exclude these pixels from the final output by imposing a threshold based on the cumulative distribution function of the distance to centerline and deleting all the pixels with a distance above this threshold.

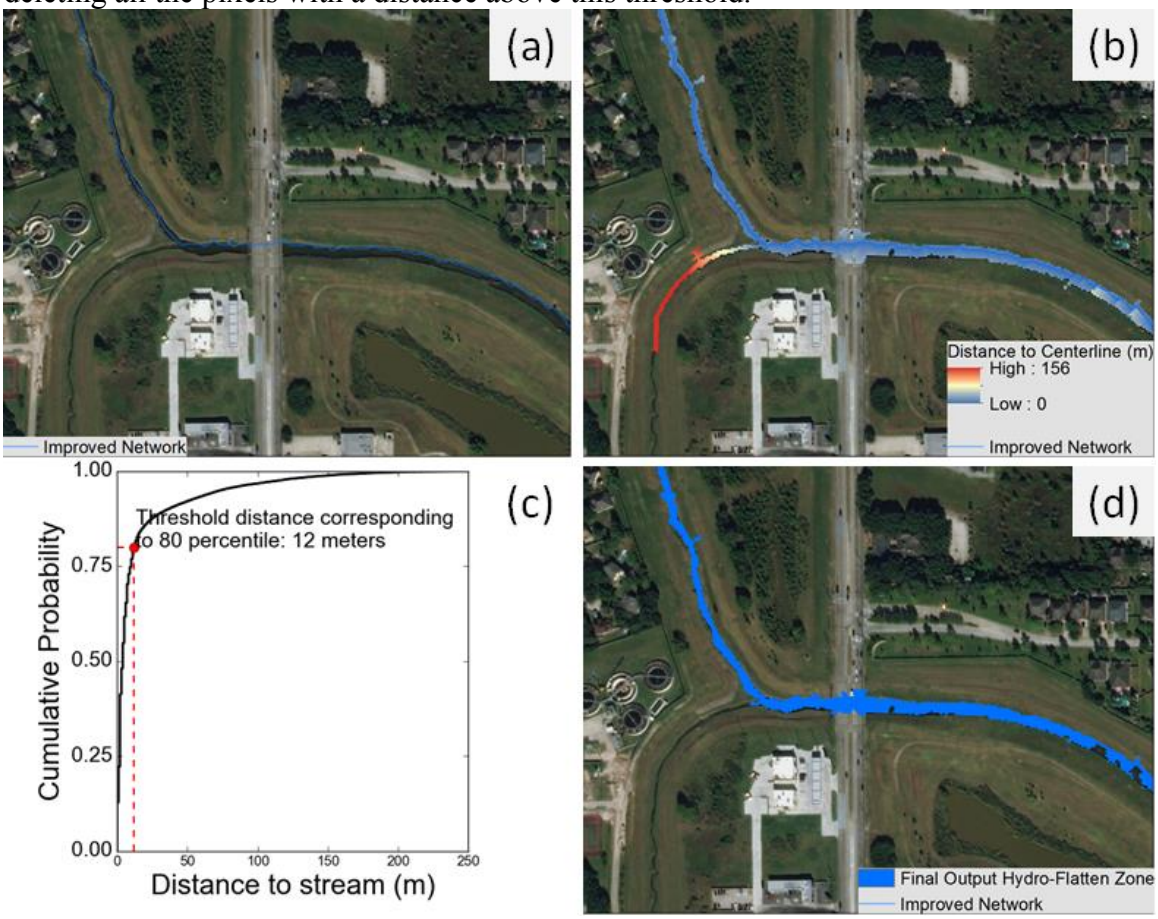

Figure 4.9: Hydro-flattened zone identification based on distance to centerline information: (a) extracted channel centerline connected with a small tributary; (b) distance to the extracted centerline of the identified positive-curvature pixels; (c) hydro-flattened zone distance threshold identification based on the probability distribution; (d) final extracted hydro-flattened output after all the pixels with a distance to the centerline greater than the threshold have been removed.

Finally, the raster composed of all the identified pixels is converted to a hydro-flattened polygon.

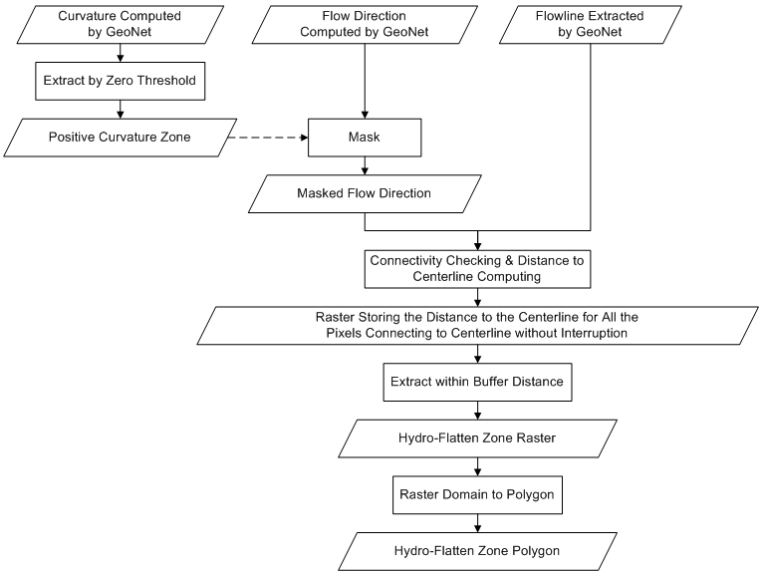

Figure 4.10: Flowchart for the hydro-flattened zone extraction identification.

4.4.2.4 Raster-based channel zone extraction and bankfull width estimation

A challenge associated with the transect-based approach used in the original GeoNet workflow for bank detection is that different transect lengths may need to be defined for different order streams. Therefore, we propose a raster-based method for solving the bank extraction problem (Figure 4.11). To extract the geomorphic channel zone, we rely on the slope information, similarly to the original GeoNet bank detection routine. It is assumed in the original routine that the bank points along a cross section should be the location with the maximum slope on both sides of the detected centerline. We introduce a filter based on the statistical analysis of the slope distribution. Since bank locations correspond to the maximum peaks of the slope along the transect, these bankline pixels are preserved after the filtering operation. The only part within the

channel that is not in this zone is the convergent section at the center where the slope is close or equal to zero. Therefore, we compensate the missing central section using the hydro-flattened zone we identified in the previous step so that the entire channel zone is selected during the bank detection process. Finally, the raster with all the selected cells is converted into a polygon, and only polygons intersecting the centerlines are kept while the others are deleted. The bankfull width of each river is computed as the channel zone area divided by the length of the centerline.

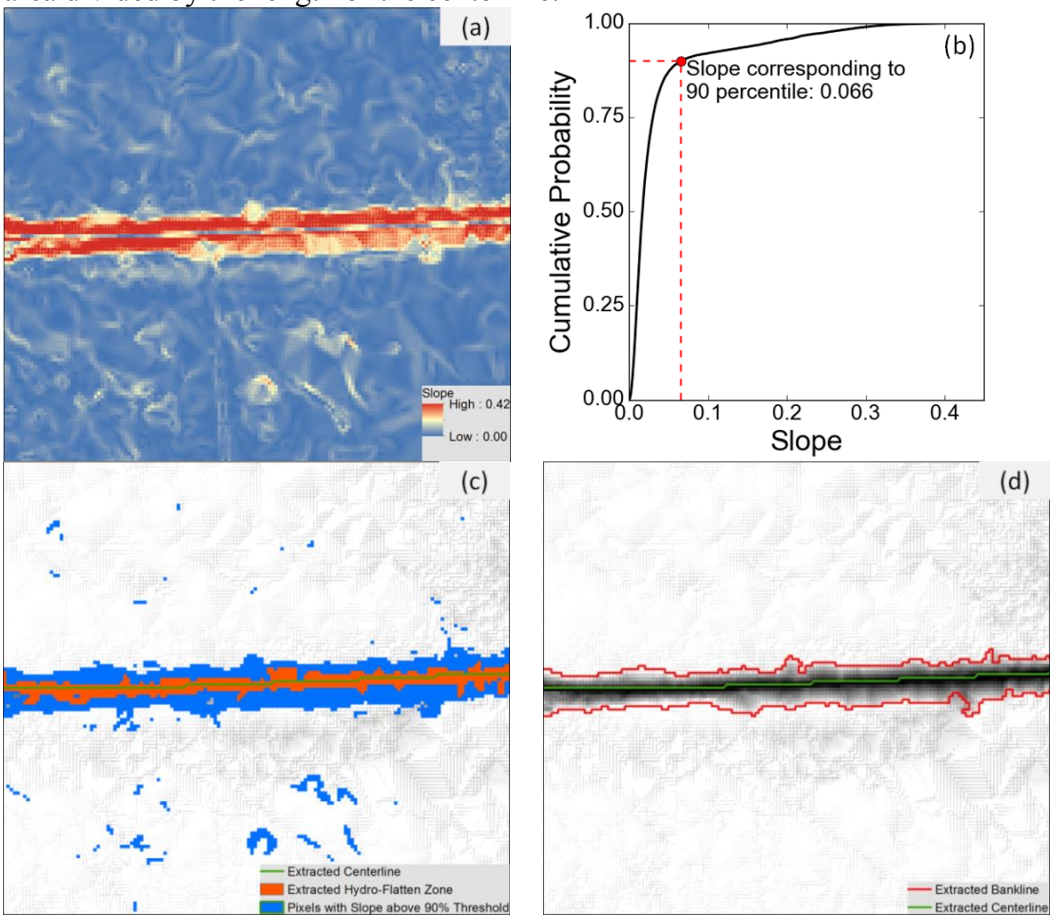

Figure 4.11: Channel zone identification based on slope: (a) slope raster at a given site; (b)channel zone slope threshold identification based on the cumulative distribution function; (c) hydro-flattened zone overlapped with the pixels above the slope threshold covering the entire channel domain; (d) final bankline output.

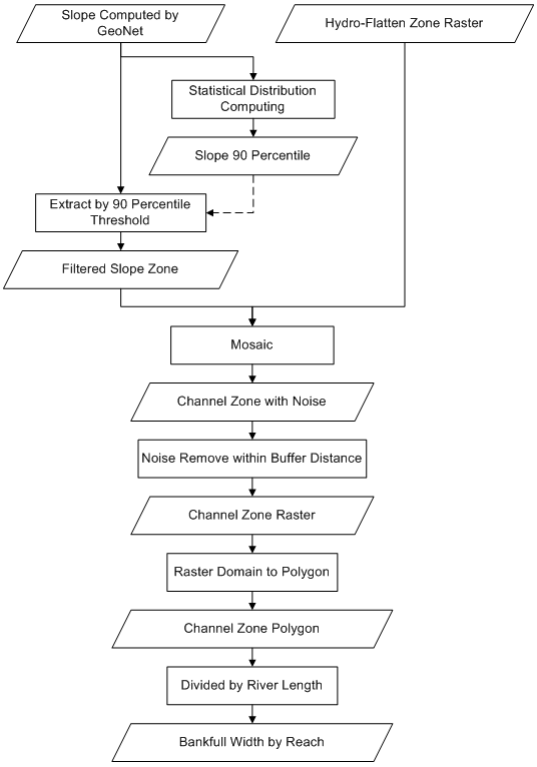

Figure 4.12: Flowchart for the channel extraction and reach-average bankfull width calculation part.

4.5 RESULTS

4.5.1 Natural basin

First, the river centerline network is extracted using the method described in section 4.4.2.2. The comparison (Figure 4.13) between our extracted river network and the original NHD one shows that our results align up better with the high-resolution terrain data (Figure 4.13.b) and satellite imagery (Figure 4.13.c).

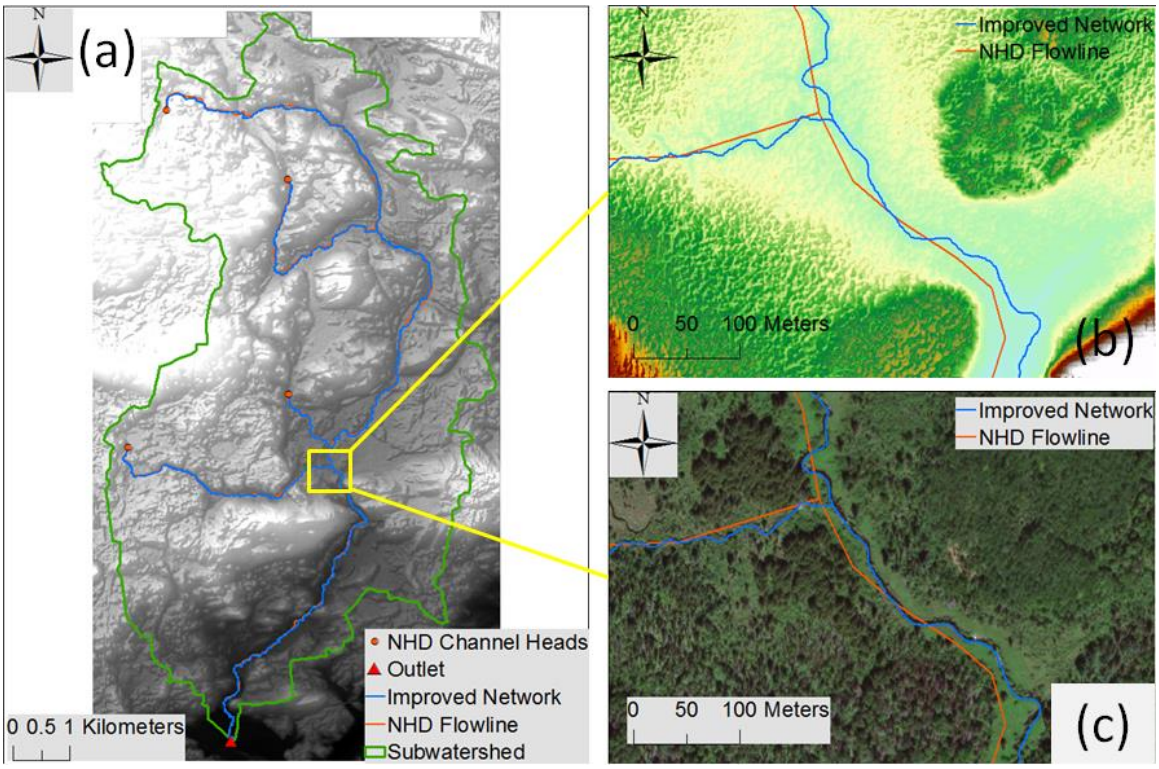

Figure 4.13: Comparison between the extracted river network and NHD river network in a natural basin, East Branch Sturgeon River Subwatershed, MI: (a) entire subwatershed; (b) zoom-in view at a location with lidar-derived terrain as background; (c) zoom-in view with satellite imagery as background.

The hydro-flattened zone is then extracted based on the curvature and connectivity analysis. A problem found during this operation is the clipping distance threshold identification: our method is able to capture the waterbodies that the channels intersect. Since the width of the waterbodies is usually large (Figure 4.14) compared to the channel width, we need to set a relative large distance threshold during the clipping process to keep these waterbodies in our final results. On the other hand, a small distance threshold is needed to remove convergent terrain portions that are not part of the network. Here, since we are interested in the hydro-flatten zone correspondence of the river network, we use a small threshold (Figure 4.15). The underestimation at waterbodies can

be accounted for by masking the initial output with a buffer of the NHD waterbody features before the clipping, and then apply the filter only to the unmasked zone.

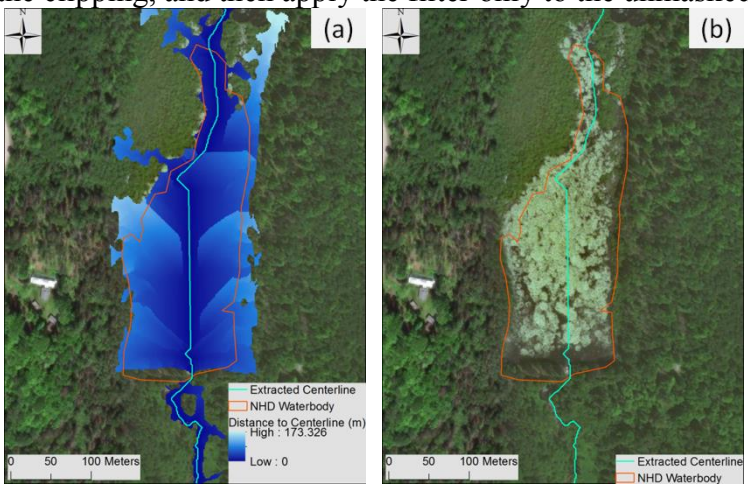

Figure 4.14: Distance to centerline at a waterbody: (a) Raster output; (b) Reference satellite imagery.

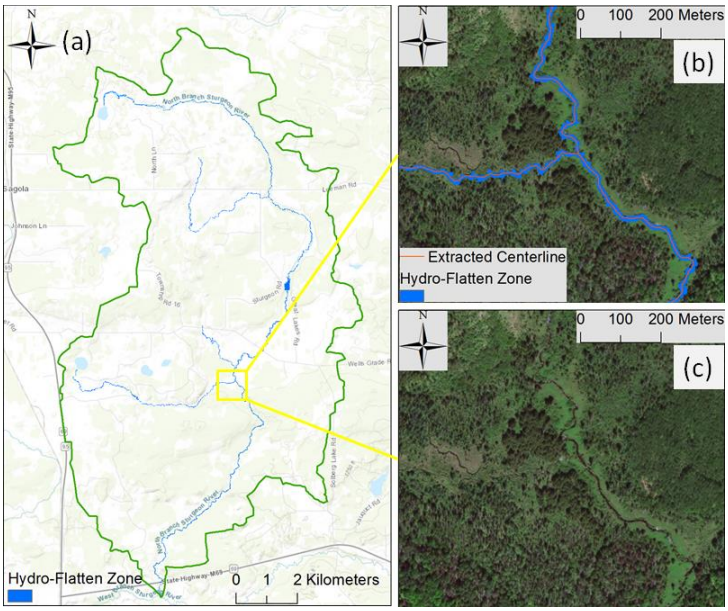

Figure 4.15: Hydro-flattened zone extracted for the natural basin, East Branch Sturgeon River Subwatershed, MI: (a) results for the entire subwatershed; (b) zoom-in view of the output; (c) zoom-in view satellite imagery as the reference.

Because the channels in this watershed are all small head water streams, we found that the hydro-flattened zone mostly coincides with the geomorphic channel zone. Therefore, we converted the extracted hydro-flattened zone into polygons and computed the corresponding bankfull width for each river (Figure 4.16).

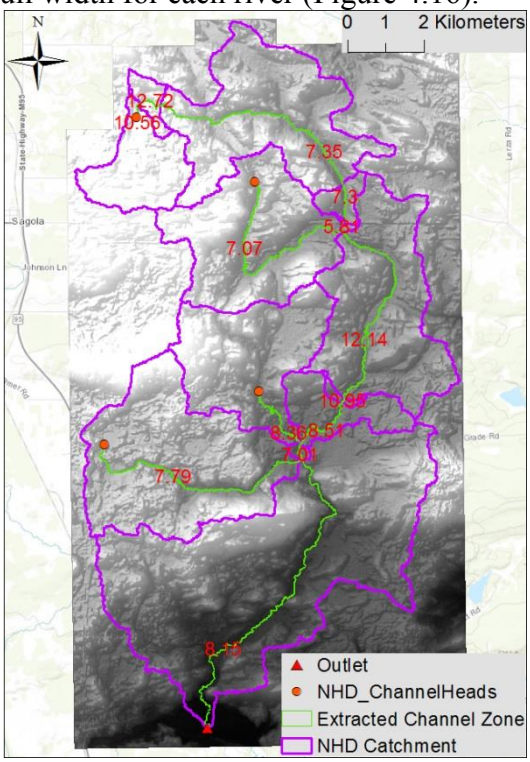

Figure 4.16: Extracted channel zone and estimated reach-average bankfull width in the natural basin, East Branch Sturgeon River Subwatershed, MI.

4.5.2 Agricultural basin

The agricultural basin test shows similar improvements in the extracted river network (Figure 4.17).

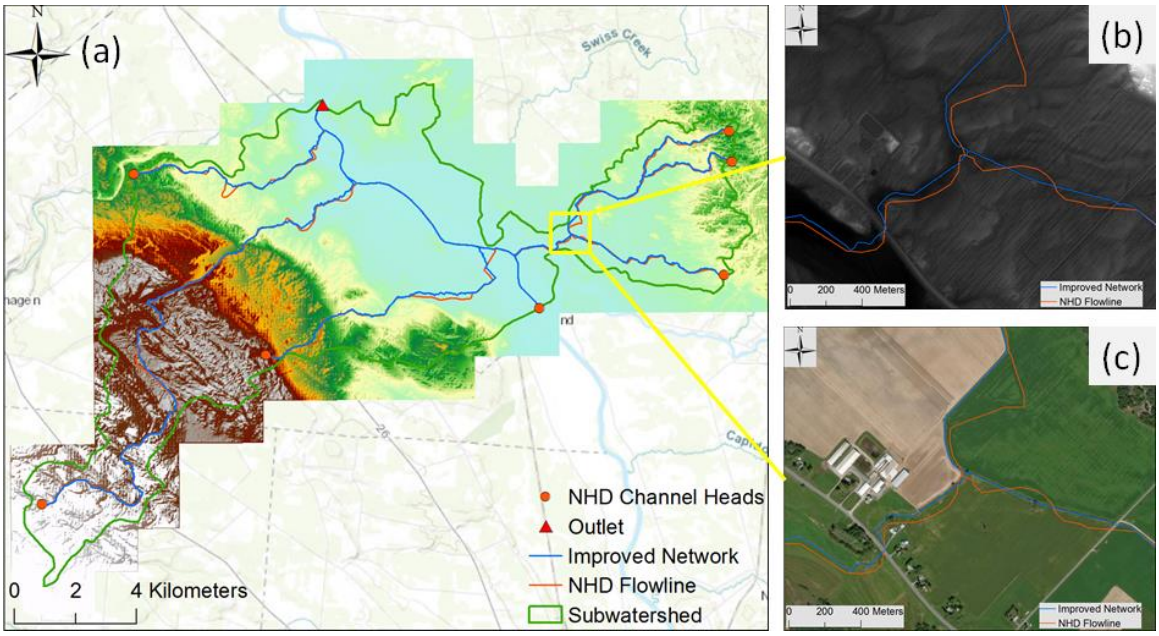

Figure 4.17: Comparison between the extracted river network and NHD river network in an agricultural basin, Stony Creek-Black River Subwatershed, NY: (a) results for the entire subwatershed; (b) zoom-in view at a location with lidar-derived terrain as background; (c) zoom-in view with satellite imagery as background.

Since there are hundred-meter-wide main stem rivers and several-meter-wide artificial canals, we implemented the clipping process by catchment with a unique threshold identified from the distance statistic distribution of each local catchment (Figure 4.18).

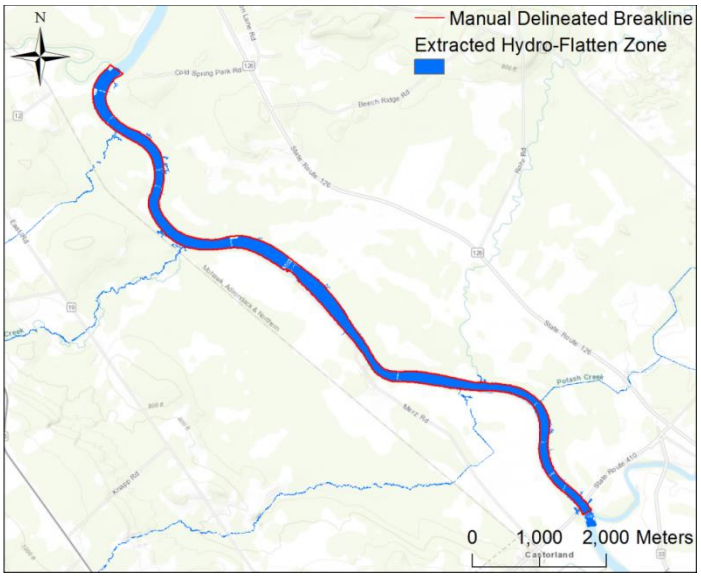

Figure 4.18: Hydro-flattened zone extracted for the agricultural basin, Stony Creek-Black River Subwatershed, NY, with manually delineated breaklines as the reference.

In this basin, the hydro-flattened zone also overlaps with the geomorphic channel zone. Therefore, we computed the reach-average bankfull width based on the extracted hydro-flattened zone (Figure 4.19).

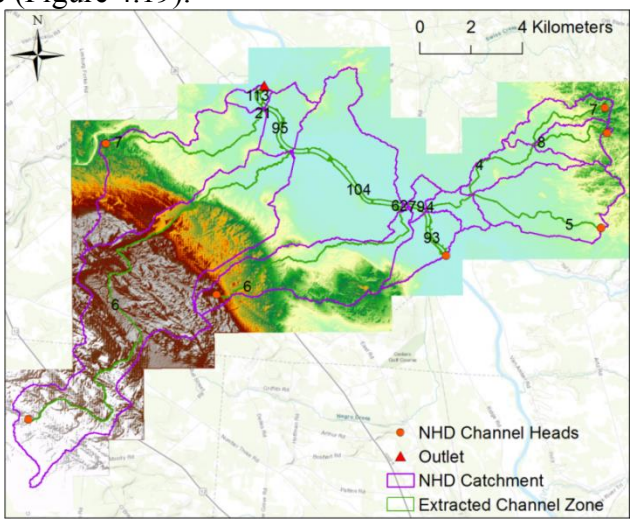

Figure 4.19: Extracted channel zone and estimated bankfull width in the agricultural basin, Stony Creek-Black River subwatershed, NY.

4.5.3 Urban basin

Since this is an urbanized flat area, we adopted the Laplacian curvature to favor the extraction of natural channels (Passalacqua et al., 2012). The results show an improved accuracy of the extracted network (Figure 4.20).

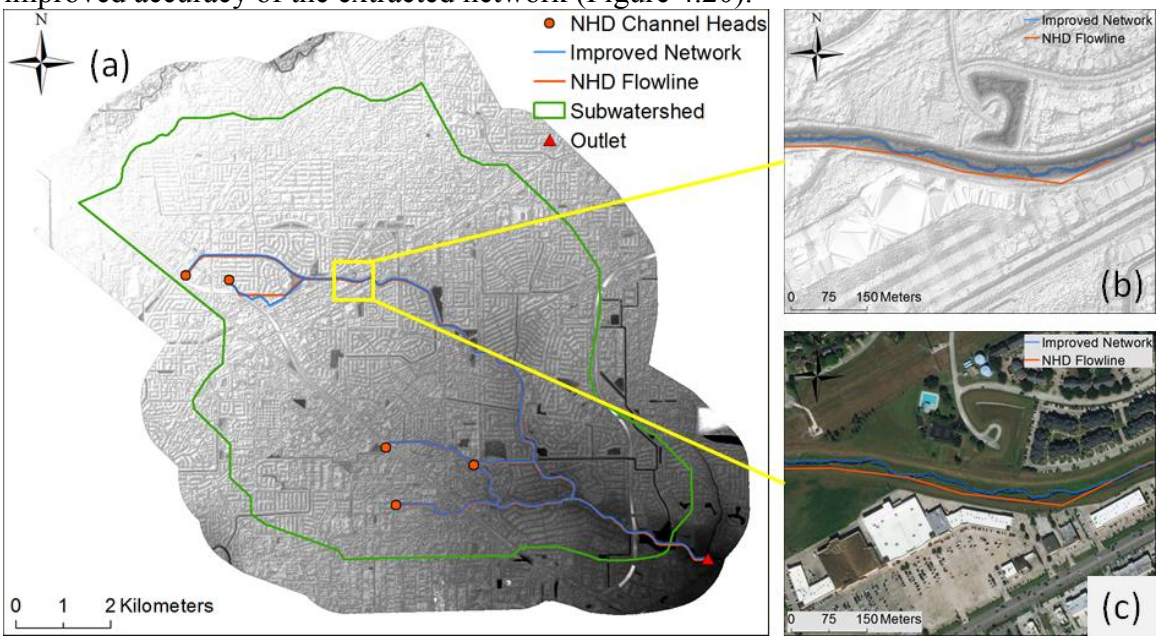

Figure 4.20: Comparison between the extracted river network and NHD river network in an urbanized basin, Jersey Lake-Whiteoak Bayou subwatershed, TX: (a) results for the entire subwatershed; (b) zoom-in view at a location with lidar-derived terrain as background; (c) zoom-in view with satellite imagery as background.

We identified problematic area in the upper left corner of the watershed, where a ditch was extracted as part of the original network, but was not detectable in the terrain input (Figure 4.21). Therefore, our tool traced an arbitrary path from the given channel head to the main stem river.

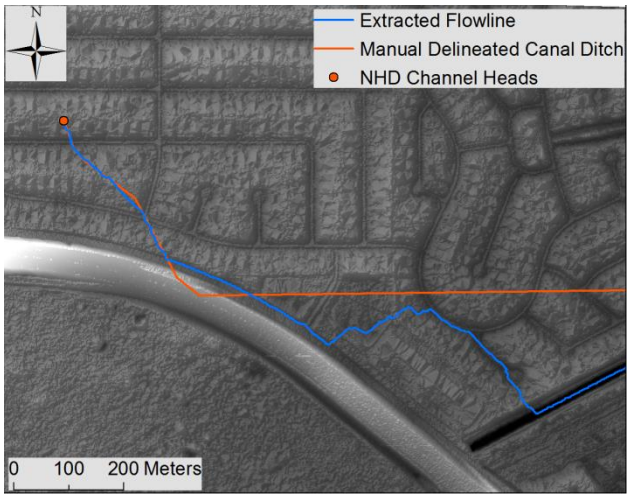

Figure 4.21: Canal ditch in NHD river network not detectable in the terrain data.

The hydro-flattened zone extracted automatically with our proposed method is able to capture the majority of the manually delineated extent (Figure 4.22).

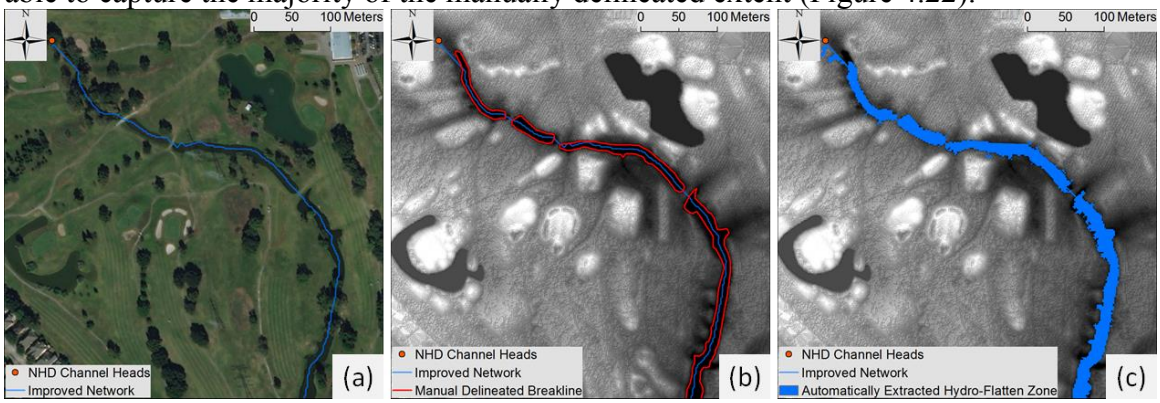

Figure 4.22: Hydro-flattened zone extracted for the urban basin, Jersey Lake-Whiteoak Bayou subwatershed, TX: (a) reference satellite imagery; (b) reference manually delineated breakline; (c) automatically extracted hydro-flattened zone.

Differently from the two previous areas, here water only occupies a small portion of the channel cross section for most of the time. Therefore, we used the slope information as described in section 4.4.2.4 to obtain the final geomorphic channel zone (Figure 4.23).

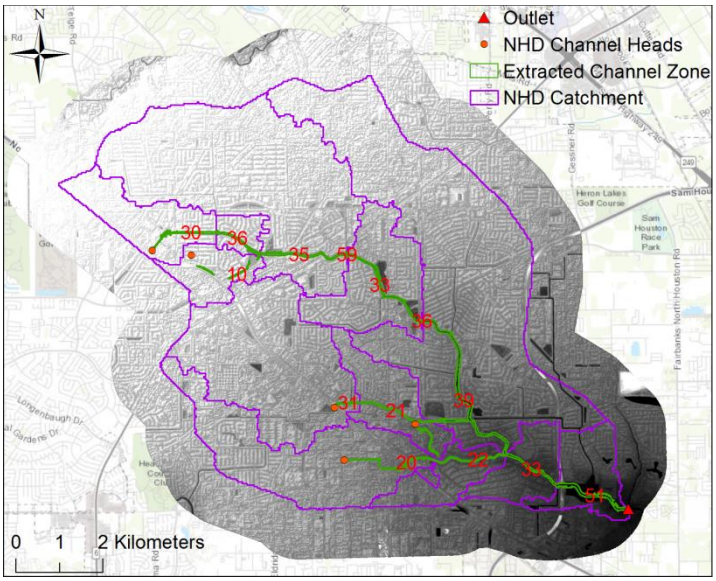

Figure 4.23: Extracted channel zone and estimated bankfull width in the urban basin, Jersey Lake-Whiteoak Bayou subwatershed, TX.

4.6 CONCLUSIONS

In this paper, we presented modifications and new modules of GeoNet, a tool designed for automatic feature extraction from high-resolution topography. The new modules allow to automatically hydro-flatten elevation data. The form of the geodesic cost function used for river network tracing was modified to include information of the existing river network features and to correct the potential errors in the accumulation area term. Once the river centerline network is extracted, curvature and connectivity to centerline information are used to identify the convergent sections of the terrain. A threshold obtained from statistical analysis of horizontal distance to stream is applied to filter unwanted components. Combining the hydro-flattened output with slope information, we obtain the geomorphic channel zone of a river network, and compute the reach-average bankfull width for every river segment in the network, providing critical information to improve the performance of large-scale hydrological simulation and

inundation mapping. We tested our proposed workflow at three sites with natural, agricultural, and urban terrain settings. Compared to satellite imagery and approved manual products, our results demonstrate competitive accuracy, showing that our method can automatically perform hydro-flattening and bank detection identification. The results also show that at some sites, the hydro-flattened zone can be directly used for the bankfull width calculation without using slope information.

Chapter 5: Conclusions

5.1 Answer to the Research Questions

Three research questions were posed at the beginning of this dissertation to guide and organize the research presented. These questions are interrelated and progressive. Though developing strategies to answer each of these questions, we understand different aspects of the complicated continental scale river geometry and inundation map subject, and gain a comprehensive view of this very big picture. A succinct summary of the answer to each question is presented and discussed below.

1. *How to combine the products with a national high-resolution real-time stream discharge forecast system to generate a high-resolution river geometry data set and a real-time flood inundation mapping system with continental coverage based on hydrologic terrain analyses?*

Based on the findings of the presented research, we treat the HAND raster as the bridge to close the gaps among continental hydrology, continental hydraulics and continental inundation mapping. We have shown how HAND can be used for multiple purposes following the methods we have developed: first, river geometry information, an essential kind of input needed to drive large-scale hydrodynamic simulation, can be derived from HAND; second, substituting HAND-derived the river geometry information into the Manning's equation provides reach-average synthetic rating curves as an approximate solution to realize the conversion from discharge provided by large-scale hydrologic simulation to stage needed by large-scale inundation mapping; third, after the stage information is obtained, either through hydrodynamic simulation or synthetic rating curves, HAND can be used to create inundation extents corresponding to the given water depth; forth, when the HAND value of each address point is estimated, the flood impact

can be directly evaluated from the stage information without the need of generating inundation extent polygons, which shortens the cycle of flood impact assessment and improves the efficiency of emergency response.

2. *When we substitute low-resolution terrain inputs with lidar-derived high-resolution topographic information during our river geometry estimation and approximate inundation mapping practice, what kinds of change do we need to introduce to the workflow? Does the improvement in terrain inputs accuracy generally result in the improvement in river geometry and inundation extent outputs accuracy?*

Through our study, we have demonstrated that the workflow designed for solving research question 1 with low-resolution terrain inputs has to be modified to address the additional challenges brought by lidar-derived inputs. GeoNet, which traces the channel centerline as the geodesic optimal path from the channel head to the outlet based on a cost function made up by curvature and accumulation terms, should be included as a part of the framework. Therefore, we couple the HAND method presented previously with GeoNet as a more comprehensive method called GeoFlood. Through analyzing the results of our test, we find out that the adoption of more detailed topographic inputs in a natural watershed does not necessarily mean significant improvement of accuracy in the predicted inundation extent. Part of this is due to the averaging effect of low-resolution data, part is due to the apparent gradient of the landscape, and part is due to the limitation in the mechanism of our approximate inundation mapping strategy. Therefore, the value of high-resolution topographic information lies more on predicting more precise local water depths, generating more accurate extent in flat areas and supporting more detailed hydrodynamic simulations.

3. *How can we automatically extract the channel zone for a large-scale river network from lidar-derived high-resolution terrain dataset? Does the workflow apply in different geomorphic settings?*

We present how the GeoNet tool has been modified and extended to extract the channel zone and estimate the reach-average bankfull width. Terrain attributes derived from the DEM including slope, curvature, accumulation, connectivity, and distance to centerline, provides beneficial indication on where the river centerline is and where the main channel separates from the floodplain. We also demonstrate how prior knowledge contained from low-resolution products can facilitate the feature automatic extraction from high-resolution terrain dataset. We have tested our method in different geomorphic circumstances and the comparison versus approved ground truth validates the feasibility of our approach.

5.2 CONTRIBUTION TO SCIENCE AND TECHNOLOGY

From a philosophical point of view, these are the insights we gain from the presented study:

1. Get 90% correct is easy, but get 100% correct is hard.
2. When we are trying to solve an extremely complicated problem with no information given, starting with a bold assumption that at least can simplify the problem to a feasible level. Sometimes it can still give you useful information and usable products.
3. The more doesn't necessarily mean the better. When the schema of a model or the structure of a system is simplified, adding extra information in the input may not result in gains in the output.

4. When exploring new knowledge, starting from what you already have is better than starting from scratch.
5. Balance is important. Specifically in our context, it refers to the balance between local and global and the balance between different terms in the cost function.
6. No matter how advanced a method is, it couldn't capture the truth not stored in the input.

From a scientific point of view, these are the knowledge we learn from the presented study:

1. Terrain is the essential factor that accounts for where water goes during flood events, but is not the whole story. Rely solely on terrain information can reproduce the majority of the actual inundation scenario, but there always are some missing parts where advanced hydraulic study comes into place.
2. Problems are found when the national hydrological framework, namely NHD, is directly adopted in hydraulic simulation and inundation mapping practice. Therefore, it needs to be subdivided into regular intervals of length of the order of 1 km to obtain robust reach-average channel properties and synthetic rating curves.
3. Great uncertainties come together with the roughness coefficient of the river. Calibration on the Manning's n must be conducted if the best performance is expected under the one-dimensional steady flow assumption.
4. When the channel extraction task is conducted with GeoNet, the size of the computation domain needs to be carefully selected. Running the tool

individually for each separate hydrological unit generates better results than running it with the entire area as a whole.

From an engineering point of view, these are the products we obtain from the presented study:

1. A continental-scale inundation mapping framework prototype that has been adopted by the National Water Center.
2. An automatic workflow with associated various terrain analysis tools that rapidly convert large-scale discharge forecast into corresponding regional or national approximate inundation maps in hours or minutes, the feasibility of which has been tested during extreme flood events in the real world.
3. A channel property and synthetic rating curve database for the continental-scale river network with millions of reach segments.
4. A set of methods and tools to validate the estimated channel properties, rating curves, and inundation extents versus ground truths.
5. A new version of the GeoNet tool which generates better results and owns more capability such as hydro-flattening and bank detection.

5.3 RECOMMENDATION FOR FUTURE WORK

In summary, the following recommendations are made to drive future research:

Continental-scale River Geometry and Inundation Mapping using Low-Resolution Terrain Data:

1. An operational real-time inundation mapping system should be established using the products created throughout this research to meet the urgent needs of flood emergency response.

2. A more systematic way of estimating stable stream bed slope should be developed, since the slope is a critical term in the Manning's equation.
3. Validation of the HAND-derived river geometry and synthetic rating curves should be conducted at more sites with different geomorphic settings where observed ground truth is available.
4. A more comprehensive inundation map database should be established to store the actual inundation scenarios, which can be used to validate our simulation results.
5. Instead of having a constant drainage relationship, how the drainage pattern changes associated with different water levels is also a promising direction to explore.

Inundation mapping with lidar-derived high-resolution terrain dataset:

1. Better understand the effect of artificial structures by comparing the results generated with raw DEM and hydro-conditioned (burnt-in) DEM.
2. More tests should be conducted with GeoNet, and further development should be added where the current tool does not return satisfactory results.
3. A more comprehensive study in urban environment to compare the performance of terrain-based inundation mapping strategy and hydrodynamic simulation. Within the scope of terrain-based inundation mapping, the accuracy comparison should also be conducted between a bare-earth DEM input and a DEM input with all building footprints.
4. A method should be explored that estimates the land surface roughness information based on either raw lidar point clouds or lidar-derived terrain datasets.

Automatic hydro-flattening and channel zone extraction

1. A regional test should be set up to examine the performance of the proposed method at a large scale.
2. More tests should be conducted where observed ground truth is available.
3. The improvement brought by this bankfull width estimation strategy should be quantified through running large-scale hydrologic simulation with and without the channel zone information.

References

Ackerman, C. T. 2005. HEC-GeoRAS, GIS tools for support of HEC-RAS using ArcGIS. United States Army Corps of Engineers, Davis.

Acharjee, P. P. 2017. On feature extraction from large scale linear lidar data (Doctoral dissertation, The University of Texas at Arlington).

Alfieri, L., Salamon, P., Bianchi, A., Neal, J., Bates, P., and Feyen, L. 2014. Advances in pan-European flood hazard mapping. Hydrological Processes, 28(13), 4067-4077.

Allen, G. H. and Pavelsky, T. M. 2015. Patterns of river width and surface area revealed by the satellite-derived North American River Width data set. Geophysical Research Letters, 42(2), 395-402.

Andreadis, K. M., Schumann, G. J. P., and Pavelsky, T. M. 2013. A simple global river bankfull width and depth database. Water Resources Research, 49(10), 7164-7168.

Apel, H., Aronica, G. T., Kreibich, H., and Thieken, A. H. 2009. Flood risk analyses--how detailed do we need to be?. Natural Hazards, 49(1), 79-98.

Arge, L., Chase, J. S., Halpin, P., Toma, L., Vitter, J. S., Urban, D., and Wickremesinghe, R. 2003. Efficient flow computation on massive grid terrain datasets. GeoInformatica, 7(4), 283-313.

Afshari, S., Tavakoly, A. A., Rajib, M. A., Zheng, X., Follum, M. L., Omranian, E., and Fekete, B. M. 2018. Comparison of new generation low-complexity flood inundation mapping tools with a hydrodynamic model. Journal of Hydrology 556: 539-556.

Band, L. E. 1986. Topographic partition of watersheds with digital elevation models. Water Resources Research, 22(1), 15-24.

Barnes, R., Lehman, C., and Mulla, D. 2014. An efficient assignment of drainage direction over flat surfaces in raster digital elevation models. Computers & Geosciences, 62, 128-135.

Basso, B. 2005. Digital terrain analysis: Data source, resolution and application for modeling physical processes in agroecosystems. Rivista Italiana di Agrometeorologia, 2(5).

Bates, P. D., Horritt, M. S., Smith, C. N., and Mason, D. 1997. Integrating remote sensing observations of flood hydrology and hydraulic modelling. Hydrological Processes, 11(14), 1777-1795.

Bates, P. D. and De Roo, A. P. J. 2000. A simple raster-based model for flood inundation simulation. Journal of Hydrology, 236(1), 54-77.

Bates, P. D., Horritt, M. S., and Fewtrell, T. J. 2010. A simple inertial formulation of the shallow water equations for efficient two-dimensional flood inundation modelling. Journal of Hydrology, 387(1), 33-45.

Bates, P. D. 2012. Integrating remote sensing data with flood inundation models: how far have we got?. Hydrological Processes, 26(16), 2515-2521.

Brunner, G. W. 1997. HEC-RAS (River Analysis System). In North American Water and Environment Congress & Destructive Water (pp. 3782-3787). ASCE.

Callow, J. N., Van Niel, K. P., and Boggs, G. S. 2007. How does modifying a DEM to reflect known hydrology affect subsequent terrain analysis?. Journal of Hydrology, 332(1), 30-39.

Casas, A., Benito, G., Thorndycraft, V. R., and Rico, M. 2006. The topographic data source of digital terrain models as a key element in the accuracy of hydraulic flood modelling. Earth Surface Processes and Landforms, 31(4), 444-456.

Castellarin, A., Di Baldassarre, G., Bates, P. D., and Brath, A. 2009. Optimal cross-sectional spacing in Preissmann scheme 1D hydrodynamic models. Journal of Hydraulic Engineering, 135(2), 96-105.

Castro, J. M., and Jackson, P. L. 2001. Bankfull discharge recurrence intervals and regional hydraulic geometry relationships: Patterns in the Pacific Northwest, USA. Journal of the American Water Resources Association (JAWRA), 37(5), 1249-1262.

Chambenoit, Y., Classeau, N., Trouvé, E., and Rudant, J. P. 2003. Performance assessment of multitemporal SAR images' visual interpretation. Geoscience and Remote Sensing Symposium (IEEE International), 6, 3911-3913.

Chen, B., Krajewski, W. F., Goska, R., and Young, N. 2017. Using LiDAR surveys to document floods: A case study of the 2008 Iowa flood. Journal of Hydrology, 553, 338-349.

Chow, V. T. 1959. Open channel hydraulics. McGraw-Hill Book Company, Inc; New York.

Chust, G., Galparsoro, I., Borja, A., Franco, J., and Uriarte, A. 2008. Coastal and estuarine habitat mapping, using LIDAR height and intensity and multi-spectral imagery. Estuarine, Coastal and Shelf Science, 78(4), 633-643.

Clifton, W. E., Steele, B., Nelson, G., Truscott, A., Itzler, M., and Entwistle, M. 2015. Medium altitude airborne Geiger-mode mapping LIDAR system. Laser Radar Technology and Applications XX; and Atmospheric Propagation XII, 9465, 946506.

Costa-Cabral, M. C., and Burges, S. J. 1994. Digital elevation model networks (DEMON): A model of flow over hillslopes for computation of contributing and dispersal areas. Water Resources Research, 30(6), 1681-1692.

Cuartas, L. A., Tomasella, J., Nobre, A. D., Nobre, C. A., Hodnett, M. G., Waterloo, M. J., ... and Ferreira, M. 2012. Distributed hydrological modeling of a micro-scale rainforest watershed in Amazonia: Model evaluation and advances in calibration using the new HAND terrain model. Journal of Hydrology, 462, 15-27.

Cunge, J. A., Holly, F. M., and Verwey, A. 1980. Practical aspects of computational river hydraulics.

David, G. C., Wohl, E., Yochum, S. E., and Bledsoe, B. P. 2010. Controls on at-a-station hydraulic geometry in steep headwater streams, Colorado, USA. Earth Surface Processes and Landforms, 35(15), 1820-1837.

Deshmukh, K. S., and Shinde, G. N. 2005. An adaptive color image segmentation. Electronic Letters on Computer Vision and Image Analysis (ELCVIA), 5(4), 12-23.

Deshpande, S. S., and Yilmaz, A. 2017. A semi-automated method to create a lidar-based hydro-flattened DEM. International journal of remote sensing, 38(5), 1365-1387.

Di Baldassarre, G., and Montanari, A. 2009. Uncertainty in river discharge observations: a quantitative analysis. Hydrology and Earth System Sciences, 13(6), 913-921.

Dingman, S. L. 2007. Analytical derivation of at-a-station hydraulic–geometry relations. Journal of Hydrology, 334(1), 17-27.

Dixon, T. H., Amelung, F., Ferretti, A., Novali, F., Rocca, F., Dokka, R., ... and Whitman, D. 2006. Space geodesy: Subsidence and flooding in New Orleans. Nature, 441(7093), 587-588.

Dottori, F. 2012. Development of parallelizable flood inundation models for large scale analysis (Doctoral dissertation, alma).

Dottori, F., Salamon, P., Bianchi, A., Alfieri, L., Hirpa, F. A., and Feyen, L. 2016. Development and evaluation of a framework for global flood hazard mapping. Advances in Water Resources, 94, 87-102.

Doctor, D. H., and Young, J. A. 2013. An evaluation of automated GIS tools for delineating karst sinkholes and closed depressions from 1-meter LIDAR-derived digital elevation data.

Ehlschlaeger, C. 1989. Using the A^T search algorithm to develop hydrologic models from digital elevation data. International Geographic Information Systems (IGIS) symposium, 89, 275-281.

Fairfield, J., and Leymarie, P. 1991. Drainage networks from grid digital elevation models. Water Resources Research, 27(5), 709-717.

Fan, Y., Liu, Y., Wang, S., Tarboton, D., Yildirim, A., and Wilkins-Diehr, N. 2014. Accelerating TauDEM as a Scalable Hydrological Terrain Analysis Service on XSEDE. Annual Conference on Extreme Science and Engineering Discovery Environment, 5.

FEMA (2016), Flood insurance study: Travis County, Texas and incorporated areas, available online at <https://map1.msc.fema.gov/data/48/S/PDF/48453CV001C.pdf?LOC=0562fb8b0786d89f646b85e5f2a9b2fc >

Ferguson, R. I. 1986. Hydraulics and hydraulic geometry. Progress in Physical Geography, 10(1), 1-31.

Ferraz, A., Mallet, C., Chehata, N. 2016. Large-scale road detection in forested mountainous areas using airborne topographic lidar data. ISPRS Journal of Photogrammetry and Remote Sensing 112, 23-36.

Gallant, J. C. 2000. Terrain analysis: principles and applications. John Wiley & Sons.

Garambois, P. A., Calmant, S., Roux, H., Paris, A., Monnier, J., Finaud-Guyot, P., ... and Santos da Silva, J. 2017. Hydraulic visibility: Using satellite altimetry to parameterize a hydraulic model of an ungauged reach of a braided river. Hydrological Processes, 31(4), 756-767.

Garbrecht, J., and Martz, L. W. 1997. The assignment of drainage direction over flat surfaces in raster digital elevation models. Journal of Hydrology, 193(1), 204-213.

Gee, D. M., Anderson, M. G., and Baird, L. 1990. Large-scale floodplain modelling. Earth surface processes and landforms, 15(6), 513-523.

Gesch, D. B., Oimoen, M. J., and Evans, G. A. 2014. Accuracy assessment of the U.S. Geological Survey National Elevation Dataset, and comparison with other large-area elevation datasets—SRTM and ASTER. U.S. Geological Survey Open-File Report 2014, 1008, 10.

Getirana, A. C., Boone, A., Yamazaki, D., and Mognard, N. 2013. Automatic parameterization of a flow routing scheme driven by radar altimetry data: Evaluation in the Amazon basin. Water Resources Research, 49(1), 614-629.

Gleason, C. J., and Smith, L. C. 2014. Toward global mapping of river discharge using satellite images and at-many-stations hydraulic geometry. Proceedings of the National Academy of Sciences, 111(13), 4788-4791.

Gleason, C. J. 2015. Hydraulic geometry of natural rivers: A review and future directions. Progress in Physical Geography, 39(3), 337-360.

Grimaldi, S., Nardi, F., Di Benedetto, F., Istanbulluoglu, E., and Bras, R. L. 2007. A physically-based method for removing pits in digital elevation models. Advances in Water Resources, 30(10), 2151-2158.

Hallegatte, S., Green, C., Nicholls, R. J., and Corfee-Morlot, J. 2013. Future flood losses in major coastal cities. Nature climate change, 3(9), 802-806.

Harman, C., Stewardson, M., and DeRose, R. 2008. Variability and uncertainty in reach bankfull hydraulic geometry. Journal of Hydrology, 351(1), 13-25.

Hart, P. E., Nilsson, N. J., and Raphael, B. 1968. A formal basis for the heuristic determination of minimum cost paths. IEEE transactions on Systems Science and Cybernetics, 4(2), 100-107.

Hellweger, F., and Maidment, D. 1997. AGREE-DEM surface reconditioning system. University of Texas, Austin.

Herold, C., and Rudari, R. 2013. Improvement of the Global Flood Model for the GAR 2013 and 2015. United Nations Office for Disaster Risk Reduction (UNISDR): Geneva, Switzerland.

Hilldale, R. C., and Raff, D., 2008. Assessing the ability of airborne LiDAR to map river bathymetry. Earth Surface Processes and Landforms, 33(5), 773-783.

Hodges, B. R. 2013. Challenges in continental river dynamics. Environmental modelling and Software, 50, 16-20.

Höfle, B., Vetter, M., Pfeifer, N., Mandlburger, G., and Stötter, J. 2009. Water surface mapping from airborne laser scanning using signal intensity and elevation data. Earth Surface Processes and Landforms, 34(12), 1635-1649.

Hohenthal, J., Alho, P., Hyyppä, J., and Hyyppä, H. 2011. Laser scanning applications in fluvial studies. Progress in Physical Geography, 35(6), 782-809.

Hood, W. G. 2002. Landscape allometry: from tidal channel hydraulic geometry to benthic ecology. Canadian Journal of Fisheries and Aquatic Sciences, 59(8), 1418-1427.

Horritt, M. S., and Bates, P. D. 2001. Predicting floodplain inundation: raster-based modelling versus the finite-element approach. Hydrological Processes, 15(5), 825-842.

Horritt, M. S., and Bates, P. D. 2001. Effects of spatial resolution on a raster based model of flood flow. Journal of Hydrology, 253(1), 239-249.

Horritt, M. S., Di Baldassarre, G., Bates, P. D., and Brath, A. 2007. Comparing the performance of a 2-D finite element and a 2-D finite volume model of floodplain inundation using airborne SAR imagery. Hydrological Processes, 21(20), 2745-2759.

Hudak, A. T., Evans, J. S., and Stuart Smith, A. M., 2009. LiDAR utility for natural resource managers. Remote Sensing, 1(4), 934-951.

Hunter, N. M., Horritt, M. S., Bates, P. D., Wilson, M. D., and Werner, M. G. 2005. An adaptive time step solution for raster-based storage cell modelling of floodplain inundation. Advances in Water Resources, 28(9), 975-991.

Jenson, S. K. 1991. Applications of hydrologic information automatically extracted from digital elevation models. Hydrological processes, 5(1), 31-44.

Jenson, S. K., and Domingue, J. O. 1988. Extracting topographic structure from digital elevation data for geographic information system analysis. Photogrammetric engineering and remote sensing, 54(11), 1593-1600.

Johnson, P. A., and Fecko, B. J. 2008. Regional channel geometry equations: a statistical comparison for physiographic provinces in the eastern US. River Research and Applications, 24(6), 823-834.

Jowett, I. G. 1998. Hydraulic geometry of New Zealand rivers and its use as a preliminary method of habitat assessment. Regulated Rivers: Research & Management, 14(5), 451-466.

Johansen, K., Tiede, D., Blaschke, T., Arroyo, L. A., and Phinn, S. 2011. Automatic geographic object based mapping of streambed and riparian zone extent from LiDAR data in a temperate rural urban environment, Australia. Remote Sensing, 3(6), 1139-1156.

Johansen, K., Grove, J., Denham, R., and Phinn, S. R. 2013. Assessing stream bank condition using airborne LiDAR and high spatial resolution image data in temperate semirural areas in Victoria, Australia. Journal of Applied Remote Sensing, 7(1), 073492.

Johnson, J. M, Coll, J. M. et al. 2017. National Water Centers Innovators Program Summer Institute Report. Consortium of Universities for the Advancement of Hydrologic Science, Inc. Technical Report No 14.

Kinner, D., Mitasova, H., Harmon, R. S., Toma, L., and Stallard, R. 2005. GIS-based stream network analysis for the Chagres River Basin, Republic of Panama. The Rio Chagres: A Multidisciplinary Profile of a Tropical Watershed, Springer/Kluwer, 83-95.

Knighton, A. D. 1974. Variation in width-discharge relation and some implications for hydraulic geometry. Geological Society of America Bulletin, 85(7), 1069-1076.

Knighton, A. D. 1975. Variations in at-a-station hydraulic geometry. American Journal of Science, 275(2), 186-218.

Knox, J. C. 1993. Large increases in flood magnitude in response to modest changes in climate. Nature, 361(6411), 430-432.

Lashermes, B., Foufoula-Georgiou, E., and Dietrich, W. E. 2007. Channel network extraction from high resolution topography using wavelets. Geophysical Research Letters, 34(23), 4.

Leopold, L. B., and Maddock Jr, T. 1953. The hydraulic geometry of stream channels and some physiographic implications.

Leskens J. G., Brugnach, M., Hoekstra, A. Y., and Schuurmans, W. 2014. Why are decisions in flood disaster management so poorly supported by information from flood models?, Environmental modelling and Software, 53, 53–61.

Liu, F., and Hodges, B. R. 2014. Applying microprocessor analysis methods to river network modelling. Environmental Modelling and Software 52: 234-252.

Liu, H., Sherman, D., and Gu, S. 2007. Automated extraction of shorelines from airborne light detection and ranging data and accuracy assessment based on Monte Carlo simulation. Journal of Coastal Research, 1359-1369.

Liu, Y. Y., Maidment, D. R., Tarboton, D. G., Zheng, X., and Wang, S. 2018. A CyberGIS Integration and Computation Framework for High-Resolution Continental-Scale Flood Inundation Mapping. Journal of the American Water Resources Association (JAWRA), Draft for review.

Lynch, C. 2008. Big data: How do your data grow?. Nature, 455(7209), 28-29.

Lyon, S. W., Nathanson, M., Lam, N., Dahlke, H. E., Rutzinger, M., Kean, J. W., and Laudon, H. 2015. Can low-resolution airborne laser scanning data be used to model stream rating curves?. Water, 7(4), 1324-1339.

Magnusson, J., Jonas, T., and Kirchner, J. W. 2012. Temperature dynamics of a proglacial stream: Identifying dominant energy balance components and inferring spatially integrated hydraulic geometry. Water Resources Research, 48(6).

Maidment, D. R. 1992. Handbook of hydrology. McGraw-Hill, New York.

Maidment, D. R. 1996. GIS and hydrologic modeling-an assessment of progress. In Third International Conference on GIS and Environmental Modeling, Santa Fe, New Mexico.

Maidment, D. R., and Djokic, D. 2000. Hydrologic and hydraulic modeling support: With geographic information systems. ESRI, Inc..

Maidment, D. R. 2002. Arc Hydro: GIS for water resources (Vol. 1). ESRI, Inc..

Maidment, D. R. 2017. Conceptual framework for the national flood interoperability experiment. Journal of the American Water Resources Association (JAWRA), 53(2), 245-257.

Mason, D. C., Bates, P. D., and Dall'Amico, J. T. 2009. Calibration of uncertain flood inundation models using remotely sensed water levels. Journal of Hydrology, 368(1), 224-236.

McNamara, J. P., Ziegler, A. D., Wood, S. H., and Vogler, J. B. 2006. Channel head locations with respect to geomorphologic thresholds derived from a digital elevation model: A case study in northern Thailand. Forest Ecology and Management, 224(1), 147-156.

Merwade, V. M., Maidment, D. R., and Hodges, B. R. 2005. Geospatial representation of river channels. Journal of Hydrologic Engineering, 10(3), 243-251.

Merwade, V. M., Maidment, D. R., and Goff, J. A. 2006. Anisotropic considerations while interpolating river channel bathymetry. Journal of Hydrology, 331(3), 731-741.

Merwade, V., Cook, A., and Coonrod, J. 2008. GIS techniques for creating river terrain models for hydrodynamic modeling and flood inundation mapping. Environmental Modelling and Software, 23(10), 1300-1311.

Merz, B., Thieken, A. H., and Gocht, M. 2007. Flood risk mapping at the local scale: concepts and challenges. In Flood risk management in Europe, 231-251. Springer Netherlands.

Metz, M., Mitasova, H., and Harmon, R. S. 2011. Efficient extraction of drainage networks from massive, radar-based elevation models with least cost path search. Hydrology and Earth System Sciences, 15(2), 667-678.

Milly, P. C. D., Wetherald, R. T., Dunne, K. A., and Delworth, T. L. 2002. Increasing risk of great floods in a changing climate. Nature, 415(6871), 514-517.

Moore, I. D., Grayson, R. B., and Ladson, A. R. 1991. Digital terrain modelling: a review of hydrological, geomorphological, and biological applications. Hydrological processes, 5(1), 3-30.

Mosley, M. P. 1981. Semi-determinate hydraulic geometry of river channels, South Island, New Zealand. Earth surface processes and landforms, 6(2), 127-137.

Mulvihill, C. I., and Baldigo, B. P. 2012. Optimizing Bankfull Discharge and Hydraulic Geometry Relations for Streams in New York State. Journal of the American Water Resources Association(JAWRA), 48(3), 449-463.

National Research Council (NRC). 2009. Mapping the Zone: Improving Flood Map Accuracy. National Academies Press, Washington, D.C.

Neal, J., Schumann, G., and Bates, P. D. 2012. A subgrid channel model for simulating river hydraulics and floodplain inundation over large and data sparse areas. Water Resources Research, 48(11).

Neteler, M., and Mitasova, H. 2013. Open source GIS: a GRASS GIS approach (Vol. 689). Springer Science & Business Media.

Nicholls, R. J. 1995. Coastal megacities and climate change. GeoJournal, 37(3), 369-379.

Noji, E. K. 1991. Natural disasters. Critical care clinics, 7(2), 271-292.

Nobre, A. D., Cuartas, L. A., Hodnett, M., Rennó, C. D., Rodrigues, G., Silveira, A., ... and Saleska, S. 2011. Height above the nearest drainage-a hydrologically relevant new terrain model. Journal of Hydrology, 404(1), 13-29.

Nobre, A. D., Cuartas, L. A., Momo, M. R., Severo, D. L., Pinheiro, A., and Nobre, C. A. 2016. HAND contour: A new proxy predictor of inundation extent. Hydrological Processes, 30(2), 320-333.

Notebaert, B., Verstraeten, G., Govers, G., and Poesen, J. 2009. Qualitative and quantitative applications of LiDAR imagery in fluvial geomorphology. Earth Surface Processes and Landforms, 34(2), 217-231.

O'Callaghan, J. F., and Mark, D. M. 1984. The extraction of drainage networks from digital elevation data. Computer vision, graphics, and image processing, 28(3), 323-344.

Ohl, C. A., and Tapsell, S. 2000. Flooding and human health: the dangers posed are not always obvious. British Medical Journal, 321(7270), 1167-1167.

O'Loughlin, F., Trigg, M. A., Schumann, G. P., and Bates, P. D. 2013. Hydraulic characterization of the middle reach of the Congo River. Water Resources Research, 49(8), 5059-5070.

Orlandini, S., Tarolli, P., Moretti, G., and Dalla Fontana, G. 2011. On the prediction of channel heads in a complex alpine terrain using gridded elevation data. Water Resources Research, 47(2).

Paris, A., Dias de Paiva, R., Santos da Silva, J., Medeiros Moreira, D., Calmant, S., Garambois, P. A., ... and Seyler, F. 2016. Stage-discharge rating curves based on satellite altimetry and modeled discharge in the Amazon basin. Water Resources Research, 52(5), 3787-3814.

Park, C. C. 1977. World-wide variations in hydraulic geometry exponents of stream channels: an analysis and some observations. Journal of Hydrology, 33(1), 133-146.

Passalacqua, P., Do Trung, T., Foufoula-Georgiou, E., Sapiro, G., and Dietrich, W. E. 2010a. A geometric framework for channel network extraction from lidar: Nonlinear diffusion and geodesic paths. Journal of Geophysical Research: Earth Surface, 115(F1).

Passalacqua, P., Tarolli, P., and Foufoula-Georgiou, E. 2010b. Testing space-scale methodologies for automatic geomorphic feature extraction from lidar in a complex mountainous landscape. Water Resources Research, 46(11).

Passalacqua, P., Belmont, P., and Foufoula-Georgiou, E. 2012. Automatic geomorphic feature extraction from lidar in flat and engineered landscapes. Water Resources Research, 48(3).

Passalacqua, P., Belmont, P., Staley, D. M., Simley, J. D., Arrowsmith, J. R., Bode, C. A., Crosby, C., DeLong, S. B., Glenn, N. F., Kelly, S. A., et al. 2015. Analyzing high resolution topography for advancing the understanding of mass and energy transfer through landscapes: A review. Earth-Science Reviews, 148, 174–193.

Pavelsky, T. M., and Smith, L. C. 2008. RivWidth: A software tool for the calculation of river widths from remotely sensed imagery. IEEE Geoscience and Remote Sensing Letters, 5(1), 70-73.

Pelletier, J. D. 2013. A robust, two-parameter method for the extraction of drainage networks from high-resolution digital elevation models (dems): Evaluation using synthetic and real-world dems. Water Resources Research, 49 (1), 75–89.

Perona, P., and Malik, J. 1990. Scale-space and edge detection using anisotropic diffusion. IEEE Transactions on pattern analysis and machine intelligence, 12(7), 629–639.

Phillips, P. J., and Harlin, J. M. 1984. Spatial dependency of hydraulic geometry exponents in a subalpine stream. Journal of Hydrology, 71(3), 277-283.

Pistocchi, A., and Pennington, D. 2006. European hydraulic geometries for continental SCALE environmental modelling. Journal of Hydrology, 329(3), 553-567.

Planchon, O., and Darboux, F. 2002. A fast, simple and versatile algorithm to fill the depressions of digital elevation models. Catena, 46(2), 159-176.

Quinn, P. F. B. J., Beven, K., Chevallier, P., and Planchon, O. 1991. The prediction of hillslope flow paths for distributed hydrological modelling using digital terrain models. Hydrological processes, 5(1), 59-79.

Rennó, C. D., Nobre, A. D., Cuartas, L. A., Soares, J. V., Hodnett, M. G., Tomasella, J., and Waterloo, M. J. 2008. HAND, a new terrain descriptor using SRTM-DEM: Mapping terra-firme rainforest environments in Amazonia. Remote Sensing of Environment, 112(9), 3469-3481.

Rhodes, D. D. 1978. World-wide variations in hydraulic geometry exponents of stream channels: An analysis and some observations—Comments. Journal of Hydrology, 39(1-2), 193-197.

Richards, K. S. 1973. Hydraulic geometry and channel roughness; a non-linear system. American Journal of Science, 273(10), 877-896.

Rodda, H. J. 2005. The development and application of a flood risk model for the Czech Republic. Natural hazards, 36(1-2), 207-220.

Roering, J. J., Mackey, B. H., Marshall, J. A., Sweeney, K. E., Deligne, N. I., Booth, A. M., Handwerger A.L., and Cerovski-Darriau, C. 2013. 'You are HERE': Connecting the dots with airborne lidar for geomorphic fieldwork. Geomorphology, 200, 172-183.

Romanowicz, R., Beven, K. J., and Tawn, J. 1996. 10 Bayesian Calibration of Flood Inundation Models.

Sampson, C. C., Smith, A. M., Bates, P. D., Neal, J. C., Alfieri, L., and Freer, J. E. 2015. A high-resolution global flood hazard model. Water Resources Research, 51(9), 7358-7381.

Samuels, P. G. 1990. Cross-section location in 1-D models. 2nd International Conference on River Flood Hydraulics, Wiley, Chichester, 339-350.

Sanders, B. F. 2007. Evaluation of on-line DEMs for flood inundation modeling. Advances in Water Resources, 30(8), 1831-1843.

Sangireddy, H., Stark, C. P., Kladzyk, A., and Passalacqua, P. 2016. GeoNet: An open source software for the automatic and objective extraction of channel heads, channel network, and channel morphology from high resolution topography data. Environmental Modelling and Software, 83, 58-73.

Savage, J. T. S., Pianosi, F., Bates, P. D., Freer, J, and Wagener, T. 2016. Quantifying the importance of spatial resolution and other factors through global sensitivity analysis of a flood inundation model. Water Resources Research, 52 (11), 9146-9163.

Schumann, G. P., Di Baldassarre, G., and Bates, P. D. 2009. The utility of spaceborne radar to render flood inundation maps based on multialgorithm ensembles. IEEE Transactions on Geoscience and Remote Sensing, 47(8), 2801-2807.

Schumann, G. P., Neal, J. C., Voisin, N., Andreadis, K. M., Pappenberger, F., Phanthuwongpakdee, N., ..., and Bates, P. D. 2013. A first large-scale flood inundation forecasting model. Water Resources Research, 49(10), 6248-6257.

Schumann, G. P., Vernieuwe, H., De Baets, B., and Verhoest, N. E. C. 2014. ROC-based calibration of flood inundation models. Hydrological Processes, 28(22), 5495-5502.

Seibert, J., and McGlynn, B. L. 2007. A new triangular multiple flow direction algorithm for computing upslope areas from gridded digital elevation models. Water Resources Research, 43(4).

Sethian, J. A., 1996. A fast marching level set method for monotonically advancing fronts. Proceedings of the National Academy of Sciences 93 (4), 1591–1595.

Singh, K. P., and Broeren, S. M. 1989. Hydraulic geometry of streams and stream habitat assessment. Journal of Water Resources Planning and Management, 115(5), 583-597.

Smeeckaert, J., Mallet, C., David, N., Chehata, N., and Ferraz, A. 2013. Large-scale classification of water areas using airborne topographic lidar data. Remote sensing of environment, 138, 134-148.

Soille, P., Vogt, J., and Colombo, R. 2003. Carving and adaptive drainage enforcement of grid digital elevation models. Water Resources Research, 39(12).

Soille, P. 2004. Optimal removal of spurious pits in grid digital elevation models. Water Resources Research, 40(12).

Stephens, E. M., Bates, P. D., Freer, J. E., and Mason, D. C. 2012. The impact of uncertainty in satellite data on the assessment of flood inundation models. Journal of Hydrology, 414, 162-173.

Stephens, E., Schumann, G. P., and Bates, P. D. 2014. Problems with binary pattern measures for flood model evaluation. Hydrological Processes, 28(18), 4928-4937.

Stockdonf, H. F., Sallenger Jr, A. H., List, J. H., Holman, R. A. 2002. Estimation of shoreline position and change using airborne topographic lidar data. Journal of Coastal Research, 502-513.

Survila, K., Yıldırım, A. A., Li, T., Liu, Y. Y., Tarboton, D. G., and Wang, S. 2016, July. A Scalable High-performance Topographic Flow Direction Algorithm for Hydrological Information Analysis. XSEDE16 Conference on Diversity, Big Data, and Science at Scale, 11, ACM.

Tarboton, D. G., Bras, R. L., and Rodriguez-Iturbe, I. 1991. On the Extraction of Channel Networks from Digital Elevation Data. Hydrologic Processes, 5(1), 81-100.

Tarboton, D. G., Bras, R. L., and Rodriguez-Iturbe, I. 1992. A Physical Basis for Drainage Density. Geomorphology, 5(1/2), 59-76.

Tarboton, D. G. 1997. A new method for the determination of flow directions and upslope areas in grid digital elevation models. Water Resources Research, 33(2), 309-319.

Tarboton, D. G., and Ames, D. P. 2001. Advances in the mapping of flow networks from digital elevation data. In World water and environmental resources congress, 20-24. Am. Soc Civil Engrs USA.

Tarboton, D. G., and Baker, M. E. 2008. Towards an algebra for terrain-based flow analysis. Representing, modeling and visualizing the natural environment: innovations in GIS, 13, 167-194.

Tarboton, David G., 2016. Terrain Analysis Using Digital Elevation Models (TauDEM). Utah Water Research Laboratory. Utah State University. http://hydrology.usu.edu/taudem. accessed 9/5/2016.

Tarolli, P. 2014. High-resolution topography for understanding earth surface processes: opportunities and challenges. Geomorphology, 216, 295–312.

Tarolli, P., Dalla Fontana, G. 2009. Hillslope-to-valley transition morphology: new opportunities from high resolution dtms. Geomorphology, 113 (1), 47–56.

Tate, E. C., Maidment, D. R., Olivera, F., and Anderson, D. J. 2002. Creating a terrain model for floodplain mapping. Journal of Hydrologic Engineering, 7(2), 100-108.

Teng, J., Jakeman, A. J., Vaze, J., Croke, B. F. W., Dutta, D., and Kim, S. 2017. Flood inundation modelling: A review of methods, recent advances and uncertainty analysis, Environmental Modelling and Software, 90, 201-216.

Tesfa, T. K., Tarboton, D. G., Chandler, D. G., and McNamara, J. P. 2009. Modeling soil depth from topographic and land cover attributes. Water Resources Research, 45(10).

Tesfa, T. K., Tarboton, D. G., Watson, D. W., Schreuders, K. A., Baker, M. E., and Wallace, R. M. 2011. Extraction of hydrological proximity measures from DEMs using parallel processing. Environmental Modelling and Software, 26(12), 1696-1709.

Tinkler, K. J., and Pengelly, J. W. 1995. Great Lakes response to catastrophic inflows from Lake Agassiz: some simulations of a hydraulic geometry for chained lake systems. Journal of Paleolimnology, 13(3), 251-266.

Toscano, G. J., Gopalam, U., Devarajan, V. 2013. A novel method for automation of 3D hydro break line generation from LiDAR data using MATLAB. ISPRS-International Archives of the Photogrammetry, Remote Sensing and Spatial Information Sciences 1(2), 99-104.

Toscano, G., Gopalam, U., Devarajan, V. 2014. Auto Hydro Break Line Generation Using LiDAR Elevation and Intensity Data. ASPRS Conference, Louisville, Kentucky.

Toscano, G. J. 2015. A LiDAR-based auto hydro breakline generation algorithm for standing water bodies (Doctoral dissertation, The University of Texas at Arlington).

Trigg, M. A., Bates, P. D., Wilson, M. D., Schumann, G. P., and Baugh, C. 2012. Floodplain channel morphology and networks of the middle Amazon River. Water Resources Research, 48(10).

Ullrich, A., and Pfennigbauer, M. 2016. Linear LIDAR versus Geiger-mode LIDAR: impact on data properties and data quality. In SPIE Defense+Security 983204-983204. International Society for Optics and Photonics.

Viger, R. J., Rea, A., Simley, J. D., and Hanson, K. M. 2016. NHDPlusHR: A National Geospatial Framework for Surface-Water Information. Journal of the American Water Resources Association (JAWRA), 52(4), 901-905.

Vigil, M., Shunk, K., and McArthur, K. 2016, One Creek, Two Floods: A Comparison of the Storms and Response, TFMA 2016 Spring Conference, Houston, Texas, available online at <https://c.ymcdn.com/sites/www.tfma.org/resource/resmgr/SpringConference2016Presentations/Wed_5_One_Creek_Two_Floods.pdf>

Wallis, C., Wallace, R., Tarboton, D. G., Watson, D. W., Schreuders, K. A. T., and Tesfa, T. K. 2009. Hydrologic terrain processing using parallel computing. In 18th World IMACS Congress and MODSIM09 International Congress on Modelling and Simulation, Modelling and Simulation Society of Australia and New Zealand and International Association for Mathematics and Computers in Simulation, 2540-2545.

Wallis, C., Watson, D., Tarboton, D., and Wallace, R. 2009. Parallel flow-direction and contributing area calculation for hydrology analysis in digital elevation models. Power, 11(8), 7.

Wang, S. 2010. A CyberGIS framework for the synthesis of cyberinfrastructure, GIS, and spatial analysis. Annals of the Association of American Geographers, 100(3), 535-557.

Werner, M. G. F. 2001. Impact of grid size in GIS based flood extent mapping using a 1D flow model. Physics and Chemistry of the Earth, Part B: Hydrology, Oceans and Atmosphere, 26(7), 517-522.

Wide, S. M., and Smith, J. D. 1996. A reach-averaged model of diurnal discharge wave propagation down the Colorado River through the Grand Canyon. Water Resources Research, 32(5), 1375-1386.

Wing, O. E., Bates, P. D., Sampson, C. C., Smith, A. M., Johnson, K. A., and Erickson, T. A. 2017. Validation of a 30 m resolution flood hazard model of the conterminous United States. Water Resources Research, 53(9), 7968-7986.

Wohl, E., Kuzma, J. N., and Brown, N. E. 2004. Reach-scale channel geometry of a mountain river. Earth Surface Processes and Landforms, 29(8), 969-981.

Woodruff, J. D., Irish, J. L., and Camargo, S. J. 2013. Coastal flooding by tropical cyclones and sea-level rise. Nature, 504(7478), 44-52.

Worstell, B. B., Poppenga, S., Evans, G. A., and Prince, S. 2014. Lidar point density analysis: implications for identifying water bodies. US Geological Survey (No. 2014-5191).

Wu, H., Adler, R. F., Tian, Y., Huffman, G. J., Li, H., and Wang, J. 2014. Real-time global flood estimation using satellite ‐ based precipitation and a coupled land surface and routing model. Water Resources Research, 50(3), 2693-2717.

Yamazaki, D., O'Loughlin, F., Trigg, M. A., Miller, Z. F., Pavelsky, T. M., and Bates, P. D. 2014. Development of the global width database for large rivers. Water Resources Research, 50(4), 3467-3480.

Yıldırım, A. A., Watson, D., Tarboton, D., and Wallace, R. M. 2015. A virtual tile approach to raster-based calculations of large digital elevation models in a shared-memory system. Computers & Geosciences, 82, 78-88.

Zhang, J., Huang, Y. F., Munasinghe, D., Fang, Z., Tsang, Y. P., and Cohen, S. 2018. Comparative Analysis of Inundation Mapping Approaches for the 2016 Flood in the Brazos River, Texas. Journal of the American Water Resources Association (JAWRA), 1–14.

Zheng, X. 2015. Hydraulic fabric: an information framework for river channel cross section data (Master dissertation, The University of Texas at Austin).

Zheng, X., Tarboton, D., Maidment, D. R., Liu, Y. Y., and Passalacqua, P. 2018. River Channel Geometry and Rating Curve Estimation Using Height Above the Nearest Drainage. Journal of the American Water Resources Association (JAWRA), under review.

Maidment, D. R., Brookshire, D., Brown, J. W., Dorman, J., Galloway, G., Imam, B., and Lathrop, W. 2009. Mapping the Zone: Improving Flood Map Accuracy.

Vita

Xing Zheng was born in Shangcheng, Henan, China, the son of Feng Zheng and Changqun Xia. He attended primary school in Shangcheng, and then attended Xinyang High School until graduation in 2009. After graduation, he entered Wuhan University where he received a Bachelor of Science in Hydrology and Water Resources Engineering in June, 2013. In August, 2013, Xing entered the Graduate School at the University of Texas at Austin. At UT Austin, he received the degree of Master of Science in Engineering from the Environmental and Water Resource Engineering program in May, 2015.

Permanent email: zhengxing@utexas.edu

This dissertation was typed by Xing Zheng.